Spring 1-1-2013

A Model for the Rapid Evaluation of Active Magnetic Shielding Designs

Scott Allen Washburn
University of Colorado at Boulder, scott.a.washburn@colorado.edu

A MODEL FOR THE RAPID EVALUATION OF ACTIVE MAGNETIC SHIELDING DESIGNS

by

SCOTT ALLEN WASHBURN

B.S., Mechanical Engineering, University of Colorado, Boulder, 2001

M.S., Aerospace Engineering Sciences, University of Colorado, Boulder, 2011

A thesis submitted to the

Faculty of the Graduate School of the

University of Colorado in partial fulfillment

of the requirement for the degree of

Doctor of Philosophy

Department of Aerospace Engineering Sciences

2013

This thesis entitled:
A Model for the Rapid Evaluation of Active Magnetic Shielding Designs
written by Scott Allen Washburn
has been approved for the Department of Aerospace Engineering Sciences

_____
Professor George H. Born

_____
Professor David M. Klaus

Date_____

The final copy of this thesis has been examined by the signatories, and we find that both the content and the form meet acceptable presentation standards of scholarly work in the above mentioned discipline.

Washburn, Scott Allen (Ph.D., Aerospace Engineering Sciences)

A Model for the Rapid Evaluation of Active Magnetic Shielding Designs

Thesis directed by Professor George H. Born

The use of active magnetic radiation shielding designs has the potential to reduce the radiation exposure received by astronauts on deep-space missions at a significantly lower mass penalty than designs that utilize only passive shielding. One of the common techniques for assessing the effectiveness of active or passive shielding designs is the use of Monte Carlo analysis to determine crew radiation exposure. Unfortunately, Monte Carlo analysis is a lengthy and computationally intensive process, and the associated time requirements to generate results make a broad analysis of the active magnetic shield design trade space impractical using this method. The ability to conduct a broad analysis of system design variables would allow the selection of configurations suited to specific mission goals, including mission radiation exposure limits, duration, and destination. Therefore, a rapid analysis method is required in order to effectively assess active shielding design parameters, and this body of work was developed in order to address this need.

Any shielding analysis should also use complete representations of the radiation environment and detailed transport analyses to account for secondary particle production mechanisms. This body of work addresses both of these issues by utilizing the full Galactic Cosmic Radiation GCR flux spectrum and a detailed transport analysis to account for secondary particle effects due to mass interactions. Additionally, there is a complex relationship between the size and strength of an active shielding design and the amount and type of mass required to create it. This mass can significantly impact the resulting flux and radiation exposures inside the active shield, and any shielding analysis should not only include passive mass, but should attempt to provide a reasonable estimate of the actual mass associated with a given design. Therefore, a survey of active shielding systems is presented so that reasonable mass quantity and composition estimates can be utilized. This survey also allows the identification of several key

technologies for the development of an active magnetic shield design. The resulting rapid analysis model allows a large range of magnetic field strengths and thicknesses to be analyzed, allowing the determination of design requirements in order to address the needs of different missions.

Acknowledgements

I would like to thank the members of my dissertation committee for providing guidance and direction throughout this research. First, I thank my advisor, Dr. George Born, for his support and advice. I would also like to thank Dr. David Klaus, not only for his time and effort, but for providing the spark that got me interested in this subject. I am deeply indebted to Dr. Steve Blattnig and Dr. Robert Singleterry for their tremendous amount of time, guidance, and patience. Finally, I thank the other members of my committee: Dr. Jeff Parker and Dr. Webster Cash.

I would also like to offer my thanks to Shayne Westover at the Johnson Space Center for his generous time and support and also for allowing me to participate in his NIAC study which was infinitely helpful in this research.

This work has been performed through generous support by a National Defense Science and Engineering Graduate (NDSEG) Fellowship, sponsored by the Army Research Office.

Table of Contents

List of Figures

List of Tables

Chapter 1

Introduction

Providing adequate radiation protection is one of the most significant problems facing long duration, deep space, human exploration missions. Chronic radiation exposure from Galactic Cosmic Radiation (GCR) and acute exposure from Solar Particle Events (SPEs) pose serious health threats to astronauts as they venture away from the protection of the near-Earth environment (Durante and Cucinotta, 2011; Townsend, 2005a). The radiation exposure levels in deep space are of such concern that radiation mitigation for human spaceflight was identified by the National Research Council (NRC) as the number one technological priority for extending and sustaining human activities beyond low Earth orbit (NRC, 2012). Additionally, NASA has identified radiation mitigation as one of the crucial items in their technology roadmap, "necessary to achieve national and agency goals in human space exploration over the next few decades" (NASA, 2012).

Current exploration goals seek to enable mission durations of a year or more in order to reach high interest destinations, and adequate radiation protection must be provided to ensure the safety of the crew. Without appropriate shielding, astronauts on a deep space mission can easily accumulate 1 to 2 mSv per day in interplanetary space (Cucinotta and Durante, 2006). These exposure rates stand in stark contrast to the average effective dose of 80 mSv for 6-month ISS missions (Cucinotta et al., 2008) or the 1 to 2 mSv per year for the average human on earth

(Buckley, 2006). Exposure rates of this magnitude could severely limit mission capabilities and pose serious health concerns for the crew.

Unfortunately, because of the nature of the space radiation environment, large amounts of passive shielding are required in order to meet current permissible exposure limits (Singleterry, 2013). In order to lower the radiation exposure received, at a reduced mass penalty, several types of "active" radiation shielding designs have been proposed. Since radiation in space consists primarily of charged particles, these active designs use electromagnetic forces to divert harmful radiation away from the crew. One of the most promising categories of these active designs utilizes confined magnetic fields (Spillantini, 2011; Westover et al. 2012). This type of design takes advantage of the Lorentz force, created by a charged particle moving through the magnetic field, which is used to divert the radiation.

1.1 Rationale and Motivation for the Research

One of the techniques for assessing the effectiveness of active or passive shielding designs is the use of Monte Carlo analysis to determine crew radiation exposure. Unfortunately, Monte Carlo analysis is a lengthy and computationally intensive process, and the associated time requirements to generate results make a broad analysis of the active shield design trade space impractical using this method. The ability to conduct a broad analysis of system design variables would allow the selection of configurations suited to specific mission goals, including mission radiation exposure limits, duration, and destination. Therefore, a rapid analysis method is required in order to effectively assess active shielding design parameters, and this research was implemented in order to address this need.

The active shielding design trade space generally includes three primary variables: magnetic field strength, magnetic field thickness, and passive/structural shielding mass. There is a complex relationship between the size and strength of the magnetic field and the amount and type of mass required to create it, and this mass can significantly impact the resulting flux and radiation exposures inside the active shield. Therefore, any such analysis should not only include passive mass, but it should attempt to provide a reasonable estimate of the actual mass associated with a given design. Additionally, the 2008 National Research Council study, *Managing Space Radiation Risk in the New Era of Space Exploration*, explicitly calls out for the following to be provided when evaluating active shielding designs: "complete and realistic representations of radiation environments expected in deep space", and "detailed transport analyses that consider all relevant secondary particle production mechanisms" (NRC, 2008).

This body of work seeks to address each of these issues by utilizing the full GCR flux spectrum as well as detailed transport analysis to account for secondary particle effects due to mass interactions. The selected deterministic transport code used in this body of work allows for the rapid analysis desired; however, this does come with some loss of fidelity in the associated physics and engineering modeling over the Monte Carlo method. Secondary particle effects, accounted for by utilizing this transport code, depend not only on the quantity of mass encountered, but the material composition as well. Therefore, a survey of active shielding systems is conducted so that reasonable mass quantity and composition estimates can be utilized. This survey also allows the identification of several key technologies for the development of an active shield design. The resulting rapid analysis model allows a large range of magnetic field strengths and thicknesses to be analyzed, allowing the determination of design requirements in order address the needs of different missions.

1.2 Dissertation Overview

This dissertation begins with a discussion of the radiation exposure problem in Chapter 2. Different mitigation strategies are discussed and a review of the history of active shielding is presented. Because the analysis of radiation exposure in the space environment is a complex and interdisciplinary problem, the required analysis fundamentals are presented in Chapter 3. This describes the major components and building blocks of this body of work and identifies where and how these are utilized. This chapter covers the space radiation environment, radiation protection quantities and units, biological damage, exposure limits, and radiation transport analysis.

Chapter 4 introduces the new modeling method that has been developed in order to provide rapid active shielding analysis for a solenoid design. Results are presented for a basic case where the mass properties are represented by a uniform quantity of aluminum, which does not vary over the trade space analyzed. This basic model is improved by conducting a system survey of active shielding designs, presented in Chapter 5; providing the basis for mass and material estimates of an active shielding design over the entire design trade space. Several key technologies for the development of an active shield, identified during this process, are also presented. In Chapter 6, the mass and material estimates from Chapter 5 are incorporated into the rapid analysis model and trade space results are presented. Additionally, Chapter 6 provides a comparison of the new modeling results to Monte Carlo results from a recent NIAC study of a similar solenoid design. A summary of the major conclusions of this work, as well as recommendations for future work, is provided in Chapter 7.

Chapter 2

Radiation Mitigation Strategies

Since the dawn of the space age and the discovery of the Van Allen radiation belts, by the Explorer 1 satellite in 1958, the space radiation environment has been recognized as a potential threat and numerous ideas have been proposed to shield from its harmful effects. The traditional engineering strategy for reducing radiation exposure is, "Time, Distance, and Shielding." Reducing time spent near a source, increasing distance to a source, or increasing the amount of shielding present will all decrease radiation exposure. Unfortunately, some of these terrestrial mitigation strategies do not necessarily apply to the space environment.

Since the goal of human space exploration is to expand human presence in space, this will inevitably entail longer duration missions and more time spent in the space radiation environment rather than less. Additionally, the space radiation environment is unique in that the environment impinging on the surface of a vehicle is isotropic, eliminating distance as a variable in reducing exposure. This leaves shielding as the remaining factor for reducing radiation exposure. It was recognized early on that effective shielding using only passive methods would require significant amounts of mass. Thus, taking advantage of the ionized nature of the space radiation environment, numerous active shielding techniques have been proposed over the years. Aside from these traditional mitigation strategies, there is also the option of using biological countermeasures, which will likely be a part of any comprehensive radiation mitigation strategy.

The goal of such countermeasures is not to minimize exposure, but rather reduce the undesirable biological effects of the exposure.

2.1 Biological Countermeasures

Biological countermeasures is a generic term that refers to a variety of proposed techniques for mitigating the harmful biological effects of radiation, rather than the exposure level itself. These countermeasures, also known as radioprotectants, can range from dietary measures to pharmaceuticals. Regardless of the method, the techniques currently being developed all seek to reduce the damage caused by radiation induced ionization through inhibiting the effects of the resulting free radicals in the body or enhancing the body's own inherent mechanisms for damage repair.

Dietary measures can include techniques such as eating anti-oxidant rich foods (Weiss and Landauer, 2000) or ingesting water that has been enhanced with therapeutic gasses, such as hydrogen, to scavenge free radicals (Schoenfeld et al., 2012). There are also a variety of different pharmaceuticals under development (Patel et al., 2011) such as the drug amifostine (ethyol or WR2721), which was originally developed to reduce the side effects of radiation treatment and chemotherapy. While countermeasures will likely be a necessary part of any comprehensive radiation mitigation strategy for a long-term mission, they will not be discussed in further detail here.

2.2 Passive Shielding

Passive shielding is the method of utilizing mass to create a protective barrier around the astronauts. This includes not only shielding placed specifically for radiation protection, but also

any surrounding structural materials. The effects of this passive mass can be significant, as this mass can attenuate some of the incident flux. However, the high energy component of GCR flux is extremely penetrating and can result in secondary particle effects that arise from the attenuation of the radiation as it passes through matter (Trovati et al. 2006). Figure 2.1 shows the dose equivalent vs. depth relationship for various shielding and structural materials.

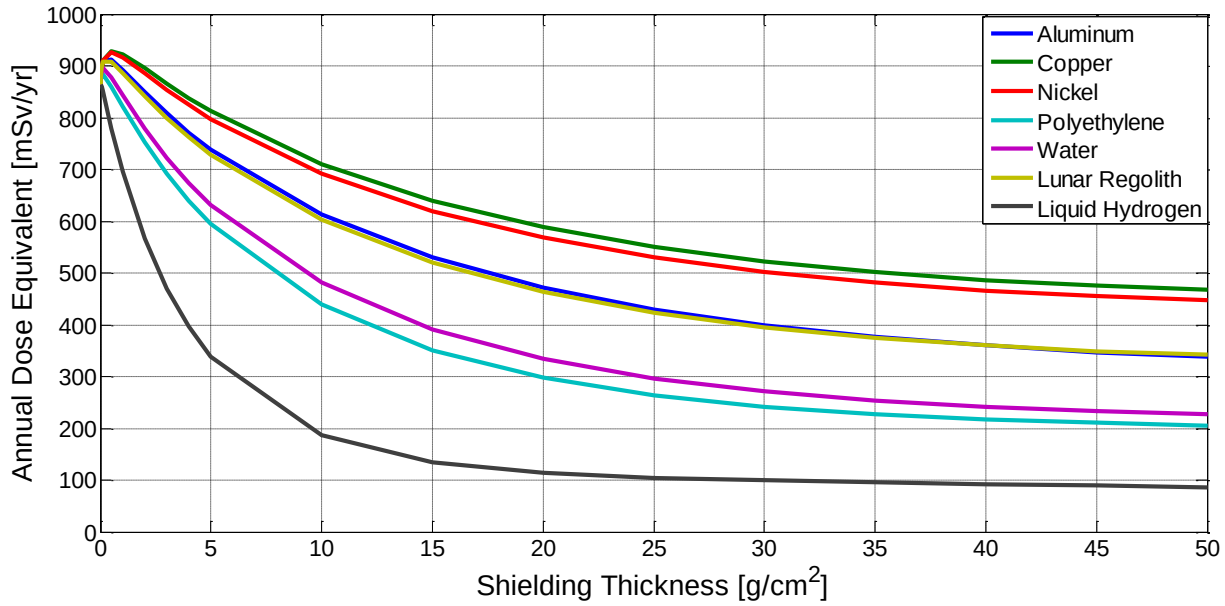

Figure 2.1 Point Dose Equivalent vs. Depth for Various Shielding Materials for 1977 Solar Minimum GCR Flux (BO'10 GCR model transported using HZETRN2010)

These dose equivalent vs. depth curves demonstrate that shielding effectiveness is reduced as the shielding thickness increases for GCR flux. This is the result of secondary radiation and particle production due to the GCR interaction with the shielding material. These secondary sources of radiation may have lower energy; however, they can also transmit more energy to surrounding material than their parent particles and cause greater biological damage. This will be discussed in greater detail in Chapter 3.

Significant quantities of passive shielding may be required to achieve low exposure levels (Singleterry, 2013), as demonstrated in Figure 2.2. The reduction in shielding efficacy, as

shielding thickness increases, indicates that increasing quantities of passive shielding beyond a certain point may not be worth the increased system mass. Certain exposure threshold may not even be achievable with passive shielding alone. The effects of secondary radiation can also be seen in the initial increase in dose equivalent values for heavier shielding materials such as aluminum.

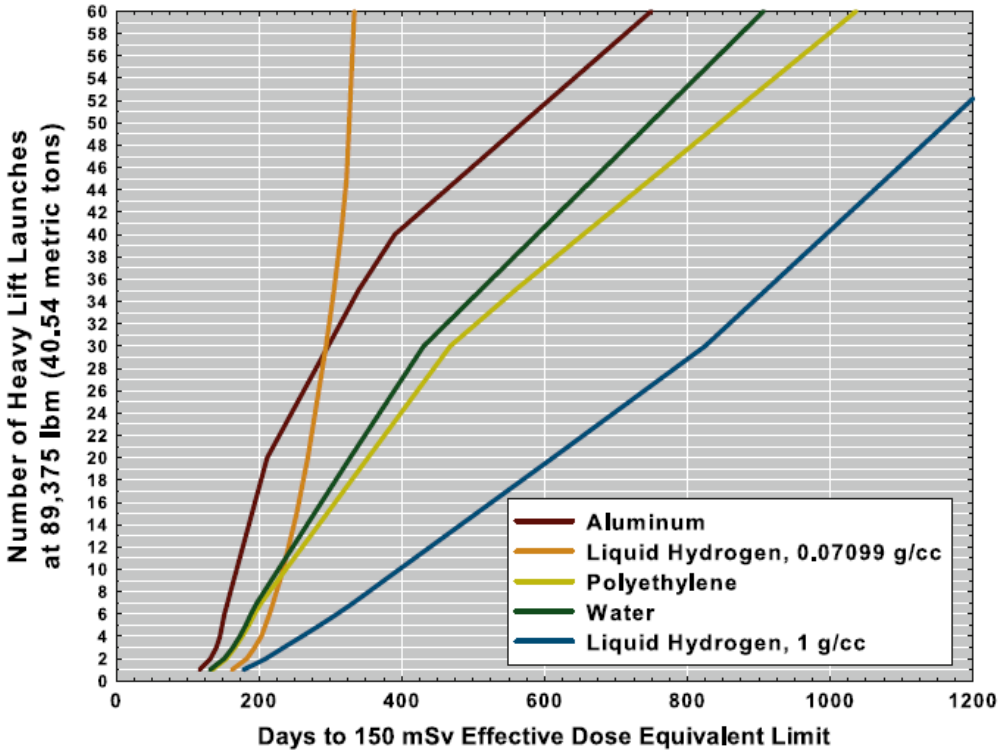

Figure 2.2 Shielding Mass Required to Enable Mission Durations for Various Materials (Singleterry, 2013, reprinted with permission from Elsevier)

Figures 2.1 and 2.2 also shows that, in addition to the quantity of passive shielding, quality is also important. Different materials have different shielding properties and can produce different secondary particle effects. The shielding effectiveness per unit mass decreases with increasing atomic number and is highest for hydrogen (Wilson et al. 1995). Thus, high hydrogen content materials, such as polyethylene, are more desirable for passive shielding. Secondary production increases with the mass number of the shielding material, making materials such as

lead, which are traditionally desirable for terrestrial applications, less effective when subjected to GCR flux. Because of the complex interaction of radiation with mass, any analysis of shielding methods, including active shielding, must necessarily include the effects of passive and structural mass. This includes not only the quantity of the shielding mass, but the composition as well.

2.3 Active Shielding

The space radiation environment is composed primarily of charged particles. This enables the possibility of deflecting these particles using "active" shielding designs in order to reduce the radiation exposure possibly using less mass than would be required by passive shielding for an equivalent amount of protection. Over the last several decades, many shielding designs that actively deflect the incoming charged particle radiation have been proposed (Sussingham and Cocks, 1999; Spillantini, 2010). There are several general classes of active shielding which take advantage of electromagnetic forces that can be used to divert harmful radiation away from the crew.

Active shielding concepts fall into four basic categories: (1) electrostatic fields, (2) plasma shields, (3) confined magnetic fields, and (4) unconfined magnetic fields. A thorough review of active shielding designs is presented in *Forty Years of Development of Active Systems for Radiation Protection of Spacecraft* by Sussingham et al. (1999). Additionally, excellent summaries of passive and active shielding methods can be found in the NASA publications *Shielding Strategies for Human Space Exploration* (Wilson et al., 1997) and *Revolutionary Concepts of Radiation Shielding for Human Exploration of Space* (Adams et al., 2005), as well as a *Critical Analysis of Active Shielding Methods for Space Radiation Protection* (Townsend,

2005b). The following sections discuss the four main active shielding categories and provide a brief history of each.

2.3.1 Electrostatic Fields

Some of the first active shielding ideas proposed were the use of electrostatic fields (Vogler, 1964). These designs create an electric field around the spacecraft by either charging the spacecraft itself or creating charged points around it. The merits of such an electrostatic design have been presented and discussed numerous times over the years (Sussingham et al., 1999; Townsend, 2005b; Tripathi et al., 2006; and Tripathi et al., 2011). While some studies have made favorable assessments of this shielding method, most have concluded that these designs are not feasible. This is generally attributed to the high voltages required to deflect incoming GCR radiation, on the order of 10^{10} volts according to Adams et al. (2005). These high voltages were far beyond the technological capacity during the 1960s, when they were originally suggested, and still remain well above the capabilities of current technology. Additionally, the vacuum and insulation breakdown characteristics of the space environment would require extremely large structures in order to make these designs feasible. The interplanetary space environment itself contains about 10 particles per cubic centimeter, which is sufficient to serve as a conductor at high voltages, and this makes maintaining the required voltage potentials extremely difficult.

2.3.2 Plasma Shielding

Another approach suggested early on was the use of plasma shielding (Levy and Janes 1964). In this design, a large free electron plasma was proposed to mitigate incoming protons, and this plasma would be bound through the use of a magnetic field to maintain the electron

cloud at a confined distance from the spacecraft. Such designs were originally proposed to shield from SPE protons, and subsequent analysis has found these designs to be insufficient for shielding against the more energetic GCR spectrum (Adams et al., 2005; Townsend, 2005b). Therefore these designs have generally not been recommended for further pursuit.

2.3.3 Confined and Unconfined Magnetic Fields

The concept of shielding utilizing magnetic fields can be broken into two categories: confined and unconfined. These designs take advantage of the Lorentz force, created by a charged particle moving through the magnetic field, which can be used to divert harmful radiation away from the crew. In general, unconfined magnetic fields use low strength fields that are significantly larger in size than the habitat they are providing protection for. Although the strength of these fields may be low, the large size of the field allows particles to be diverted. In fact, these designs are similar in concept to the protection provided by the earth's magnetic field. Confined magnetic fields rely on higher strength magnetic fields that are confined within structures placed immediately surrounding the habitat.

Because of the large scale of these magnetic fields, practical implementation of these concepts relies on superconductor technology, similar to large scale terrestrial magnets such as those used in MRI machines. The first suggestion of utilizing superconducting coils for this purpose can be traced back to S.F. Singer (Sussingham et al., 1999), prior to the beginning of the manned space program. This concept was actively pursued by both the US and Soviet space programs all the way through the Apollo era. As superconductor technology progressed, even Werner von Braun began promoting these designs for protecting astronauts during interplanetary travel (von Braun, 1969).

Superconductors themselves were originally discovered in 1911 by the Dutch physicist Heike Kamerlingh Onnes (Cyrot and Pavuna, 1992). This original class of superconductors is now known as low temperature superconductors, with transition temperatures, $T_{C,}$ below 20 K. Since high temperature superconductors were unknown at the time, early magnetic shielding designs were centered on these low T_C technologies, usually NbTi or Nb_3Sn, which required liquid He for cooling. Initial active shielding studies concluded that the required cooling system mass to operate these designs provided questionable savings over passive only designs. In 1986, researchers at IBM Laboratories discovered the first high temperature superconductor, LaBaCuO ceramics, with a T_C of 38 K. A flood of new research soon discovered superconductors with even higher transitions temperatures. With the prospect of significantly reducing the cooling requirements for a superconducting coil, research into this area for space applications was once again proposed (Cocks, 1991).

Recently, the development of the Alpha Magnetic Spectrometer (AMS; Chung et al., 2005), which uses similar technology principles for the employment of a high strength magnetic field in space, has furthered interest in these designs. The success of the AMS experiment can be credited with spawning studies by Hoffman et al. (2005), Figure 2.3, and Westover et al. (2012), Figure 2.4, through NASA's Advanced and Innovative Concepts (NIAC) grants, as well as an ESA study by Battiston et al. (2011). Although many technical advances need to be made in order to make these shields a reality (Townsend, 2005b; Spillantini, 2010) they do hold the promise of being able to reduce the radiation dose received by astronauts on such missions to acceptable levels at a significantly lower mass penalty than passive only designs.

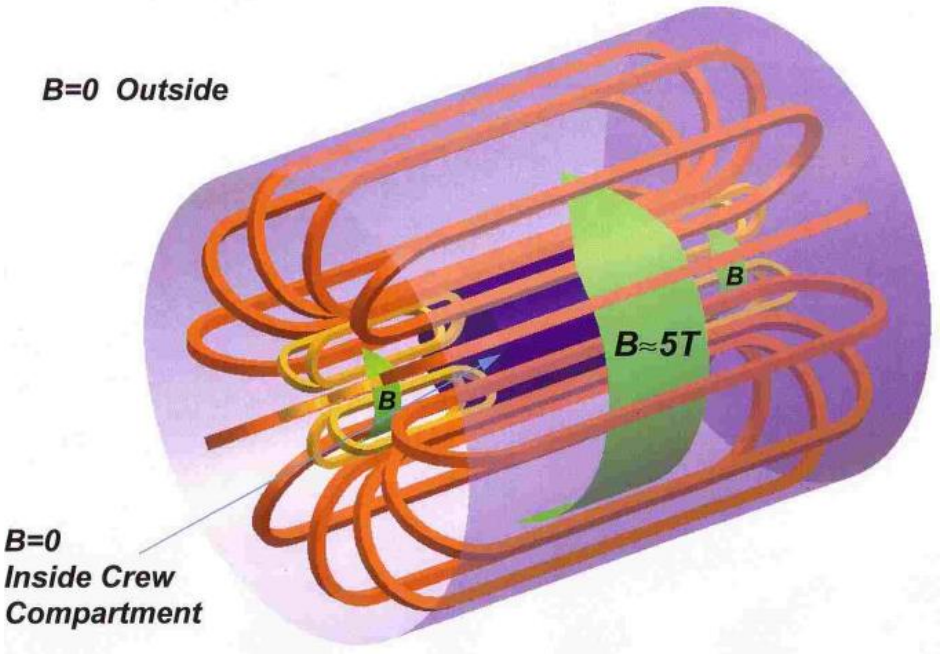

Figure 2.3 Hoffman et al. Active Shielding Design (Hoffman et al., 2005)

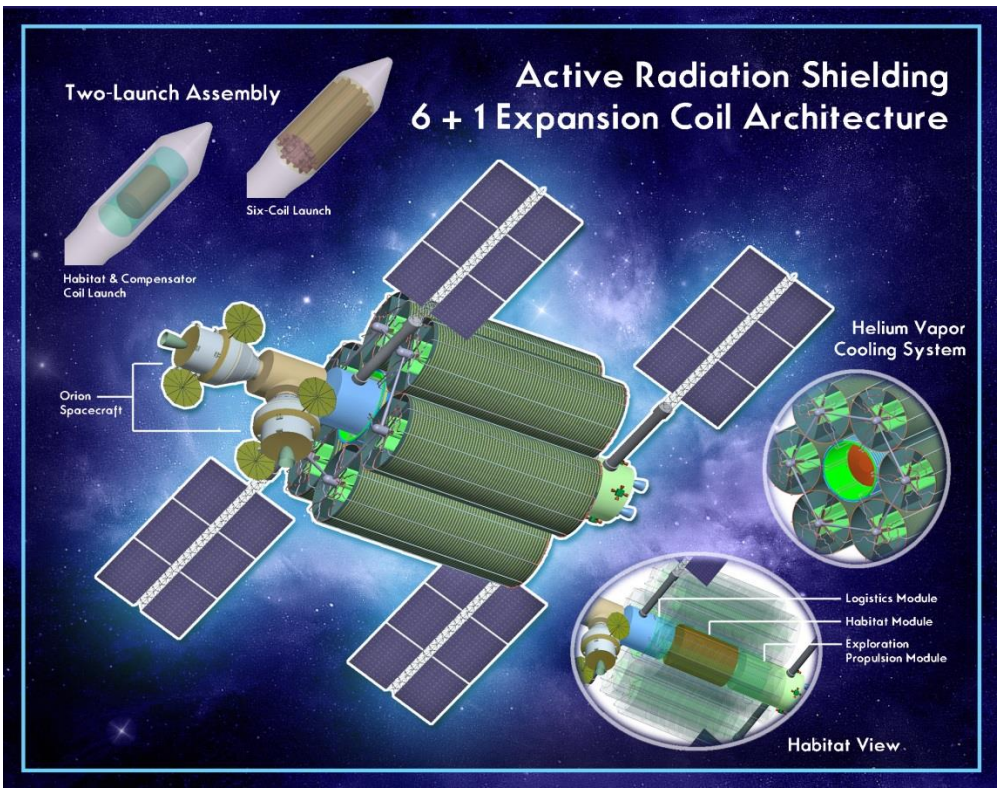

Figure 2.4 Westover et al. Active Shielding Design (NASA, NIAC website)

This body of work will focus specifically on confined magnetic fields. These confined fields generally fall into two design categories: toroidal, with the magnetic field lines curling around the habitat structure, and solenoidal, with the magnetic field lines running parallel to the central axis of the habitat. The rapid evaluation method presented here focuses specifically on the solenoid design case; however, the principles developed here can be modified and applied to the toroidal case as well.

Chapter 3

Space Radiation Analysis Fundamentals

The analysis of radiation exposure in the space environment is a complex and interdisciplinary problem. This chapter introduces the fundamental topics upon which the subsequent work is based, including the space radiation environment, radiation protection quantities and units, biological damage, radiation exposure limits, and radiation transport analysis. Each subject is reviewed and its application to the current body of work is presented. Discussion of the space radiation environment and radiation transport methods each tie into the implementation of the modeling work presented, while topics on radiation protection quantities and units, biological damage, and radiation exposure limits provide context for the results. Research is still ongoing in many of these areas, particularly in radiation protection quantities and exposure limits where there are high levels of uncertainty, and these topics will continue to evolve as understanding of these subjects improves.

3.1 Space Radiation Environment

The space radiation environment is fundamentally different from that experienced on earth. Even in terrestrial "high radiation" environments, such as nuclear power plants, the radiation exposure risks are due primarily to alpha particles, beta particles, neutrons, and gamma rays, which are all relatively low energy when compared to deep space radiation. The Earth, including its atmosphere and magnetosphere, provides a natural protection that shields humans

from the high radiation levels in space. Even in low earth orbit (LEO) much of this protection is still provided to astronauts who, while still at a higher risk of radiation exposure, are relatively protected.

The radiation environment beyond the earth's protection is composed of three primary sources: the Van Allen radiation belts (and other trapped belts around other planets), Solar Particle Events (SPEs), and Galactic Cosmic Radiation (GCR). Unlike terrestrial radiation sources, these forms of radiation consist of high energy, charged particles. Manned missions which seek to extend beyond LEO will need to sufficiently protect against these radiation sources.

3.1.1 Van Allen Belts

The Van Allen radiation belts consist primarily of protons and electrons which are trapped in the earth's magnetic field. While these belts present a significant source of radiation exposure in LEO (NRC, 2010), the flux levels in these belts drop rapidly after several earth radii (Olsen, 2005). Therefore, most human exploration missions beyond LEO will pass through this zone quickly, and any contribution from this radiation source is assumed to be negligible (Townsend, 2005b).

3.1.2 Solar Particle Events

Solar Particle Events (SPEs) are the result of powerful solar storms which occur periodically on the surface of the sun. The radiation released from these SPEs is composed of relatively high energy, low mass particles. These consist primarily of protons and helium ions, but also contain some higher atomic number particles (Buckley, 2006). SPEs are directional in

nature and only pose a risk to astronauts if they happen to lie along the trajectory of the SPE path. However, the directionality of SPEs occurs primarily at a large scale, and the radiation exposure of a spacecraft within a SPE environment is approximately isotropic. Therefore, SPEs cannot be directionally shielded, and are usually treated as an isotropic source. Additionally, SPEs are highly sporadic and tend to fluctuate in frequency corresponding to the 11 year solar cycle, with a greater number of events occurring near the solar cycle peak. This 11 year solar cycle is often described by the solar modulation parameter, with larger values corresponding to periods of greater solar activity (the solar modulation parameter is directly associated with solar activity, although it is often associated with GCR because it is a primary variable used in some GCR flux models). Figure 3.1 shows the history of large SPEs relative to solar activity, as described by the solar modulation parameter.

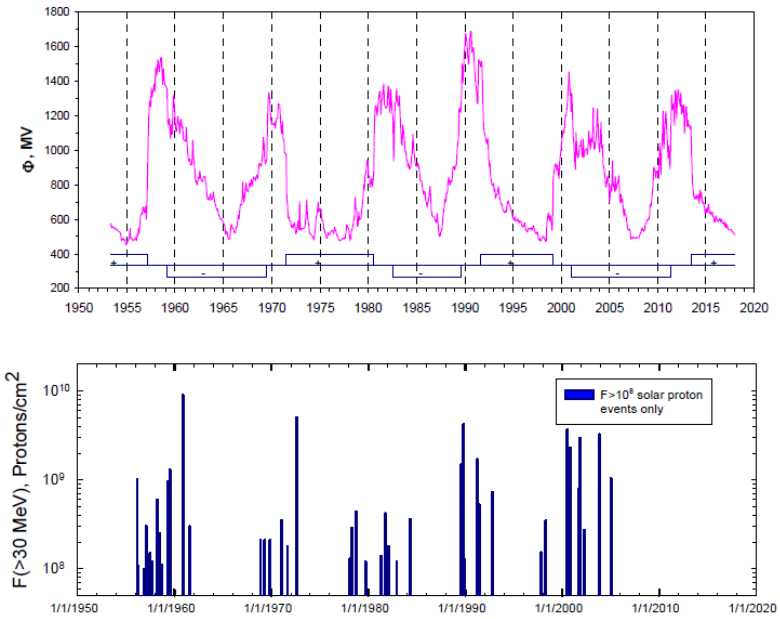

Figure 3.1 Historical data on fluence of protons above 30 MeV per cm^2 F(>30 MeV) from large SPEs relative to solar modulation parameter (Φ). Only events with $\Phi_{>30\ MeV} > 10^8$ particles per cm^2 are shown in the lower graph (Cucinotta et al., 2013)

Small SPEs, which are composed of fewer high energy particles, are generally not of concern as they can be effectively shielded by existing structures (Wilson et al., 1997). However, large SPEs can pose a significant health hazard to humans if not effectively shielded (Parsons and Townsend, 2000; Townsend, 2005a). Additionally, the radiation received from such exposures would also contribute to long-term deterministic and stochastic effects, described in Section 3.4.

Studies have shown that active shielding which is sufficient to reduce GCR dose will also effectively reduce SPE exposures (Wilson et al., 1997). Although SPEs are characterized by high flux bursts of particles, the energies are much lower than those comprising the GCR spectrum, as shown in Figure 3.2. Active shielding which is sufficient to deflect even the lower end of the GCR spectrum will also effectively deflect most of the SPE spectrum. Therefore, if there is an effective active shield SPE exposure only becomes a serious problem for activities outside the shielding structure, such as while conducting an EVA, and can be ignored for active shielding analysis.

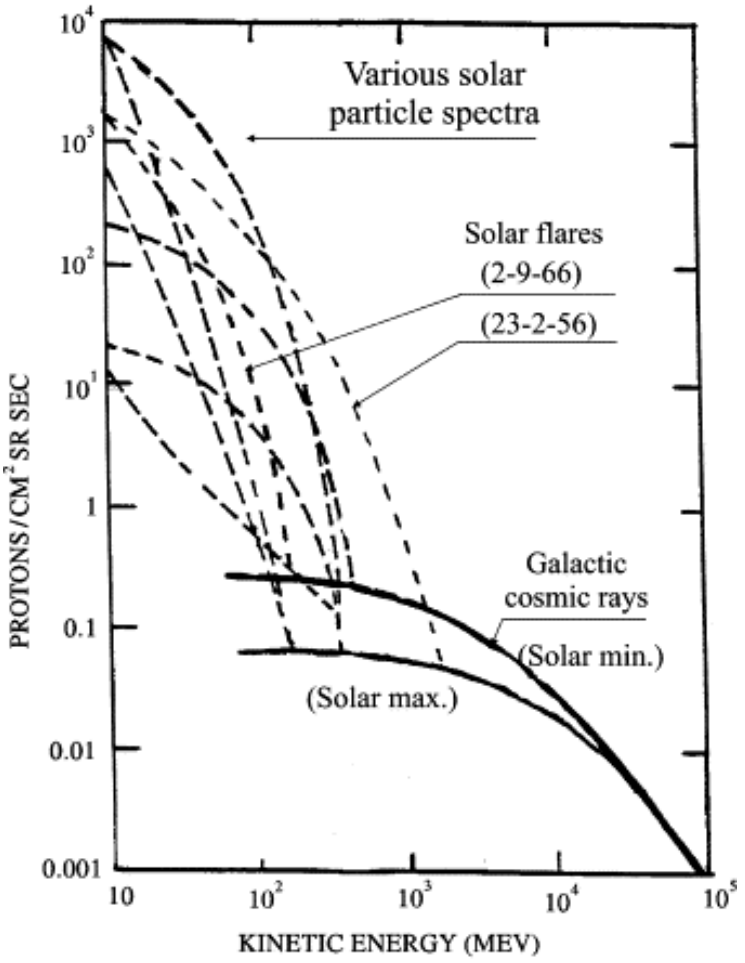

Figure 3.2 SPE and GCR Fluence and Energy
(Spillantini et al., 2000, reprinted with permission from Elsevier)

3.1.3 Galactic Cosmic Radiation

Galactic Cosmic Radiation (GCR) is the ambient background radiation in space, produced by distant exploding supernovae which send vast numbers of ions into the galaxy. This radiation consists of an isotropic, continuous flux of very high energy radiation composed of High charge (Z) and Energy (HZE) particles. The intensity of the GCR spectrum in the inner solar system also varies with the 11 year solar cycle, shown in Figure 3.1, due to the solar wind and interplanetary magnetic field. During periods of increased solar activity, the increased

outward flow of solar particles (solar wind) and greater interplanetary magnetic field remove some of the lower energy GCR spectrum and may reduce the energy of the remaining GCR spectrum. "The result is that, at times of solar maximum, the GCR energy distribution in the inner solar system has a lower energy fluence than at times of solar minimum. The consequence is that, at solar minimum, doses can be on average two to three times higher than at solar maximum" (NASA, 2010).

This flux is comprised of approximately 88% protons, 10% alpha particles, and 2% heavier ions (Z >2). Although these heavy ions comprise only a small percentage of the overall GCR flux, their relative mass, charge, and energy possess a significant biological threat. Electrons and positrons also comprise a small portion of the overall GCR flux, but are generally ignored since they are a minor biological hazard compared to the remainder of the GCR flux and are easily shielded (NASA, 2010). This continuous high energy, low flux radiation source presents a significant long term health hazard in the form of stochastic effects such as cancer, as described in Section 3.4. For example, in the presence of this high energy flux, on a mission to Mars, "every cell nucleus within an astronaut would be traversed by a proton or secondary electron every few days, and by an HZE ion every few months" (Cucinotta et al., 1998). While the potential consequences of being subjected to radiation from a SPE are severe, it is this continuous presence of the background GCR which is of primary concern in enabling long duration human exploration beyond LEO.

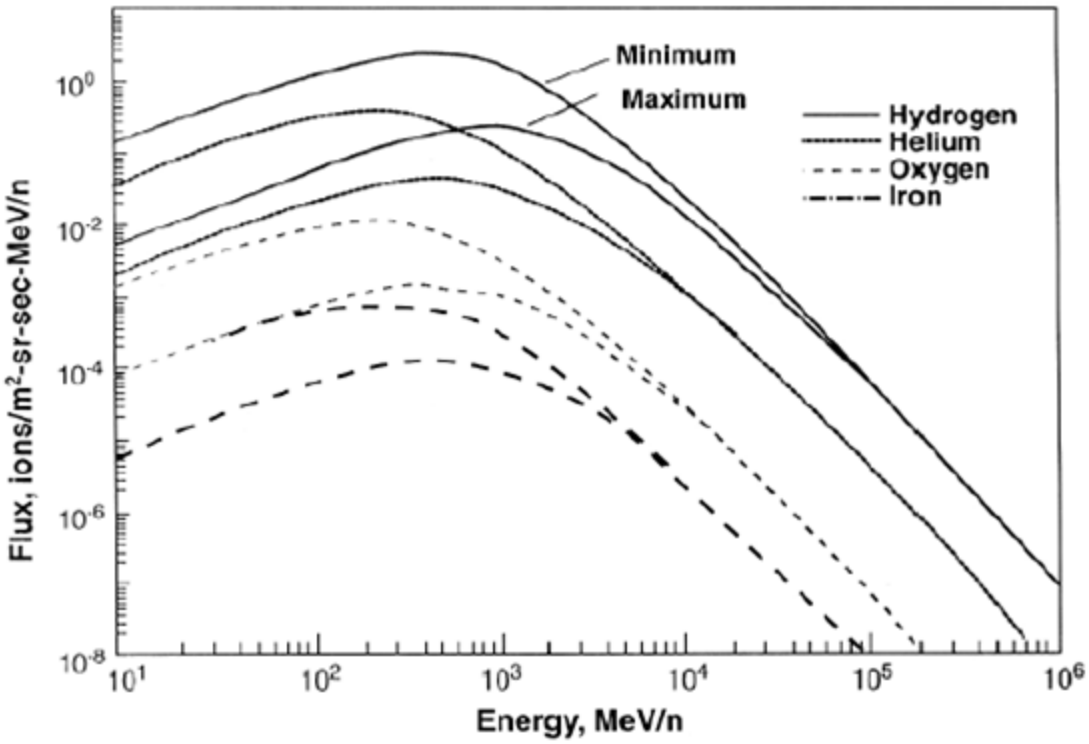

Figure 3.3 GCR fluxes for representative ions (Adams et al., 2005)

3.1.4 GCR Models

There are several different GCR models available. The most common models found in the literature are CREME96, Badhwar-O'Neill 2004 (BO'04), CREME2009, and Badhwar-O'Neill 2010 (BO'10). The Badhwar-O'Neill 2010 (BO'10) GCR model (O'Neill, 2010) is used in this study, primarily because it is the newest model available at the time of this analysis. Although the models are relatively similar, they are continually being updated with available data and differences in the flux profiles do exist. This can result in differences between radiation exposure estimates given in the relevant literature. Of greatest significance for this study, the BO'10 model has substantially lower flux profiles for both proton and alpha particles in the energy ranges below approximately 10^3 MeV/n. A comprehensive comparison of these models is given by Mrigakshi et al. (2012).

The BO'10 model provides the GCR energy spectrum for 1 to 10^6 MeV/n for elements with Z = 1 through Z = 94. This study only takes into account elements with Z = 1 through Z = 28, since the resulting dose equivalent for elements with Z greater than 28 provides a negligible contribution to the total dose equivalent (Simpson, 1983). The model output is the differential flux, given in units of particles-m^{-2}-sec^{-1}-sr^{-1}-MeV/n^{-1}, and is assumed to be isotropic.

The GCR model output used in this analysis is based on a solar modulation parameter value of 481 MV, corresponding to the 1977 solar minimum. This solar minimum is commonly used to provide a design basis in the literature because it results in the highest radiation exposure during the time period for which GCR data is available (Badhwar et al., 1994). However, the GCR model output used in this study represents the highest radiation exposure for a single day during the 1977 solar minimum. This is used to estimate radiation exposure values for long duration missions, and therefore results in conservative exposure estimates since the GCR environment may not result in such high exposure rates when averaged over longer duration. Future studies which apply the modeling techniques presented here should utilize a GCR model output which is scaled to match the length of the desired mission focus.

3.2 Radiation Interaction with Mass

As radiation moves through material, either shielding or tissue, it interacts with the surrounding medium. An understanding of these interaction mechanisms is essential to the radiation shielding problem. Particulate radiation can interact with the surrounding medium in a variety of ways including excitation, ionization, absorption, or nuclear fragmentation (Turner, 1995). Ionization is of concern because this is one of the primary mechanisms for biological damage (Robbins and Yang, 1994), but these interactions may also result in the creation of

secondary radiation effects. Additionally, nuclear fragmentation can change the composition of the flux profile, which is of particular concern for the space environment (Trovati et al., 2006). Although the space radiation environment is primarily composed of charged particles, the interactions of photons and neutrons with matter are also important. While these types of radiation do not initially comprise a significant portion of the space radiation environment, they are produced as secondary particles.

Primary interaction mechanisms of protons and other heavier, positively charged particles are excitation and ionization. As the charged particle passes near an orbital electron it may become excited, moving to a higher orbit, or cause it to uncouple from its nucleus, resulting in ionization. This secondary electron can then move on to cause further excitations and ionizations. These secondary electrons are called delta rays, which are a form of secondary radiation (NRC, 1996). Additionally, protons and other heavier charged particles may interact with the nuclei of the surrounding medium. Such nuclear interactions result in elastic collisions or inelastic atomic collisions, which can result in nuclear fragmentation. These fragmentation reactions, which can occur in either the projectile or target nucleus, can produce secondary particles such as neutrons, protons, mesons, and other heavier charged particles. Thus, this type of nuclear interaction can change the composition of the incident radiation as it passes through shielding material (Trovati et al., 2006).

Electrons also interact with material via excitation or ionization. These interactions are due to the electromagnetic force between the primary particle and the orbital electrons of the medium. Additionally, electrons may also interact with the nuclei of the medium. As these electron pass by the nucleus, the electrical field of the nucleus causes them to deflect and emit secondary gamma radiation, known as “bremsstrahlung” radiation (ions also emit

bremsstrahlung radiation, but this tends to be negligible at energies of interests for space radiation). For electrons, ionization and excitation are dominant at lower energies, while bremsstrahlung dominates at higher energies.

Neutrons fundamentally differ in their interaction with the surrounding material. They are uncharged, therefore interaction with surrounding electrons is negligible. These particles primarily interact with surrounding nuclei and this may result in collisions or absorption of the neutron. Elastic or inelastic collisions generally result in energy transfer to the surrounding atoms as the neutron passes through the material. In some cases, the neutron will pass completely through the material; however, if the neutron loses enough energy it can become thermalized (i.e. it has approximately the same energy as the surrounding medium) and may be absorbed by a nearby nucleus. These nuclear interactions can cause fragmentation, resulting in the creation of additional secondary particles. While neutrons comprise a negligible portion of the space radiation environment, they become a significant factor because they are frequently formed as secondary particles, due to the primary particle's interaction with shielding material or the target material (Trovati et al., 2006).

Photons deposit energy in matter through three processes: the photoelectric effect, Compton scattering, and pair production. Any of these interactions may result in the ionization of surrounding material and therefore contribute to biological damage in the target medium. Again, photons are not a significant source in the space radiation environment, however they become a concern since they are formed as a result of particle interaction as the primary flux passes through shielding or target material.

While most radiation interactions deposit energy in the surrounding medium, causing ionizations and potentially resulting in damage, one of the interactions that must be accounted

for in the space environment are the nuclear interactions. These nuclear interactions fundamentally alter the composition of the flux as the radiation passes through material, in either shielding or tissue. This can result in significant differences in the biological effects of the incident radiation. The secondary particles and radiation formed may even cause greater biological damage than the initial radiation. This can also result in differences between exposures in different parts of the body, such as between the skin or blood forming organs (BFO), in what is known as "body-shielding" or "self-shielding." Therefore, alterations in the composition of the radiation fields and generation of secondary radiation must be accounted for, necessitating the use of radiation transport codes that solve for the complex interactions between the incident radiation and material.

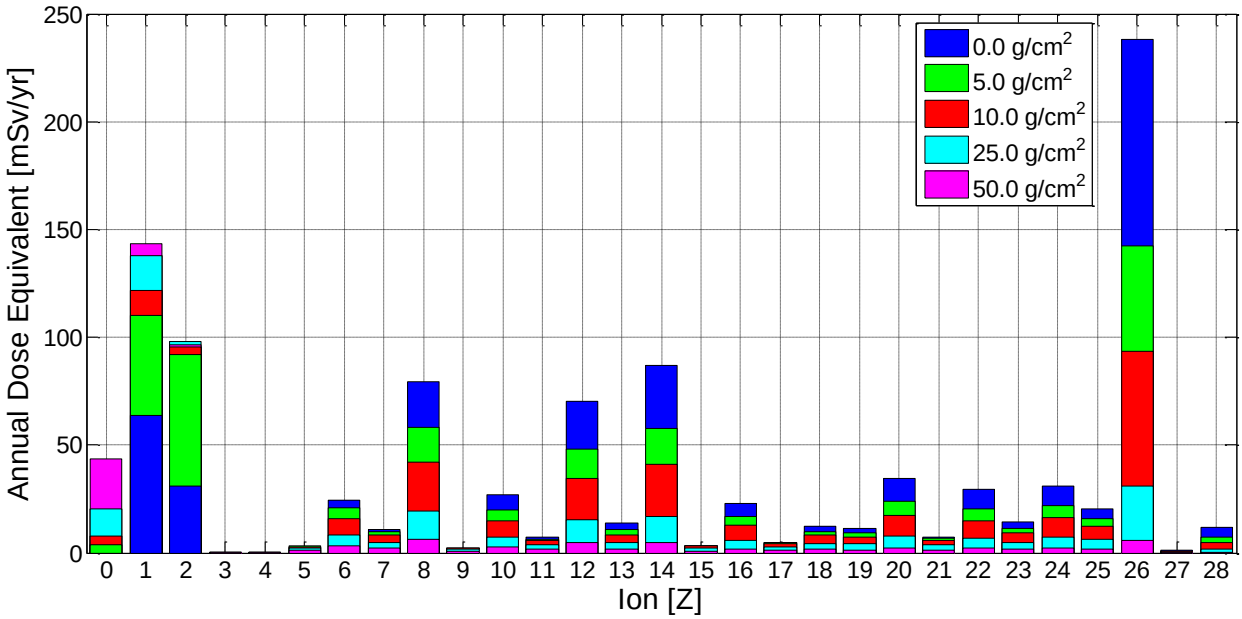

Figure 3.4 Individual GCR Ion Contribution to Annual Dose Equivalent Behind Different Thickness of Aluminum Shielding for 1977 Solar Minimum GCR Flux (BO'10 GCR model transported using HZETRN2010)

3.3 Radiation Protection Quantities

The following sections provide an introduction to the relevant radiation protection quantities and units commonly seen in literature and utilized in this work. These quantities are designed to allow the comparison of different types of radiation exposure and correlate this exposure to chemical or biological effects in a target. As the following sections demonstrate, this is especially difficult in the field of space radiation. Most experience with radiation and its biological effects are based on terrestrial radiation sources, which are very different from those found in space. Therefore, large uncertainties can exist when applying these terrestrially derived quantities to the space environment. An excellent summary of this topic can be found in the 2009 NASA publication *Human Health and Performance Risks of Space Exploration Missions*.

3.3.1 Absorbed Dose

The amount of damage caused by radiation is related to the amount of energy deposited in the target material. This quantity is the absorbed dose, or simply dose, and is defined as the energy absorbed per unit mass from ionizing radiation. This is commonly expressed in the SI unit of greys (Gy), defined as 1 J per kg of mass. An older unit still seen in literature is the rad, defined as 1 erg per g. Therefore, 1 Gy is equivalent to 100 rad. The absorbed dose rate, $\dot{D}_i$, at a point, or the point dose, is approximated by,

$$\dot{D}_i = \int_0^\infty S_i(T)\Psi_i(T)\,\mathrm{d}T\,, \tag{3.1}$$

where Ψ_i is the differential flux as a function of kinetic energy, T, for particle type i, and S_i is the mass stopping power as a function of kinetic energy, T, for particle type i (Turner, 1995). The

mass stopping power is the stopping power, *-dT/dx*, divided by the target material density (Turner, 1995),

$$S_i(T) = \frac{1}{\rho}\left(\frac{-dT}{dx}\right)_i . \tag{3.2}$$

The stopping power is the average rate of energy loss of a heavy charged particle in a medium, usually given in units of keV per µm of water. The energy *lost* in a target is not necessarily equal to the energy *absorbed* in target; therefore, Eq. (3.1) is only an approximation of the absorbed dose.

3.3.2 Linear Energy Transfer (LET)

Another important quantity is the linear energy transfer (LET), which is closely related to the stopping power. LET is defined as the quotient of dT_{Δ} to *dl*, where dT_{Δ} is the mean energy lost by the charged particles in a medium, due to electronic interactions in traversing a distance *dl*, minus the mean sum of the kinetic energies in excess of Δ of all the electrons released by the charged particles (ICRU, 2011). Therefore, this quantity looks at localized interactions between charged particles with electrons in the medium. Thus, the Δ term is designed to exclude the energy imparted to secondary electrons which leave the "local" region. Since charged particle radiation interactions within a medium are dominated by the interaction with medium electrons, LET and stopping power are similar quantities. If the unrestricted linear energy transfer ($\Delta = \infty$) is observed, this quantity is equal to the electronic interaction contribution to the unrestricted stopping power ($\Delta = \infty$) and roughly equivalent to the total unrestricted stopping power.

It is known that the distribution of energy deposition in tissue can affect the biological response. Therefore, LET is a useful quantity because it relates the amount of energy deposited

per unit length and is commonly given in units of keV per micrometer. The HZE particles which comprise the GCR spectrum are also often referred to as "high LET" radiation because of their high LET values which stem from both their energy and high charge characteristics. This is in contrast to "low LET" radiation, such as photons, which deposit significantly less energy and cause fewer ionizations per unit of distance traveled in a target material. The Bethe formula for stopping power of a uniform medium for a heavy charged particle demonstrates that stopping power, and therefore LET, is a function of not only a particle's energy, but it is also proportional to the square of the particle's charge. This is given by,

$$\frac{-dT}{dx} = \frac{4\pi k_0^2 z^2 e^4 n}{m_e c^2 \beta^2}\left[\ln\frac{2m_e c^2\beta^2}{I(1-\beta^2)} - \beta^2\right], \tag{3.3}$$

where z is the atomic number of the heavy particle, e is the magnitude of the electron charge, n is the number of electrons per unit volume is the medium, m_e is the electron rest mass, c is the speed of light in a vacuum, β is the speed of the particle relative to c ($\beta = v/c$), I is the mean excitation energy of the medium, and the constant $k_0 = 8.99\text{x}10^9$ $\text{Nm}^{-2}\text{C}^{-2}$ (Turner, 1995). It is important to note that when calculating the actual stopping power of a material for a given particle type, correction factors are often applied to the Bethe formula to account for various factors (Wilson et. al, 1995).

3.3.3 Dose Equivalent

The damage incurred from a given absorbed dose is often different for different types of radiation. In order to account for this, the dose equivalent was introduced, which factors the absorbed dose by a unitless quality factor, Q. This quality factor accounts for the Relative Biological Effectiveness (RBE) of different types of radiation. Therefore, the dose equivalent

allows the biological effect of different types of radiation to be expressed on a common scale. In 1990, the International Commission on Radiological Protection defined the quality factor as a function of LET in water, commonly known as the ICRP 60 quality factor (ICRP, 1991), shown in Table 3.1.

Table 3.1 ICRP 60 Dose Equivalent Quality Factors (ICRP, 1991)

LET, L [keV/μm in water]	**Q**
<10	1
10 – 100	0.32L – 2.2
>100	$300/\sqrt{L}$

Therefore the dose equivalent rate at a point, $\dot{H}_i$, or point dose equivalent rate, for particle type *i*, is given by (Turner, 1995),

$$\dot{H}_i = \int_{T=0}^{T=\infty} Q_i\left(LET(T)\right) S_i(T)\,\Psi_i(T)\,\mathrm{d}T\,. \tag{3.4}$$

The SI unit for dose equivalent is the Sievert, Sv. Related to the absorbed dose value of rad is the rem, which is still commonly seen in literature for dose equivalent. Similarly, 1 Sv is equivalent to 100 rem. The dose equivalent for each particle type is additive, resulting in the total point dose equivalent rate, $\dot{H}$, being given by,

$$\dot{H} = \sum_{i=1}^{N} \dot{H}_i\,. \tag{3.5}$$

3.3.4 Equivalent Dose, Effective Dose, and Effective Dose Equivalent

There are numerous other methods which attempt to quantify the biological impact of radiation exposure. One of the most common quantities is the equivalent dose. This was originally introduced in ICRP 60 (1991) and was designed to be broadly comparable to dose equivalent and better quantify the relationship between absorbed dose and the resulting

stochastic effects. This quantity uses a radiation weighting factor, w_R, multiplied by the absorbed dose averaged over a tissue, $D_{T,R}$,

$$H_T = \sum_R w_R D_{T,R} \,. \tag{3.6}$$

This utilizes the radiation weighting factors shown below in Table 3.2.

Table 3.2 Equivalent Dose Radiation Weighting Factors (ICRP 60, 1991)

Radiation type	**Radiation weighting factor, w_R**
Photons	1
Electrons and muons	1
Protons and charged pions	2
Alpha particles, fission fragments, heavy ions	20
Neutrons	$5.0 + 17.0e^{-[ln(2*E_n)]^2/6}$

*Note: although these factors have been updated by ICRP 103 (2007), these values are still used for space applications

The equivalent dose provides a method for quantifying the biological effects on a given tissue. However, according to the ICRP, "the relationship between the probability of stochastic effects and equivalent dose is found also to vary with the organ or tissue irradiated. It is, therefore, appropriate to define a further quantity, derived from equivalent dose, to indicate the combination of different doses to several different tissues in a way which is likely to correlate well with the total of the stochastic effects" (ICRP 60, 1991). This led to the introduction of the effective dose, E, which combines the equivalent dose of various important tissues which are multiplied by a tissue weighting factor, w_T, given in Table 3.3,

$$E = \sum_T w_T H_T \,. \tag{3.7}$$

"These tissue weighting factors, w_T, attempt to equate the impact an individual tissue has on the entire human system relative to the previously described dose equivalent" (NASA, 2010).

Table 3.3 Equivalent Dose Tissue Weighting Factors (ICRP 60, 1991)**

Tissue	Tissue weighting factor, w_T
Gonads	0.20
Bone Marrow (red)	0.12
Colon	0.12
Lung	0.12
Stomach	0.12
Bladder	0.05
Breast	0.05
Liver	0.05
Esophagus	0.05
Thyroid	0.05
Skin	0.01
Bone Surface	0.01
Remainder*	0.05

* Remainder tissues: Adrenals, Extrathoracic (ET) region, Gall bladder, Heart, Kidneys, Lymphatic nodes, Muscle, Oral mucosa, Pancreas, Prostate (male), Small intestine, Spleen, Thymus, Uterus/cervix (female).
** Note: although these factors have been updated by ICRP 103 (2007), these values are still used for space applications

The above radiation weighting factors for equivalent dose calculations show that these factors are primarily geared toward terrestrial radiation sources, which only have a minor contribution from HZE particles. Utilizing a uniform weighting factor of 20 for the entire GCR spectrum is not appropriate for determining the biological impact of these particles and the terrestrially geared calculation of equivalent dose is not appropriate for use in space applications. Therefore, NASA and the space radiation community have adopted a slightly different method for calculating effective dose (Cucinotta and Durante, 2009). Rather than using the radiation weighting factors, which do not appropriately account for the space HZE environment, the equivalent dose in a tissue is calculated with the ICRP 60 quality factors using,

$$H_T = \sum_R \int Q_R(LET(T)) D_{T,R}(T) dT \,, \tag{3.8}$$

where, Q_R is the ICRP quality factor as a function of LET, and $D_{T,R}$ is the absorbed dose averaged over a tissue, integrated over the range of kinetic energy, T, for radiation type R. The

effective dose is then calculated using the ICRP 60 tissue weighting factors using Eq. (3.7). This is sometimes referred to as the effective dose equivalent, to distinguish it from the traditional effective dose as defined by the NCRP for terrestrial applications. It is important to note that the tissue weighting factors for equivalent dose calculation were updated in ICRP 103 (2007); however, this update came after the release of the NCRP's recommendation for LEO (NCRP 132, 2000) and it is common for these older values to still be used for calculating effective dose equivalent (Clowdsley et al. 2004; Cucinotta and Durante., 2009).

3.3.5 Grey-Equivalent

The quality factors and weighting factors used in the calculation of dose equivalent and effective dose equivalent are based upon the relating the stochastic biological effects of radiation. Therefore, the Grey-Equivalent (Gy-Eq) was introduced to account for deterministic effects (NCRP 132, 2000). The Gy-Eq for a given tissue is calculated by determining the average dose for a tissue and multiplying the dose for each radiation type by the appropriate RBE value, given in Table 3.4. "This quantity is analogous to the dose equivalent, as it applies a Q-like effectiveness value to the absorbed dose, but it applies only to deterministic effects in individual organs" (NASA, 2010).

Table 3.4 Gy-Eq RBE Values (NCRP 132, 2000)

Particle Type	**RBE**
1 to 5 MeV neutrons	6.0
5 to 50 MeV neutrons	3.5
Heavy ions (e.g. helium, carbon, neon, argon)	2.5
Protons > 2 MeV	1.5

3.3.6 Quantities Used in this Study

With the evolution of radiation analysis, the complexity of determining the latest radiation protection quantities has greatly increased. Accurately determining the equivalent dose, effective dose, or Gy-Eq for a specific organ requires the use of a human phantom model. There are several types of human phantom models available, including the Computerized Anatomical Man (CAM)/Computerized Anatomical Female (CAF) models (Billings and Yucker, 1973; Yucker and Huston, 1990; Yucker and Reck, 1992) and Male Adult voXel (MAX)/Female Adult voXel (FAX) models (Kramer et al., 2003; Kramer et al., 2004). Because of the shielding provided by the body to organs and tissues, these human phantom models are necessary for accurately determining the absorbed dose for individual tissues as well as the effective dose for the individual. This is particularly true for the space radiation environment, where the shielding provided by the rest of the body can significantly alter the flux profile seen by a given tissue and, therefore, affect the level of radiation exposure. Due to the complexity of integrating these human phantom models, they are not utilized in this phase of the research. However, utilizing these advanced models is essential for determining an accurate picture of the biological effects of radiation, and integrating this capability into the current body of work is identified as a priority for future efforts.

The radiation protection quantity primarily used in this study is the dose equivalent evaluated at a point inside the shielding, i.e. the point dose equivalent. Although this does not allow for direct comparison to radiation exposure limits, which are often expressed in effective dose and organ dose Gy-Eq, it does allow for a relative comparison of the shielding efficacy, as well as enable faster computation times, so that a large array of design variables may be evaluated. It should be understood that the resulting effective dose values for any subsequent

analysis will usually be some fraction of the reported point dose equivalent values due to the self-shielding of the tissue in the human body.

3.4 Health Hazards

3.4.1 Basis for Radiation Damage

As radiation moves through material it deposits energy, resulting in the excitation and ionization of the surrounding atoms and molecules. This also results in the production of secondary electrons, which can produce additional excitation and ionization in a cascading effect. This ionizing radiation produces chemically active molecules that can have potentially damaging biological results.

Biological damage is primarily the consequence of damage to key molecules within a cell, especially DNA molecules. This damage can occur directly or indirectly, and "both of these mechanisms can generate sufficient damage to cause cellular death, DNA mutation, or abnormal cellular function" (Cucinotta and Durante, 2009). Direct damage occurs through the direct interaction between radiation and key molecules. This can damage DNA and even result in single or double strand breaks as a result of interaction with a heavy radiation particle (Hall and Cox, 1994). Indirect effects are the result of chemically active molecules, created as a product of ionizing radiation, disrupting key molecules. Since tissue is primarily composed of water, the most common interaction is the ionization of water molecules. The ions produced are highly energetic and highly reactive, with the most common interaction resulting in the production of a hydroxyl radical (OH). A radical, or "free radical," is defined as a highly reactive atom or molecule with an unpaired electron in its outer shell. These free radicals, once formed, can then interact with DNA or other key molecules within a cell.

Cells have the capability to repair some damage caused by radiation. If damage occurs within a cell that it is not able to repair, there are several potential outcomes which include mutation, cell death, or the cell becoming unable to reproduce, with these later two outcomes often occurring as a result of mutation. Susceptibility of a given cell to later of these two outcomes is influenced by several factors that affect the cell's "radiosensitivity." The radiosensitivity of a cell type increases with its rate of division and decreases according to its degree of specialization (Stabin, 2007). For example, the cells which line the gastrointestinal tract have a high cellular turnover rate and are, therefore, more radiosensitive than other cell types.

The biological effects of radiation exposure are usually grouped into deterministic and stochastic effects (ICRP, 2007) or short and long term effects. Short term effects are wholly deterministic, while long term effects can be either deterministic or stochastic. As will be discussed in the following section, deterministic effects are caused by large radiation exposures incurred in a short period of time (i.e. high dose rates), with higher dose rates leading to increasingly severe deterministic effects. In the space radiation environment these would be the result of exposure to SPE radiation. Stochastic effects are primarily driven by low intensity, long term exposure to the GCR component of the space radiation environment, although acute exposures also contribute to the probability of incurring these effects. Therefore, stochastic effects are the primary concern in this analysis since SPEs will be effectively shielded by appropriate active radiation shields.

3.4.2 Short Term Deterministic Effects

The effects of large, acute radiation doses are also known as acute or deterministic effects. These deterministic effects are called so because "the statistical fluctuations in the number of affected cells are very small compared to the number of cells required to reach the threshold" (ICRP 1991). The results begin to appear at a certain exposure threshold and become more severe with increased exposure. Deterministic effects are usually immediate or short-term, with symptoms appearing soon after exposure.

"Early radiation effects usually are related to a significant fraction of cell loss that exceeds the threshold for impairment of function in a tissue" (Cucinotta and Durante, 2009). The resulting biological symptoms are often generically referred to as Acute Radiation Syndrome (ARS) and can range from mild radiation sickness to death, in the case of extremely high exposures. Symptoms will manifest first in tissues which have a high level of radiosensitivity and the health consequences will be determined by the affected tissue's function. In the space environment, deterministic effects would be caused by large, acute radiation doses as a result of exposure to an SPE. Although SPEs will not be examined here, Table 3.5 gives a list of deterministic effects as a function of exposure to provide some context of the magnitude of these exposure values

Table 3.5 Acute Radiation Dose Effects (Buckley, 2006)

Dose [mSv]	Predicted Physiological Effects
100 – 500	No obvious effects, some minor changes in blood counts
500 – 1,000	Fatigue; 5-10% experience nausea and vomiting for 1 day; no deaths anticipated
1,000 – 2,000	25-50% experience nausea and vomiting for 1 day; no deaths anticipated
2,000 – 3,500	75% reduction in circulating blood elements; most experience nausea and vomiting; loss of appetite, diarrhea, and minor hemorrhage also seen; death in 5 – 50% of those exposed ("bone marrow syndrome")
3,500 – 5,500	Nearly all experience nausea and vomiting on first day followed by fever, hemorrhage, diarrhea, and emaciation; death of 50 – 90% within 6 weeks; survivors convalesce for about 6 months (overlap of "bone marrow syndrome" and "GI syndrome"
5,500 – 7,500	All experience nausea and vomiting within 4 hours, followed by severe symptoms of radiation sickness; death of up to 100%
7,500 – 10,000	Severe nausea and vomiting may continue into the third day; survival time reduced to less than 2.5 weeks
10,000 – 20,000	Nausea and vomiting within 1 – 2 hours; all die within two weeks
45,000	Incapacitation within hours; acute central nervous system syndrome due to radiation can be seen (disorientation, ataxia, convulsions, coma); all die within days

3.4.3 Long Term Deterministic Effects

There are also several types of deterministic effects which are long-term or latent effects. These include radiation induced cataracts (Cucinotta et al., 2001), central nervous system damage (Cucinotta et al., 2009), heart disease, and other degenerative health effects (Huff and Cucinotta, 2009). Although deterministic limits have been determined for more common forms of low LET radiation, limits for the high LET space environment are difficult to determine since there is little terrestrial experience with similar radiation sources.

3.4.4 Long Term Stochastic Effects

As the name implies, stochastic effects are predicted by a statistical probability of occurrence, with increased exposure resulting in an increased probability of the symptom

occurring. These are long term effects that could result in the appearance of cancer or a genetic chromosomal defect, which could be passed to offspring, and are thought to be caused by mutations in the DNA of tissue throughout the body. These effects also have a long latency period, with consequences such as cancer typically occurring 2 – 20 years after the period of exposure. The risk of producing inheritable effects from space exposure is probably quite low (NRC, 1996); therefore, the primary stochastic risk factor is the induction of cancer. Risks of radiation induced cancer are also a complex function of other factors such as gender, age, diet, genetic predisposition, and exposure to carcinogens (such as cigarettes). Again, there is little experience with the risk factors and levels of probability associated with high LET radiation exposure, such as would be found in the space environment. Current stochastic estimates are based on terrestrial sources of data, which primarily consist of radiation workers, atomic blast survivors, and patients who were treated therapeutically with radiation (Cucinotta and Durante, 2009).

3.4.5 Exposure Limits

Mission specific exposure limits have been delegated to the individual programs, in the NASA Space Flight Human System Standard Volume 2 (NASA-STD-3001v2) (NASA, 2011), and have not yet been established. However, future mission limits must comply with the career and short term Permissible Exposure Limits (PELs) established in the NASA Space Flight Human System Standard Volume 1 (NASA-STD-3001v1) (NASA, 2007). These PELs include "age- and gender-dependent career cancer risks limits and dose limits for short–term and career non-cancer effects." The short term exposure limits are in place to prevent acute radiation

exposure effects (such as lethality, vomiting, and nausea), and the PELs for short-term and career non-cancer effects are shown in Table 3.6.

Table 3.6 Dose Limits for Short-Term and Career Non-Cancer Effects
[mGy-Eq, or mGy where specified] (NASA, 2007)

Organ	30 day limit	1 Year Limit	Career
Lens*	1000	2000	4000
Skin	1500	3000	4000
BFO	250	500	Not applicable
Heart**	250	500	1000
CNS***	500	1000	1500
CNS*** ($Z \geq 10$)	-	100 mGy	250 mGy

*Lens limits are intended to prevent early (< 5 yr) severe cataracts (e.g., from a solar particle event). An additional cataract risk exists at lower doses from cosmic rays for sub-clinical cataracts, which may progress to severe types after long latency (> 5 yr) and are not preventable by existing mitigation measures; however, they are deemed an acceptable risk to the program.
**Heart doses calculated as average over heart muscle and adjacent arteries.
***CNS limits should be calculated at the hippocampus.

The PELs for cancer risks are established such that that astronaut career radiation exposure "shall not exceed 3 percent risk of exposure induced death (REID) for fatal cancer … at a 95 percent confidence level using a statistical assessment of the uncertainties in the risk projection calculations" (NASA, 2007). Cancer risk evaluations are made using the double detriment life-table, for an average population, that contains age- and gender-dependent rates of death, including from cancer, combined with a radiation cancer mortality rate model (NCRP, 2000). These cancer mortality rates are based upon epidemiological data, primarily from data on atomic-bomb survivors in Japan, as well as radiation workers, patients who have undergone radiation treatment, and individuals exposed to radiation accidents such as Chernobyl (Cucinotta and Durante, 2009). These exposures are primarily due to low-LET gamma ray exposure and, therefore, this data must be extrapolated to account for the high-LET space radiation environment. Additionally, this epidemiological data is primarily based on large acute exposures and must be adjusted to account for low dose rate exposures.

The additional level of conservatism, due to the application of the 95% confidence interval, "accounts for uncertainties in epidemiology data, dose-rate factors, individual biological response, organ dose assessment errors, and uncertainties associated with measurement and the environment" (NASA, 2010). Because the uncertainties in many of these areas are large, applying the 95% confidence level may make the career dose limits rather restrictive. It is hoped that resolving these uncertainties will increase the acceptable exposure limits. Example career GCR exposure limits for a 1 year mission are shown in Table 3.7.

Table 3.7 Example Career Effective Dose Limits for a 1 Year Mission (NASA, 2010)

Age [yr]	Male 3% REID 95% CL for GCR Exposure [mSv]	Female 3% REID 95% CL for GCR Exposure [mSv]
30	163	124
35	189	145
40	211	163
45	250	197
50	303	242

These limits are a function of both age and gender, in accordance with the recommendation from the NCRP Report No. 98 (1989). In general, exposure limits for females are lower due to their higher risks of cancer in the breast, ovaries, and lungs (NCRP, 2000). Additionally, exposure limits increase with age. There are many factors that contribute to this, but one can expect that risk decreases "with age at exposure because the distribution of latency for tumor development would extend beyond the expected life span at older exposure ages" (Cucinotta et al., 2011).

Individual mission limits must be established such that astronauts do not violate these career limits. However, in addition to these limits, astronaut radiation exposure is guided by the "as low as reasonably achievable" (ALARA) principle. "The ALARA principle is a legal requirement intended to ensure astronaut safety. An important function of ALARA is to ensure

that astronauts do not approach radiation limits and that such limits are not considered as 'tolerance values'" (NASA, 2007). This principle also serves to enable mission and spacecraft design such that astronaut exposure should be kept at a minimum but not impose undue restrictions on the design such that the mission or design is no longer feasible.

Because cancer risk varies with both age and gender, these risks may also affect the crew composition for a given mission. An obvious crew selection choice would be to have older and more experienced astronauts participate in missions, due not only to their flight experience, but also to their lower risk levels. However, this must be balanced with the need to send younger astronauts as part of these same crews so that they may gain flight experience and learn from senior personnel. Not only are the exposure limits lower for younger astronauts, but applying a larger margin towards these limits may be considered so that sufficient exposure allowance is available for participation in future missions.

3.5 Radiation Transport Analysis Methods

Because of the complex interaction of radiation with material, there is no simple method for evaluating the resulting flux at a shielding boundary. Therefore, these problems must often be solved using transport theory. Transport theory, as applied to this problem, accounts for the interaction of the incident radiation as it passes through a medium based on the probabilities of various physical interactions. There are two primary approaches to solving this problem: deterministic transport calculations and stochastic calculations. Both of these methods rely on the knowledge of possible physical interactions and the probabilities associated with each.

Deterministic methods compute a solution by discretizing the problem and solving the Boltzmann equation, using linear algebra or other methods. This allows the determination of the

resulting radiation flux, for a given boundary condition, at all nodes in the discretization grid. Stochastic solutions use statistical methods to obtain a solution. Monte Carlo methods are a common stochastic solution and utilize a random walk of radiation particles through a given phase space. Each method has distinct advantages and disadvantages, which are also affected by how these methods are practically applied to the radiation analysis problem. A complete discussion and comparison of these methods is beyond the scope of this work; however, significant literature is available on this topic.

There are a variety of deterministic and stochastic tools which can be applied to the space radiation transport problem. Two common deterministic tools, developed specifically for the space radiation environment, are HZETRN (Wilson et. al, 1995; Slaba et. al, 2010a, 2010b), developed by NASA, and UPROP (Severn Communications Corporation, 1989), developed by the Naval Research Laboratory (NRL). However, other general deterministic codes can be used for space radiation analysis. Of the stochastic tools available, the most common are Monte Carlo methods. Many of these were developed for use in high energy physics calculations, but have found application in space radiation analysis. Some of the available codes are the MCNP series of Monte Carlo codes (James et al., 2009), developed at Los Alamos National Laboratory (LANL); HETC (Townsend et al., 2005); FLUKA (Fassò et al., 2005; Battistoni et al., 2007); and PHITS (Iwase et al., 2002), developed by the Japanese Atomic Energy Agency. There are also several Monte Carlo analysis toolkits, such as GEANT4 (Agostinelli et al., 2003), developed at CERN. Several studies are available in the literature that discuss and compare these various transport tools for use in the space radiation environment (Heinbockel et al., 2011; Lin et al., 2012).

In order to enable the rapid analysis times desired, NASA's High-Charge and Energy (HZE) radiation transport code, HZETRN, was selected for use in this work. Specifically, the HZETRN2010 version (Slaba et. al, 2010a, 2010b) is utilized. In addition to the high analysis speed enabled, HZETRN has extensive validation and verification (Wilson et al., 2005), as well as heritage in the NASA radiation analysis community.

Chapter 4

Rapid Analysis Model Development

In order to rapidly evaluate an active magnetic shielding design, the following model was developed. This model can be broken into two separate sections: the electromagnetic analytic solution segment, which allows the determination of the resulting flux due to the active magnetic field, and the radiation transport segment, which allows the determination of the flux due to the effects of any passive/structural shielding mass. NASA's High-Charge and Energy (HZE) radiation transport code, HZETRN 2010 (Wilson et. al, 1995; Slaba et. al, 2010a, 2010b), is utilized for the radiation transport segment and also allows for the determination of dose and dose equivalent values. The rapid evaluation method presented here focuses specifically on the solenoid design case; however, the principles developed can be modified and applied to the toroidal case as well.

The model is first developed for a solenoid magnetic field confined to an infinitely long cylinder. Once the analytical equations have been developed for the active magnetic field effects, HZETRN is introduced and some results are presented as a limiting case. The model is then applied to a more realistic cylinder of finite length and several analyses are presented using different thickness of aluminum shielding mass.

4.1 Model Development: Infinite Cylinder

4.1.1 Electromagnetic Analytic Solution Component

In order to simplify the complex calculations for determining the GCR flux inside a magnetic field, an infinitely long, cylindrically shaped, solenoid magnetic field is examined using the following assumptions:

1) the field is uniform in magnitude, and
2) the field is confined to the boundaries of the cylindrical geometry, as shown in Figure 4.1a.

The GCR flux passing through a point P in free space, with no magnetic field, can be written as

$$\Psi_i(T) = \int_{\theta=0}^{\theta=\pi} \int_{\phi=0}^{\phi=2\pi} \Phi_i(T) \sin\theta \, d\theta \, d\phi \,, \tag{4.1}$$

where Φ_i is the GCR omnidirectional, differential flux of particles, with charge Z_i, as a function of kinetic energy, T. The GCR flux passing through point P inside the solenoid magnetic field is determined by examining the approach angles θ and ϕ, shown in Figure 4.1b.

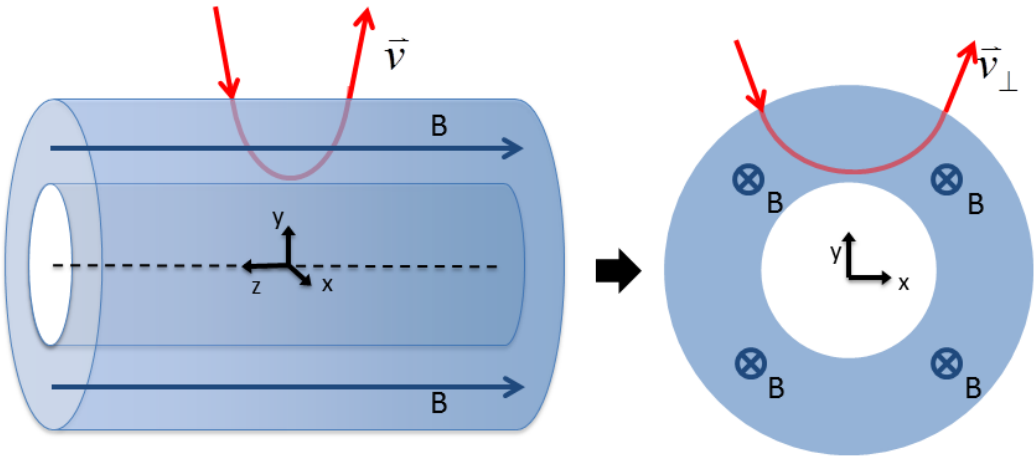

Figure 4.1a Infinite Cylinder Model and Cross Section

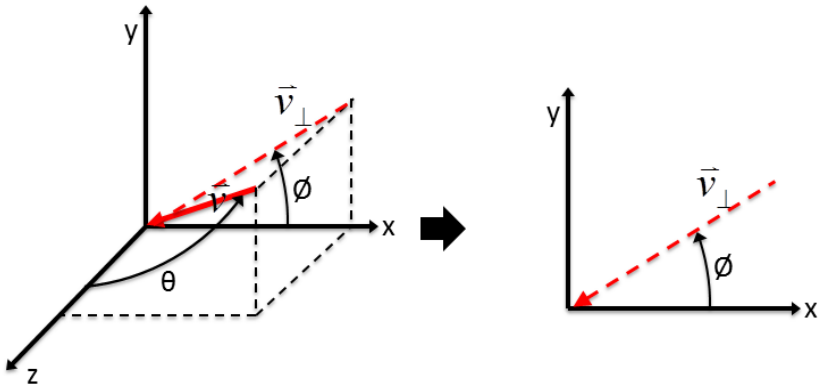

Figure 4.1b Infinite Cylinder Model Coordinates

4.1.1.1 Charged Particle Motion in a Magnetic Field

The motion of charged particles as they pass through a magnetic field is governed by the Lorentz force equation, given by

$$\vec{F} = q\vec{v} \times \vec{B}\,, \tag{4.2}$$

where q is the particle's charge, v is the particle's velocity, and B is the magnetic field strength. This force affects particle motion perpendicular to the magnetic field lines, while the velocity component parallel to the magnetic field remains unaffected. Since the high energy particles which comprise the GCR flux can have kinetic energies in the GeV/n range, relativistic equations must be utilized. The Lorentz force results in the particle's motion in the plane perpendicular to the magnetic field being circular. The equation for the radius of curvature of a charged particle in a magnetic field, which is also known as the Larmor radius or gyroradius (Griffiths, 1999), is given by

$$r_L = \frac{\gamma m_0 v_\perp}{qB}\,, \tag{4.3}$$

where γ is the Lorentz factor, m_0 is the particle's rest mass, and $v_\perp$ is the particle's velocity component perpendicular to the magnetic field.

Eq. (4.3) demonstrates that as the energy, and therefore velocity, of a given particle increases, its Larmor radius will also increase, making the particle more difficult to deflect. Additionally, a higher magnetic field strength, *B*, results in a smaller Larmor radius, causing greater deflection of a given particle.

4.1.1.2 Particle Motion in the x-y Plane

A cross section of the magnetic field in the *x-y* plane is examined, as shown in Figure 4.2. For a given approach angle, ϕ, the limiting trajectory for a particle passing through point P is associated with $\alpha = 0$, where α is the angle of incidence and is defined as the angle formed between the velocity vector of the particle and the surface of the magnetic field where the particle intersects it. A particle on this limiting trajectory will first enter the magnetic field at a glancing angle ($\alpha = 0$), and curve through the magnetic field along a circular path, with a radius equal to the particle's Larmor radius. This particle then exits the magnetic field, where the particle will pass through point P along the given approach angle, ϕ. Particles with a higher energy, and thus a larger Larmor radius, can pass through point P along the same angle, ϕ, but will enter the magnetic field at higher angles of incidence ($\alpha > 0$) and enter at a different point along the boundary of the magnetic field (illustrated on the left side of Figure 4.2). Particles with a lower energy, and thus a smaller Larmor radius, will be unable to pass through point P along the same angle, ϕ, regardless of angle of incidence, or where the particle intersects the magnetic field. Therefore, the Larmor radius associated with the limiting trajectory defines the lower limit, or cutoff energy, $T_{C/O}$, of a particle passing through point P from a given approach angle, ϕ, and varies as a function of this angle. This will be defined as the critical Larmor radius, $r_{L,0}$.

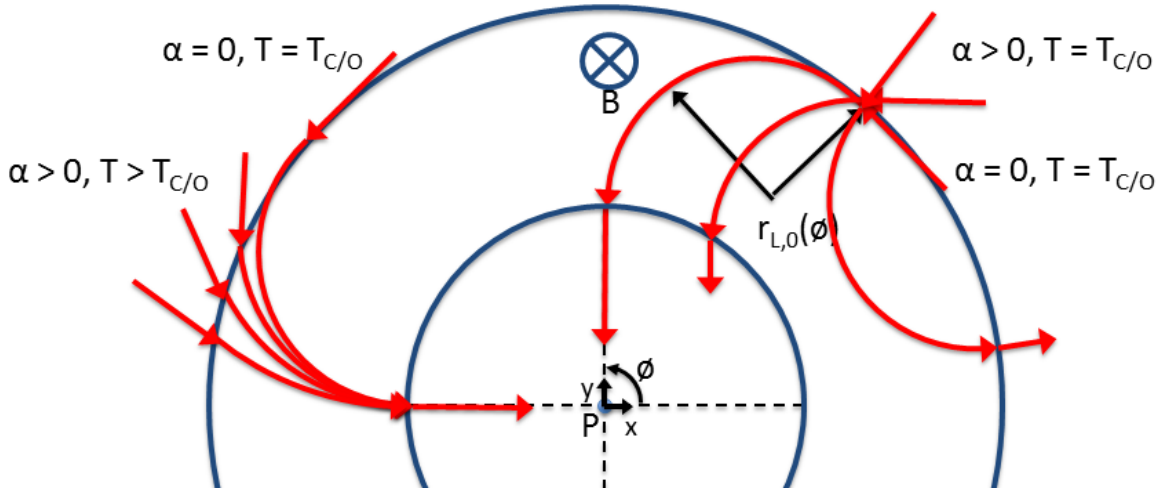

Figure 4.2 Flux Through Point P in *x*-*y* Plane

4.1.1.3 Critical Larmor Radius and Cutoff Energy

By examining this limiting case, a relationship between the critical Larmor radius ($r_{L,0}$) and the geometry of the magnetic field can be determined. This geometry is shown in Figure 4.3, where r_p is the radial distance of point P from the center, r_i is the inner radius of the magnetic field, and r_o is the outer radius of the magnetic field.

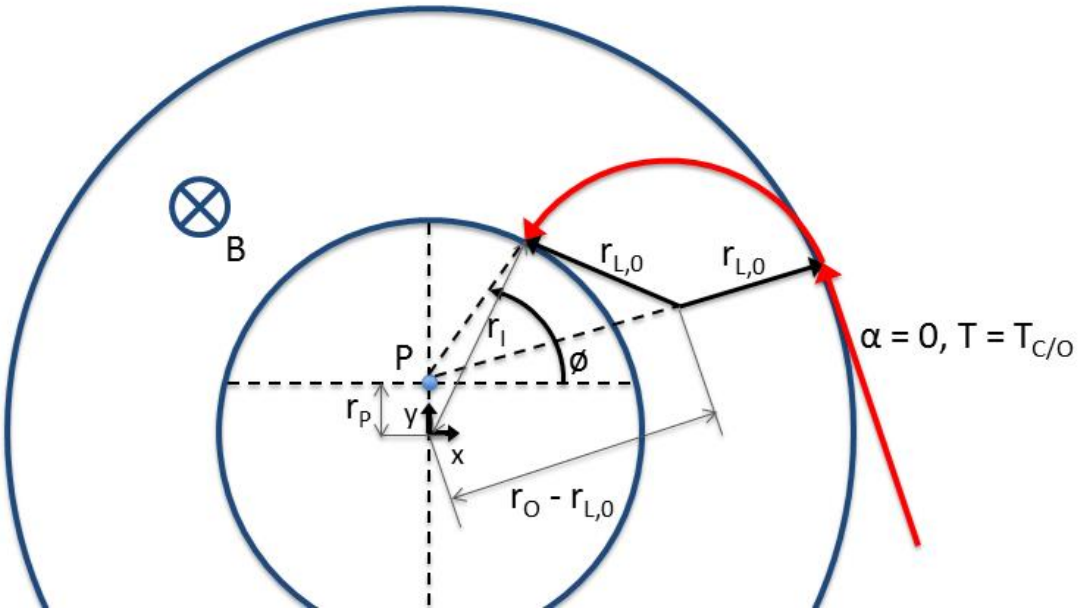

Figure 4.3 Geometry of Critical Radius

Using only the geometric relationships of the configuration in Figure 4.3, it can be shown that

$$r_{L,0}(\phi) = \frac{r_o^2 - r_i^2}{2(r_o - r_P \cos\phi)}. \tag{4.4}$$

By using Eq. (4.2), the particle's kinetic energy can be expressed as a function of only its Larmor radius by

$$T(r_L) = \sqrt{(r_L qBc)^2 + (m_0 c^2)^2} - m_0 c^2. \tag{4.5}$$

By substituting Eq. (4.4) for r_L in Eq. (4.5), the cutoff energy, $T_{C/O}$, may be expressed as a function of the angle ϕ.

$$T_{C/O}(\phi) = \sqrt{\left(\left(\frac{r_o^2 - r_i^2}{2(r_o - r_P \cos\phi)}\right) qBc\right)^2 + (m_0 c^2)^2} - m_0 c^2. \tag{4.6}$$

It is important to note that the cutoff energy refers to the minimum energy a particle can have and still pass through point P along approach angle ϕ. The above equations can be further extended to show how cutoff energy varies as a function of the approach angle θ for particles which do not lie entirely in the *x*-*y* plane.

4.1.1.4 Particle Motion in 3-Dimensions

As shown in Figure 4.1b, for a given approach angle θ, the particle's total velocity is related to its component perpendicular to the magnetic field by

$$v_\perp = v \sin\theta. \tag{4.7}$$

Drawing from Eq. (4.3), the Larmor radius as a function of the particle's total velocity and approach angle θ is written as

$$r_L(\theta) = \frac{\gamma m_0 v \sin\theta}{qB}. \tag{4.8}$$

Following Eq. (4.5), an expression relating the particle's kinetic energy and the Larmor radius is

$$T(\theta, r_L) = \sqrt{\left(\frac{r_L qBc}{\sin\theta}\right)^2 + \left(m_0 c^2\right)^2} - m_0 c^2. \tag{4.9}$$

The geometric relation for the particle's critical Larmor radius as a function of energy, Eq. (4.4), still applies. Therefore, the minimum kinetic energy, or cutoff energy ($T_{C/O}$), which will penetrate point P as a function of angles θ and ϕ, can be obtained by substituting Eq. (4.4) for r_L in Eq. (4.9).

$$T_{C/O}(\theta,\phi) = \sqrt{\left(\left(\frac{r_o^2 - r_i^2}{2\left(r_o - r_P\cos\phi\right)}\right)\frac{qBc}{\sin\theta}\right)^2 + \left(m_0 c^2\right)^2} - m_0 c^2. \tag{4.10}$$

The flux of particles with charge Z_i which passes through point P, where the cutoff energy ($T_{C/O}$) is given by Eq. (4.10), can be written as

$$\Psi_i(T) = \int_{\theta=0}^{\theta=\pi}\int_{\phi=0}^{\phi=2\pi} \Phi_i(T) H\left(T - T_{C/O}(\theta,\phi)\right)\sin\theta\, d\theta\, d\phi, \tag{4.11}$$

where H is the Heaviside unit step function.

4.1.1.5 Energy Cutoff

Eq. (4.10) shows that the cutoff energy varies with the approach angle θ as a function of $1/\sin\theta$. When $\theta = 90°$, the approach angle is perpendicular to the magnetic field direction, and thus the motion of any particle approaching from this angle will lie entirely in the x-y plane (i.e. it has no velocity component parallel to the magnetic field). As θ either decreases or increases

away from 90°, and the approach angle becomes more parallel to the central axis of the cylinder, the cutoff energy increases and approaches infinity, as shown in Figure 4.4. Particles which approach the habitat at these low "glancing angles" have only a small component of their velocity which lies perpendicular to the magnetic field, and thus, these particles have small Larmor radii and are easily bent away from the inner volume. For the theoretical infinite cylinder, the flux entering through the end of the cylinder is almost perfectly shielded. Although this property is not realistic, this case provides a good reference point as the lower limit for achievable dose equivalent values utilizing a solenoid design.

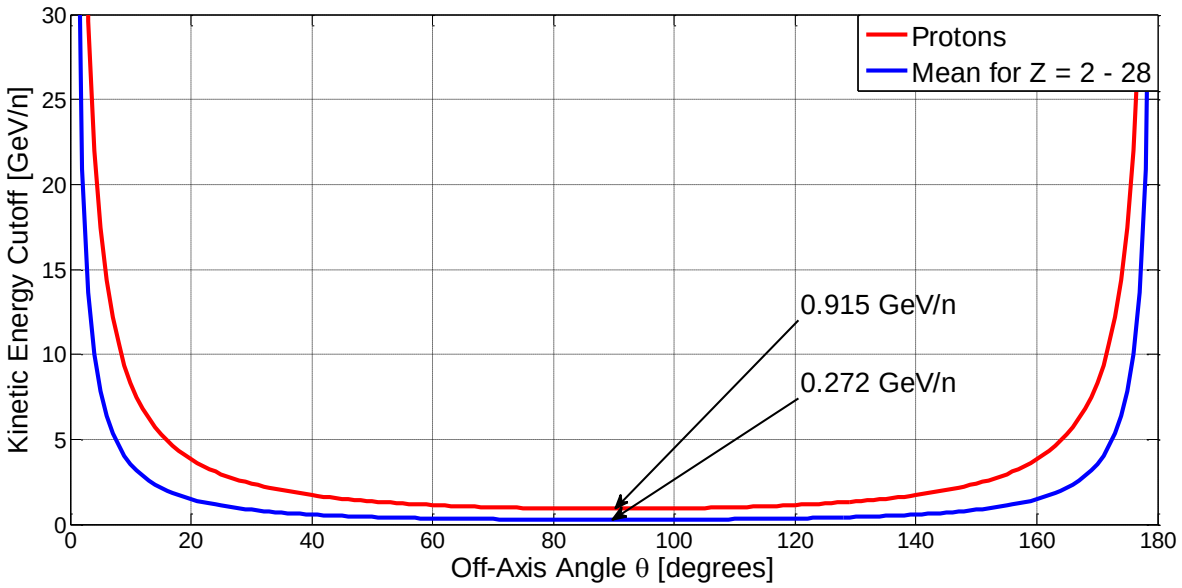

Figure 4.4 Infinite Cylinder Cutoff Energy for 8Tm Field (r_i = 4m, r_o = 12m, B = 1T)

4.1.2 Radiation Transport: Addition of HZETRN

The previously described analytical equations allow the determination of the flux at a point considering the effects of the magnetic field, but does not account for the effects of structural mass or any other passive shielding that may be part of the system. As previously demonstrated, these effects can be significant, as this mass can attenuate some of the incident

flux, as well as generate secondary particles. To determine the effects of mass, the High-Change and Energy (HZE) particle transport code HZETRN (Wilson et. al, 1995; Slaba et. al, 2010a, 2010b) is used for particle transport. In order to simplify the model, and reduce the run time required, the following simplifying assumptions are made:

1) all of the passive/structural shielding mass (habitat, structure, magnetic field architecture, etc.) is confined in the interior of the magnetic field, and
2) all of passive/structural shielding mass is represented by an appropriate volume of spherical shielding.

Based on these assumptions, the flux inside the magnetic field is determined using the equations outlined previously. This flux is then passed into the HZETRN code where it is transported through a uniform thickness of aluminum. HZETRN is used to determine the resulting dose equivalent in water, which is assumed to be a good approximation of the dose equivalent in tissue, using the ICRP 60 quality factor (ICRP, 1991). The computational run time for a single case is on the order of several seconds, and thus, an entire trade space of variables may be analyzed in minutes to hours depending on the level of fidelity and range of variables desired.

4.1.3 Passive Shielding Effects

Figure 4.5 shows how the dose equivalent is affected by passive/structural shielding thickness for various magnetic field bending powers (magnetic field strength multiplied by field thickness).

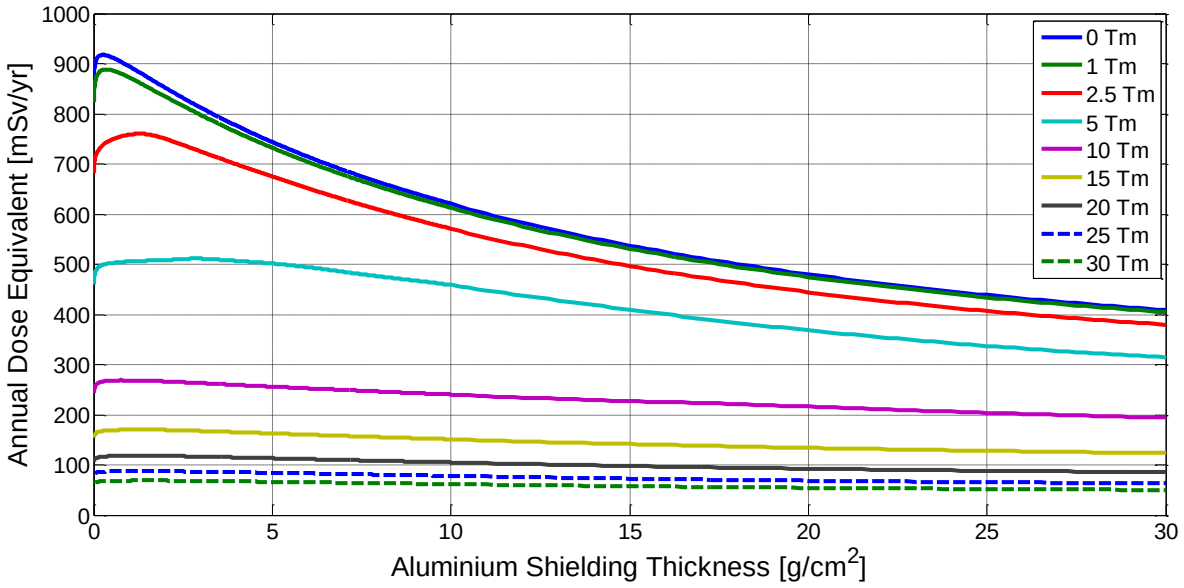

Figure 4.5 Depth vs. Dose Equivalent for Various Field Bending Powers (r_i = 4m, r_P = 0m)

Initially, the dose equivalent increases as the passive/structural shielding material thickness increases. As discussed previously, this is due to secondary particle production, particularly an increase in proton and alpha particles. As shown in Figure 4.6, the contribution to dose equivalent from protons and alpha particles initially increases, while the contribution from higher Z particles decreases. Neutrons (shown as Z=0) are also generated as secondary particles and contribute modestly to the total dose equivalent, although it is difficult to tell due to the scale of Figure 4.6.

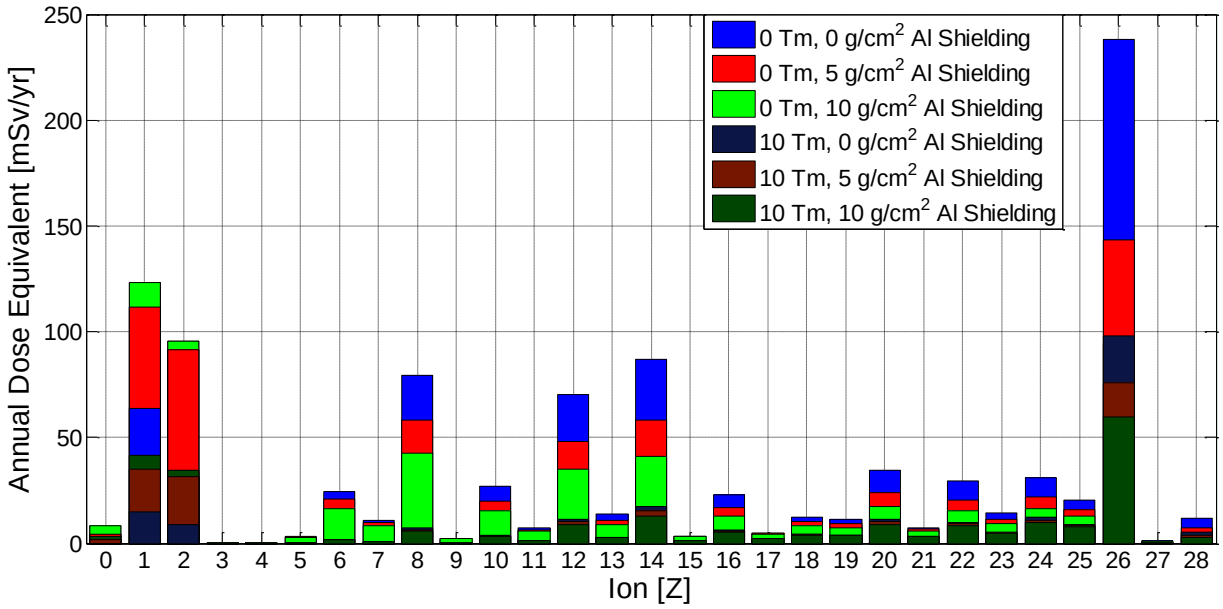

Figure 4.6 Ion Contribution to Total Annual Dose Equivalent (r_i = 4m, neutrons at Z=0)

4.1.4 Variation with Radial Distance

It is also interesting to see how the dose equivalent at point P varies as a function of the radial distance from the axial centerline of the cylindrical magnetic field (r_p). By plotting dose equivalent as a function of r_p, shown in Figure 4.7, it can be seen that for bending powers above 5 Tm the dose equivalent varies little. For low bending powers, the resulting dose equivalent decreases as r_p increases.

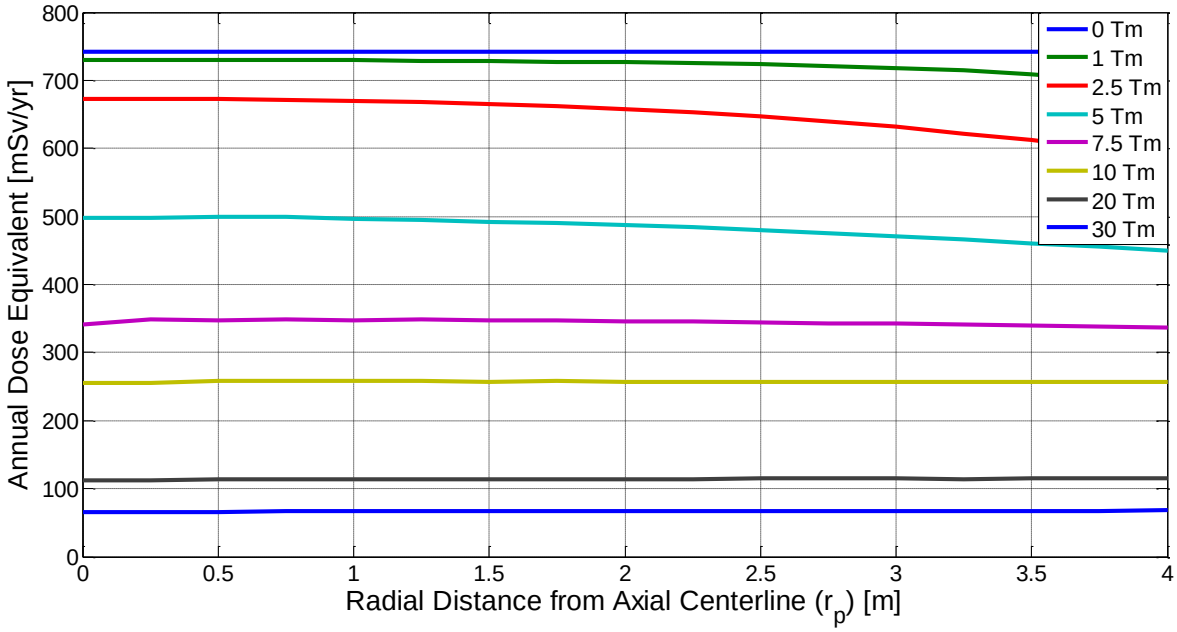

Figure 4.7 Dose Equivalent vs. Radial Distance from Axial Centerline of Infinite Cylinder Model (r_i = 4m. 5.0 g/cm^2 Al Shielding)

From this, it can be assumed that the dose equivalent determined at the axial centerline is either representative, or a conservative estimate, of the dose equivalent throughout the interior of the magnetic field. By setting r_p equal to zero in Eq. (4.10), an equation for the cutoff energy at the axial centerline is obtained. This causes the cosϕ term to drop out, resulting in the cutoff energy as a function of the angle θ only. Therefore, the flux calculation can be further simplified by determining the resulting dose equivalent at the axial centerline and eliminating the need to integrate over ϕ, reducing the overall computation time, by using Eq. (4.12) below:

$$\Psi_{i,Center}(T) = 2\pi \int_{\theta=0}^{\theta=\pi} \Phi_i(T) H\left(T - T_{C/O,Center}(\theta)\right) \sin\theta \, d\theta, \tag{4.12}$$

where,

$$T_{C/O,Center}(\theta) = \sqrt{\left(\left(\frac{r_o^2 - r_i^2}{2r_o}\right)\frac{qBc}{\sin\theta}\right)^2 + \left(m_0c^2\right)^2} - m_0c^2. \tag{4.13}$$

4.1.5 Trade Study Results

The following results are easily created using the rapid analysis model developed here and highlight the design trades between magnetic field strength, magnetic field thickness, and passive/structural shielding mass. Although the infinite cylinder data presented is only theoretical, the plots provide useful insight into the effects of the magnetic field and serve as a limiting case for reference and provide useful insights into the solenoid active shielding design. Each of the trade study results shown were generates in only a few hours, where a similar analysis using Monte Carlo methods would take significantly longer.

Figure 4.8a shows the annual dose equivalent for a range of magnetic field strengths and field thicknesses with 5.0 g/cm^2 of passive/structural aluminum shielding. Additionally, a related plot can be generated, Figure 4.8b, which shows the maximum mission duration achievable for a selected dose equivalent limit (selected to be 150 mSv for the plots shown).

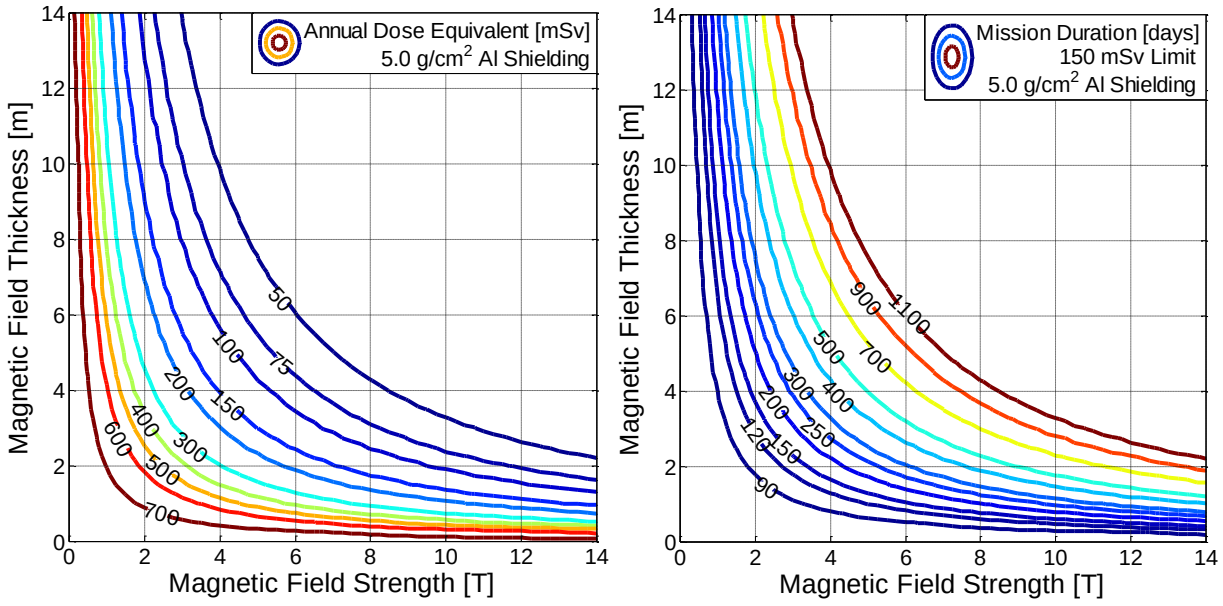

Figure 4.8 Infinite Cylinder Model, 5.0 g/cm^2 Passive Aluminum Shielding (r_i = 4m)
a) Annual Dose Equivalent b) Maximum Mission Duration to 150 mSv Limit

These plots are relatively symmetric, although a unit increase in field strength is slightly more effective at reducing dose equivalent than a unit increase in magnetic field thickness. Because of the symmetry, the resulting dose equivalent can be plotted for various passive/structural shielding thicknesses as a function of magnetic field bending power by assuming equal field strength and field thickness units (e.g. 4 Tm = 2T x 2m). The results can be assumed to be approximately the same for any combination of field strength and field thickness which results in the same bending power.

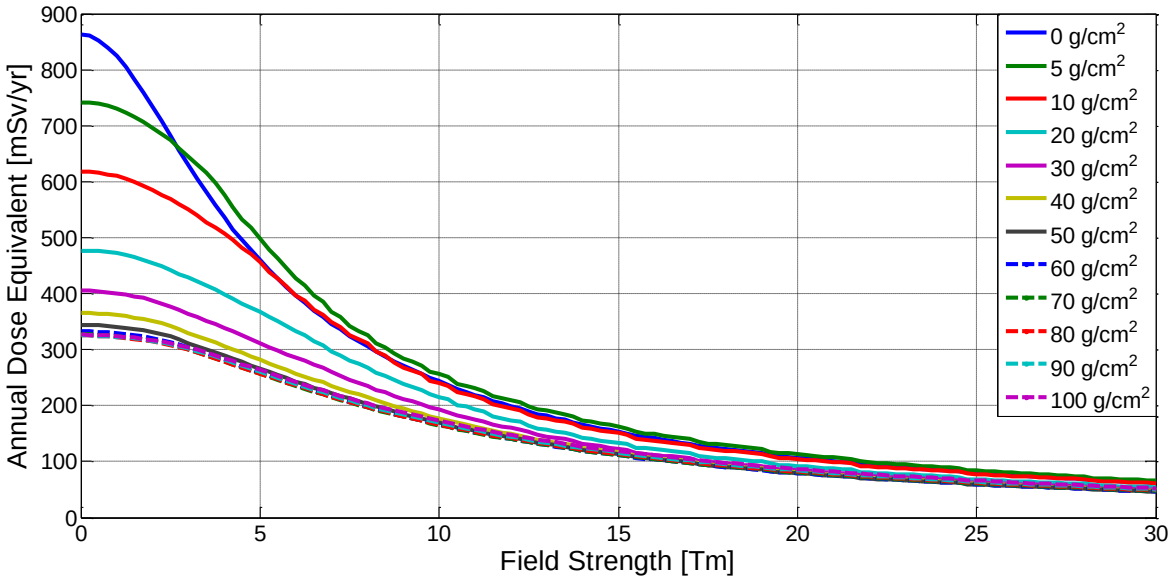

Figure 4.9 Infinite Cylinder Model, Annual Dose Equivalent vs Bending Power for Various Passive/Structural Shielding Thicknesses (r_i = 4m)

Several important concepts are shown in Figure 4.9. At high bending powers, passive/structural shielding has little impact on reducing the dose equivalent. At low bending powers, passive/structural shielding thicknesses greater than 40 g/cm^2 also have little impact on the dose equivalent. Similarly, bending powers greater than ~15 Tm appear to have a limited impact on further reducing dose equivalent values. The diminishing rate of return for high bending powers and large passive/structural shielding thicknesses indicates that, above a certain

threshold, the resulting decrease in dose equivalent may not be worth the increased cost in system mass for both active and passive components of a design.

4.2 Rapid Analysis Model: Finite, Open-Ended Cylinder

Until this point, only a theoretical solenoid magnetic field of infinite length has been discussed. While this design is not realistic, it provides useful insight into the effects of the magnetic field and serves as a limiting case for reference. An analysis of a more realistic solenoid active shield design is now presented: a cylindrical magnetic field of finite length or "open-ended cylinder" design, shown in Figure 4.10.

Unlike the infinite cylinder, where the flux coming from the end regions is reduced to zero, this active shield is open on the ends. These regions will be referred to as the "end-cap" regions. Any flux or contribution to the total dose equivalent from the end-cap regions is assumed to be unaffected by the magnetic field and subject only to passive/structural shielding. Since no magnetic field is present at the ends of the solenoid, and if no structural mass or additional passive shielding were present, a human inside this shield would be subjected to a partial view of the un-attenuated GCR spectrum entering through these openings. However, this "un-shielded" scenario is unlikely since the habitat itself will afford some passive shielding protection from the flux entering through the end-cap region. Additionally, the open space in the end-cap regions is a likely location for items such as a crew module and service module, which would provide significant amounts of additional passive shielding. The area between the two end-cap regions will be referred to as the "barrel" region. Any flux or contribution to the total dose equivalent from this region is assumed to have been attenuated by the magnetic field, as detailed previously, before passing through the passive/structural shielding mass.

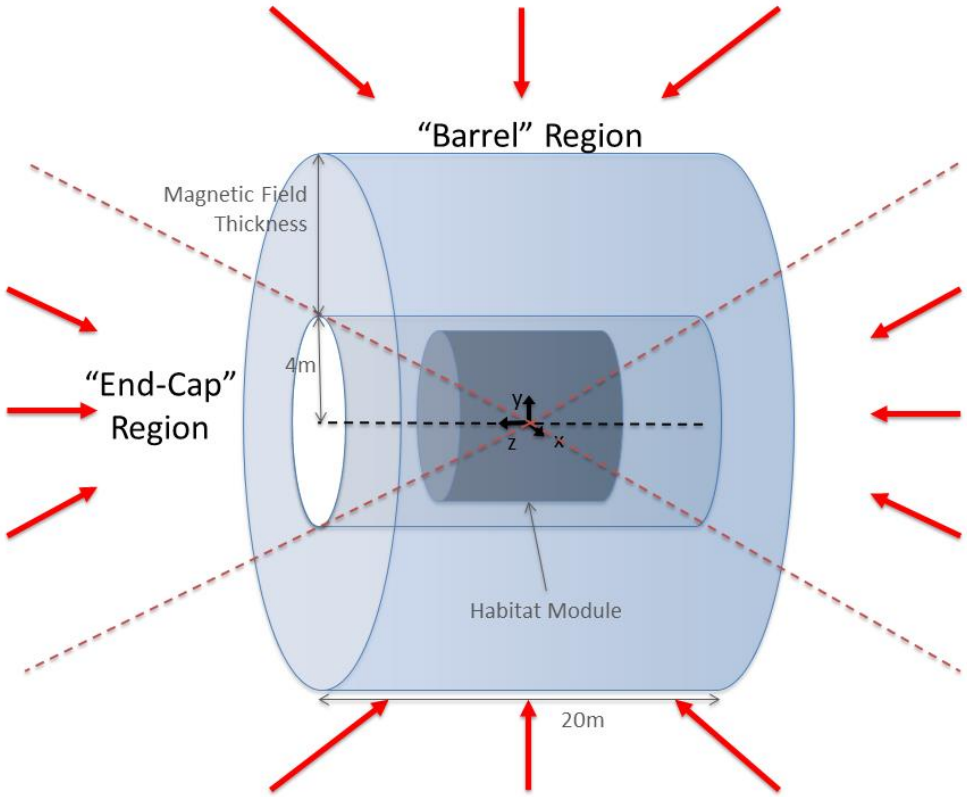

Figure 4.10 Finite, Open-Ended Cylinder Model

For the purposes of this analysis, it is assumed that the length of the active shield is 20m. This length was selected to maximize habitat shadowing and shielding efficiency. Additionally, it is also assumed that the inner radius of the magnetic field is 4m. This was selected to allow a 3m radius habitat module plus an additional meter gap to accommodate any equipment or material between it and the interior of the active shield.

4.2.1 Energy Cutoff

Similar to the case for the infinite cylinder, the cutoff energy at a point on the axial centerline varies with the approach angle, θ, as shown in Figure 4.11. Toward the center of the barrel region, where incoming particles pass through the entire thickness of the magnetic field,

the cutoff energy is governed by Eq. (4.12), the same equation as the infinite cylinder. In this region, the cutoff energy varies with the approach angle, θ, as a function of $1/\sin\theta$. In the end-cap region, the energy cutoff is obviously zero since there is no magnetic field present to attenuate the incoming particle flux. In the open-ended cylinder barrel region there also exists a "transition region," where incoming particles enter through the "side wall" of the magnetic field and do not pass through the entire thickness of the magnetic field. In this region, Eq. (4.12) still holds; however, the variable r_o, the outer radius of the magnetic field, is now equal to the radial distance from the axial centerline to the point at which the limiting energy particle penetrates the magnetic field. Therefore, the cutoff energy in this region is defined as either

$$T_{C/O,Center}(\theta) = \sqrt{\left(\left(\frac{r_o^2 - r_i^2}{2\left(\left(l/2\right) - L_P\right)\tan\theta}\right)\frac{qBc}{\sin\theta}\right)^2 + \left(m_0c^2\right)^2} - m_0c^2, \text{ for } \theta < 90^o, \qquad (4.14)$$

or

$$T_{C/O,Center}(\theta) = \sqrt{\left(\left(\frac{r_o^2 - r_i^2}{-2\left(\left(l/2\right) + L_P\right)\tan\theta}\right)\frac{qBc}{\sin\theta}\right)^2 + \left(m_0c^2\right)^2} - m_0c^2, \text{ for } \theta > 90^o, \qquad (4.15)$$

where l is the length of the solenoid magnetic field and L_P is the distance of point P from the center of the solenoid along the axial centerline.

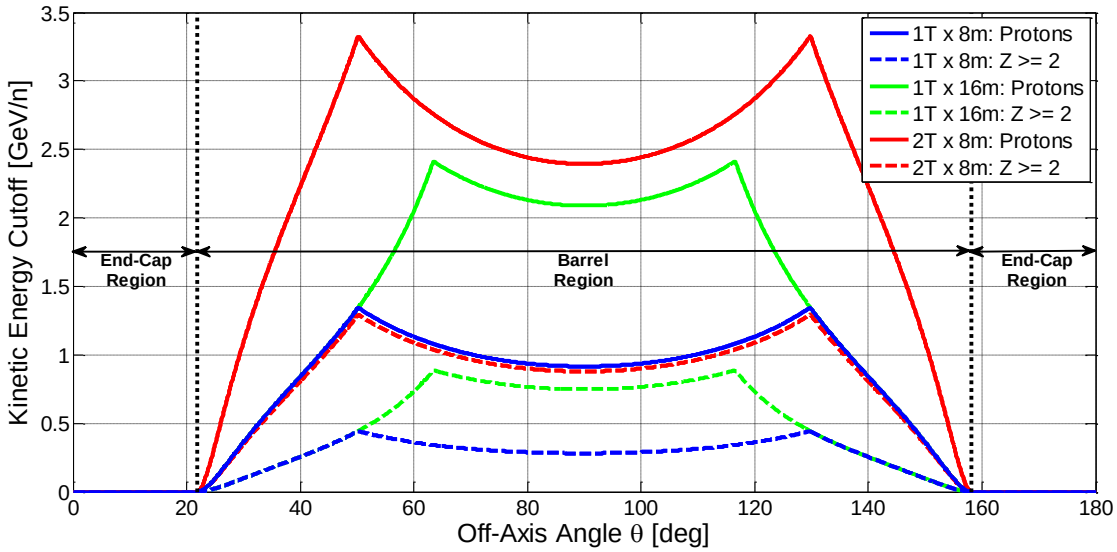

Figure 4.11 Open-Ended Cylinder Cutoff Energy at the Center of the Habitat (r_i = 4m)

4.2.2 Dose Equivalent Variation with Axial Distance from Center

In Section 4.4.2, it was demonstrated that the resulting dose equivalent inside the active shield does not significantly depend on the radial distance from the central axis of the active shield. The effect on dose equivalent as a function of distance from the absolute center of the active shield in the axial direction is now examined. In the end cap region, moving toward one end of the active shield will widen the angular view-factor on that end and narrow it on the other. Additionally, in the barrel region, moving away from the center will alter the cutoff energy profile from what is shown in Figure 4.11.

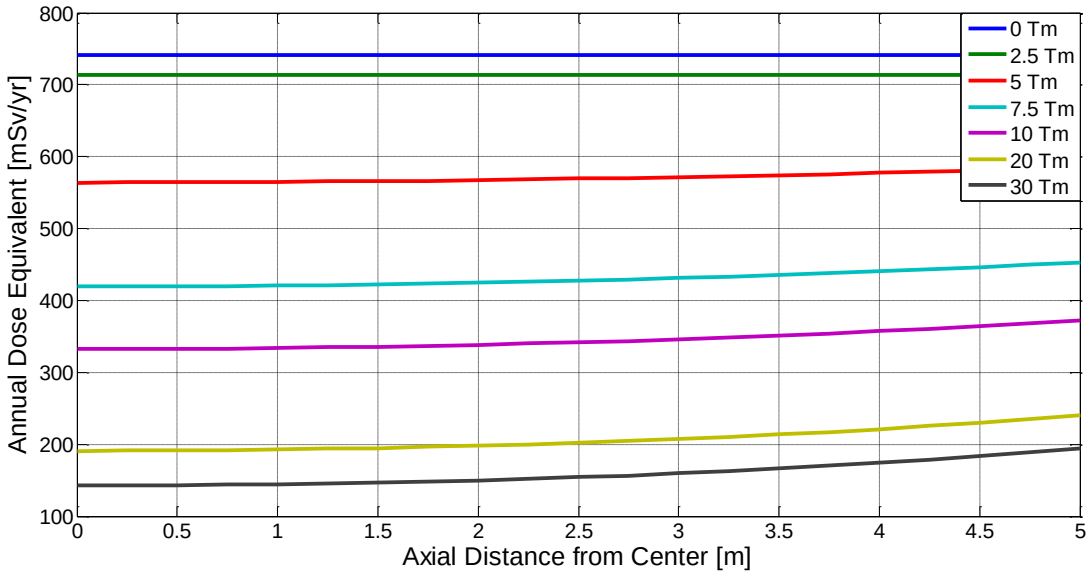

Figure 4.12 Open-Ended Cylinder Dose Equivalent vs Distance from Absolute Center (r_i = 4m, r_o = 12m)

Figure 4.12 demonstrates that as the target point P is moved away from the center of the habitat, the resulting dose equivalent increases. Therefore, in order to present the limiting case, the dose equivalent values should be evaluated at the edge of the habitat module for a given design, away from the absolute center of the active shield.

4.2.3 Trade Space Analysis

Figures 4.13 - 4.15 show the annual dose equivalent and maximum mission duration for a range of magnetic field strengths and field thicknesses. The results shown are for 5.0, 10.0, and 20.0 g/cm^2 of passive/structural aluminum shielding. The figures show the dose equivalent value at the worst-case location for the open-ended cylinder model (i.e. at the edge of the habitat), which is assumed to be 5m from the absolute center, along the axial centerline, for the results shown.

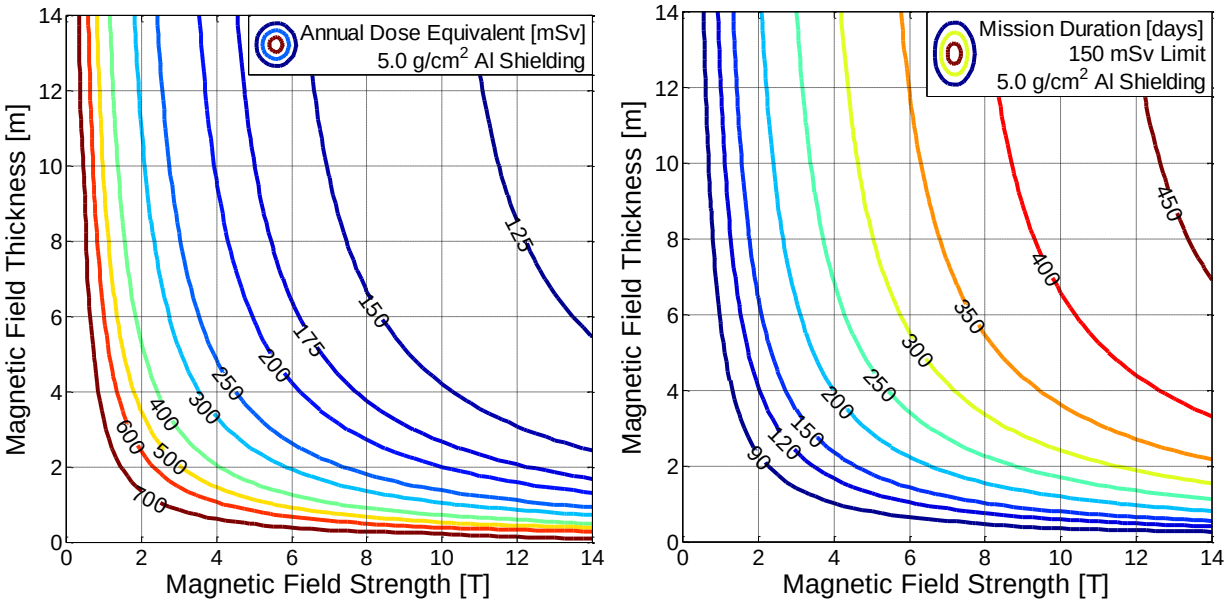

Figure 4.13 Open-Ended Cylinder Model, 5.0 g/cm^2 Passive/Structural Al Shielding (r_i = 4m)
a) Annual Dose Equivalent, b) Maximum Mission Duration to 150 mSv Limit

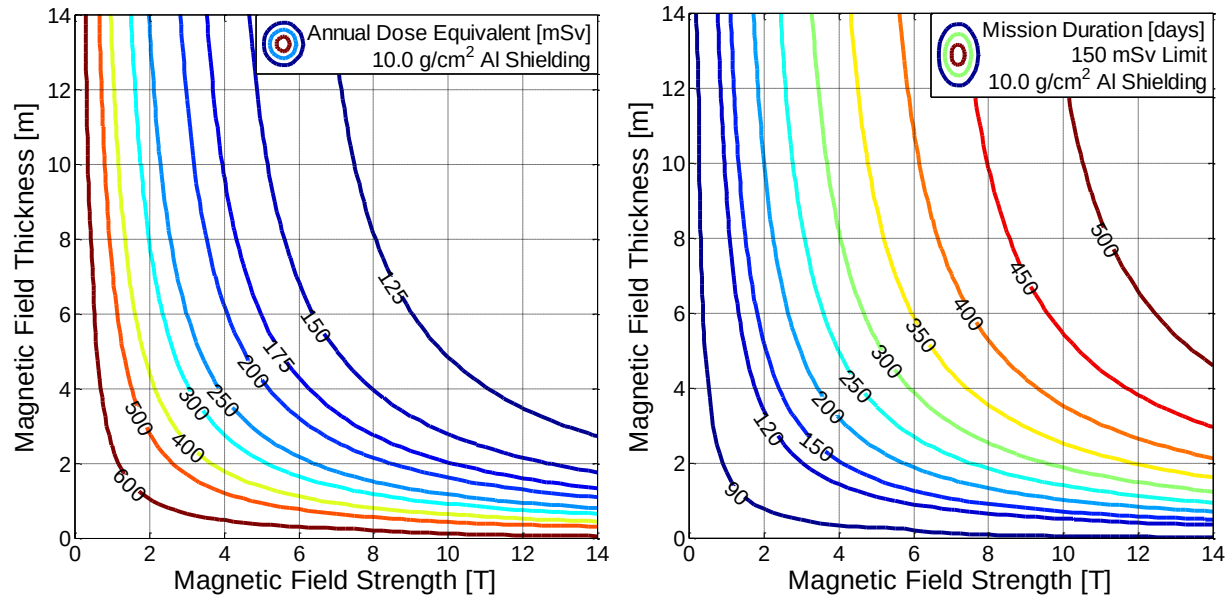

Figure 4.14 Open-Ended Cylinder Model, 10.0 g/cm^2 Passive/Structural Al Shielding (r_i = 4m)
a) Annual Dose Equivalent, b) Maximum Mission Duration to 150 mSv Limit

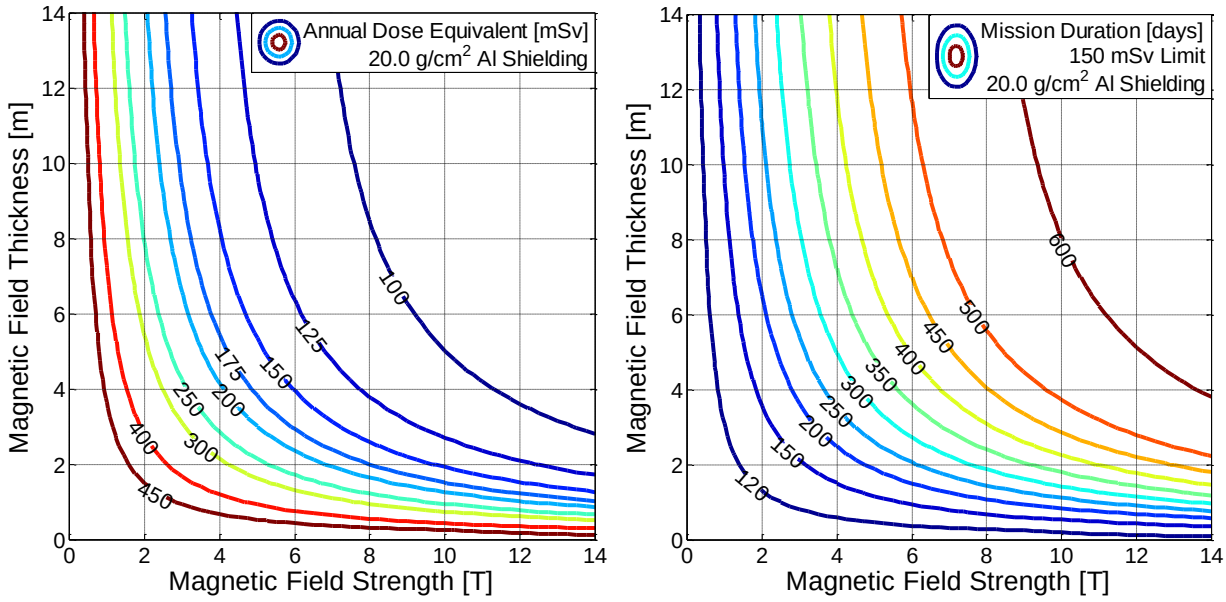

Figure 4.15 Open-Ended Cylinder Model, 20.0 g/cm^2 Passive/Structural Al Shielding (r_i = 4m)
a) Annual Dose Equivalent, b) Maximum Mission Duration to 150 mSv Limit

These plots are much less symmetric than was seen for the infinite cylinder case, and for a given bending power, a higher field strength is more effective at reducing dose equivalent than a larger field thickness (e.g. 10T x 2m yields ~150 mSv/yr, 2T x 10m yields ~225 mSv/yr). However, it is still useful to observe how the resulting dose equivalent is affected by bending power by assuming equal field strength and field thickness units (e.g. 4 Tm = 2T x 2m), as shown in Figure 4.16.

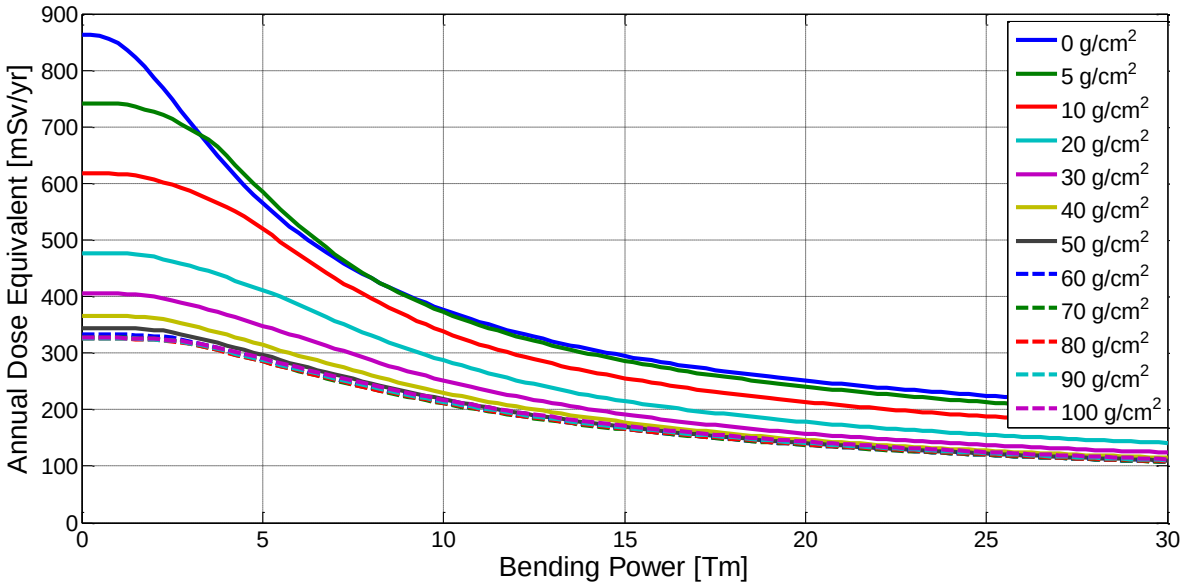

Figure 4.16 Open-Ended Cylinder Model, Annual Dose Equivalent vs Bending Power for Various Aluminum Passive/Structural Shielding Thicknesses (r_i = 4m)

The results shown in Figure 4.16 for the open-ended cylinder model are very similar to those shown in Figure 4.9 for the infinite cylinder model. Bending powers greater than ~15 Tm and passive/structural shielding thicknesses greater than 40 g/cm^2 appear to have a limited impact on further reducing dose equivalent values. However, unlike the infinite cylinder case, passive/structural shielding thickness has a definite impact, even at high bending powers. This is due to the GCR flux entering through the end-cap regions of the open-ended cylinder, where passive/structural shielding provides the only protection.

As stated previously, the open-ended cylinder model results are not symmetric, and an increase in field strength will have a greater impact than an increase in field thickness. This is demonstrated in Figure 4.17 where the range of achievable dose equivalent values is shown for a given bending power by fixing either the field strength at 1T, or the field thickness at 1m, and then varying the other component. Thus, it can be seen that for a given bending power, a higher magnetic field component is more desirable in terms of reducing the dose equivalent.

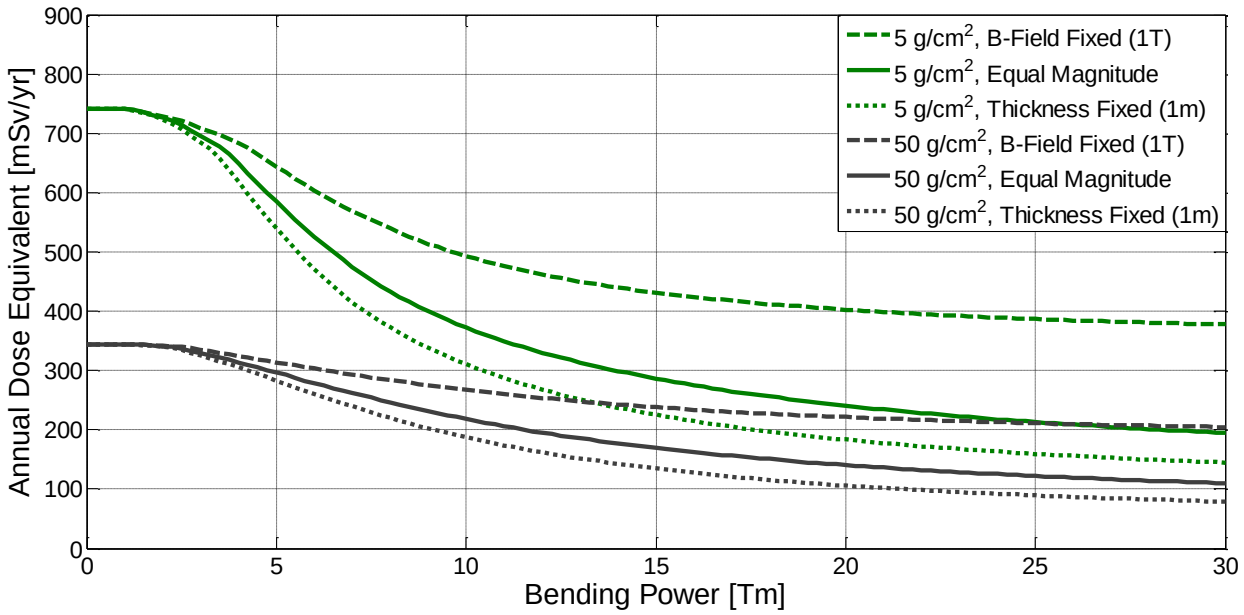

Figure 4.17 Open-Ended Cylinder Model, Field Strength and Field Thickness Effects (r_i = 4m)

4.3 Chapter Summary

The simplicity of the electromagnetic analytic solution model combined with the computational speed of HZETRN allows the rapid determination of dose equivalent values over a large trade space of variables. By providing an analysis over a large variables such as magnetic field strength, magnetic field thickness, and passive/structural shielding mass, the above results allow designers to select configurations suited to specific mission goals, including mission radiation exposure limits, duration, and destination. In order to reduce the required computation time, four primary assumptions are made in this model: the magnetic field is uniform in magnitude, the magnetic field is confined to the boundaries of a cylindrical geometry, all of the mass is confined in the interior of the magnetic field, and this mass is represented by an appropriate volume of spherical shielding. Future work concerning this model should focus on quantifying the effects of these assumptions.

Based on the generated results, several characteristics of an active solenoid magnetic shield design can be determined. Bending powers greater than ~15 Tm and passive/structural shielding thicknesses greater than 40 g/cm^2 have a limited impact on further reducing dose equivalent values. Passive/structural shielding has a greater impact at lower bending powers; however, it still has a definite impact even at high bending powers due to the shielding it provides in the end-cap regions where the magnetic field does not attenuate the incoming GCR flux. Additionally, for a given active shield bending power, magnetic field strength is slightly more effective at reducing dose equivalent than field thickness. This leads to the conclusion that, all else being equal, a higher magnetic field strength is more desirable than a higher field thickness in terms of reducing dose equivalent. However, the trade space results presented in this chapter are based upon uniform quantities of aluminum shielding which do no vary as a function of the active shielding parameters. In the following chapter a survey of active shielding systems is conducted so that the actual mass values may be adjusted as a function of the trade space variables

Chapter 5

System Survey Mass and Material Estimates

The rapid analysis model developed in the previous chapter enables the analysis of a large array of active shielding design variables. However, the trade study results presented in Chapter 4 only utilize various uniform distributions of aluminum shielding to represent the total passive/structural shielding mass of the system. As previously discussed, there is a complex relationship between the size and strength of the magnetic field and the amount and type of mass required to create it. Even modest changes in active shielding design parameters can have significant impacts on the system mass requirements and radiation exposure results. In addition to the quantity of mass, the material composition can significantly affect the resulting flux inside the shield and the resulting radiation exposure values. Therefore, in order to provide a more robust model, mass and material estimates are developed.

In this chapter, the major systems required for a solenoidal, active magnetic shield are explored: magnetic/superconductor, structure, thermal, and power systems. These systems are studied because they are highly interdependent and potential mass drivers of the overall system design. A detailed survey is conducted for each one and a trade study of some of the major design options is presented, which allows a narrowing in scope of possible system solutions. From this, mass and material estimates are formulated as a function of the primary design parameters under consideration: magnetic field strength and field thickness. These estimates can be incorporated into the rapid analysis model so that as design variables change, so does the

mass of each system, which contributes to the overall shielding of the design. This systems analysis also allows the identification of several key technologies for the development of an active magnetic shield. These technologies are either enabling for such a design or would provide significant mass or performance improvements.

5.1 General Configuration

There are several ways in which a solenoid magnetic field design may be constructed, as shown in Figure 5.1. The coils in each of these designs are wound such that the magnetic field runs parallel to the central axis of the interior volume. The first configuration on the left uses irregular coils with a pie shaped cross section to create the solenoid magnetic field. While this configuration allows minimal gaps between the coils, the irregular shape makes the necessary systems difficult to analyze. In the last configuration, on the right side of Figure 5.1, a single ring of cylindrically shaped solenoid coils is used to create the magnetic field. This design greatly simplifies the following systems analysis, particularly for the superconductor and structural systems. This permits the analysis of a single cylindrical coil, where the diameter of the solenoid coil is equal to the magnetic field thickness analyzed. Therefore, this last configuration, using a single layer of cylindrically shaped solenoid coils, is utilized for the systems analysis in the following sections.

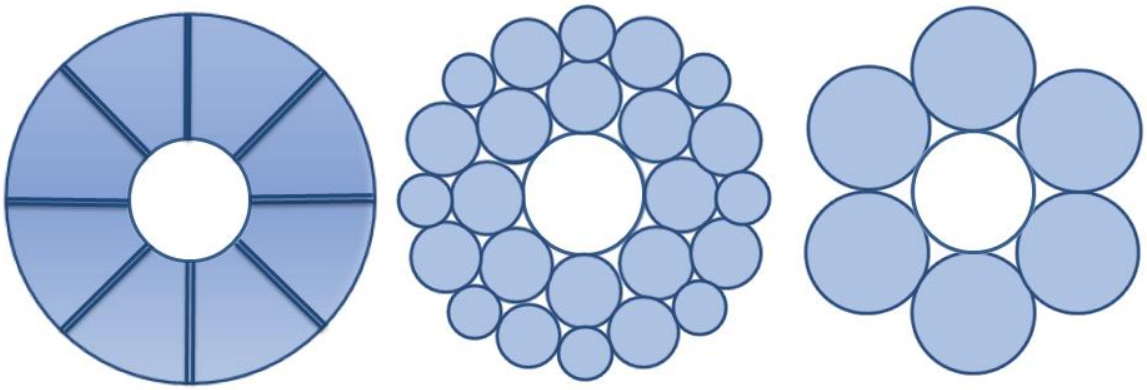

Figure 5.1 End View of Various Solenoid Field Configuration Options

5.2 Magnetic/Superconductor System

There are three primary methods for creating a magnetic field which could be used for radiation protection: permanent magnets, standard electromagnetic coils, and superconducting electromagnetic coils. Large field strengths have been achieved with permanent magnets; however, these are generally only on a small scale (Kumada et al., 2001). As shown in the previous chapter, the ability of a shield to deflect incident radiation is also related to the field's thickness. Therefore, on the scale desired for shielding a spacecraft, large volumes of magnetic fields are required. Filing these volumes with large permanent magnets would require significant quantities of mass and generating these field volumes can be accomplished with less mass through the use of hollow bore electromagnetic coils. Standard electromagnetic coils are capable of achieving the large field strengths and geometries desired, but the high resistivity of conventional conductor materials makes them undesirable for active shielding applications. The high resistance losses would require a large thermal system to dissipate the resulting thermal energy and a large power system to compensate for these losses. However, superconducting magnetic coils have the capability of generating extremely powerful magnetic fields with a mass that allows for feasible active shielding designs. Superconducting materials possess the unique

property that they exhibit no, or negligible, electrical resistivity below a certain critical temperature, T_C. Therefore, these materials enable the construction of powerful magnetic fields that are not constrained by the high power requirements and resistance losses associated with standard electromagnets.

5.2.1 Superconductors: Low Temperature vs. High Temperature Superconductors

The topic of superconduction and its theory is a lengthy one and only a brief discussion is given here. Further descriptions may be found in Cyrot and Pavuna (1992) and Iwasa (2009). Superconducting materials possess the unique property of superconductivity, where they exhibit no, or negligible, electrical resistivity below the material's critical temperature, T_C, defined as the transition temperature between superconducting and non-superconducting states. This superconducting property disappears if an external field is applied to the material that is greater than the critical magnetic field, H_C. H_C is defined as the maximum external field that can be applied, as a function of temperature, for a material to remain superconductive. Additionally, this superconducting state can be destroyed by passing a current through the material that exceeds the critical current density, J_C. At the critical current, a magnetic field is created at the surface of the superconductor which is equal to the critical field, H_C, resulting in a loss of superconductivity. Therefore, T_C, H_C, and J_C define a critical surface below which the superconducting phase can exist. While T_C and H_C are thermodynamic properties of the material, J_C is not, and can be significantly altered by metallurgical processing.

Superconductor materials are classified as either Type I or Type II. Type I materials exhibit superconductivity up until the critical magnetic field, H_C, at which point the material becomes completely non-superconducting. H_C values for Type I superconductors are usually

very low; therefore, they are not suitable for use in magnetic applications. Type II materials have two critical magnetic field values: a lower critical field, H_{C1}, and an upper critical field, H_{C2}. Below the lower critical field, H_{C1}, Type II materials are fully superconducting and behave like Type I materials. Between H_{C1} and H_{C2}, Type II materials exhibit properties of a "mixed state," between superconducting and non-superconducting, until they reach the upper critical field, H_{C2}, where they become completely non-superconducting. H_C values are much higher for Type II superconductors, making them more suitable for magnetic applications.

Superconducting materials are further classified in two general categories: Low Temperature Superconductors (LTS), with a T_C less than ~40K, and High Temperature Superconductor (HTS), with T_C values of up to ~100K. LTS magnets are typically operated in the range of 4.2K, the boiling point of liquid helium, while HTSs allow higher operating temperatures; however, both LTSs and HTS have additional advantages and disadvantages (Iwasa, 2009). Another consideration, when comparing LTSs and HTSs for active shielding applications, is the risk of "quench." Quench is the phenomenon that can occur when any part of the superconductor material departs from its superconductive state during operation. This change in material properties causes a localized increase in resistance and a sudden increase in resistance losses, creating a "hot spot." The entire stored energy of the magnet may be dissipated over this hot spot resulting in permanent damage.

As will be illustrated later for the thermal system, the overall requirements of a LTS magnet are prohibitive for use in a large scale, space based platform. HTS magnets allow a higher operating temperature and also allow for a greater thermal margin to be applied, reducing the risk of quench. Therefore, the subsequent focus will remain on HTS materials. Figure 5.2

shows a trade tree highlighting the major design options for the magnetic/superconductor system and the down-selection to a HTS design.

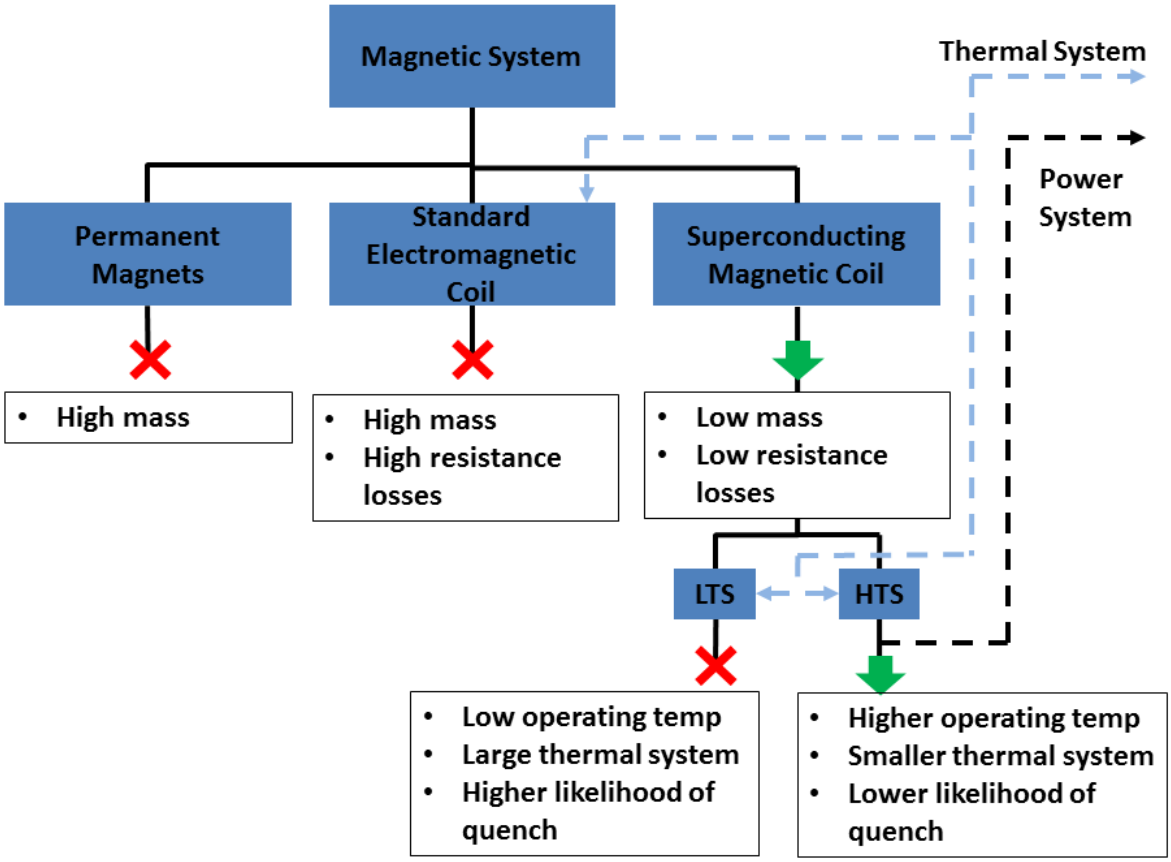

Figure 5.2 Magnetic/Superconductor System Trade Tree

5.2.2 Mass and Material Estimates

Since a HTS based superconducting electromagnetic coil design has been highlighted as the primary architecture option, mass and material estimates for this system can be conducted. Of the HTS material choices, the most prominent are known as REBCO and BSCCO. REBCO stands for the generic Rare Earth Barium Copper Oxide, or rare earth barium cuprate, where the rare earth element is usually Yttrium (Y), Europium (Eu), Erbium (Er), or Gadolinium (Gd). These are of the generic formula $REBa_2Cu_3O_{7-x}$, where x is the relative oxygen doping of a

given compound, with the most popular being YBCO (Saxena, 2012). BSCCO stands for Bismuth Strontium Calcium Copper Oxide, of the generic formula $Bi_2Sr_2Ca_{n-1}Cu_nO_{2n+4}$. The most popular of the BSCCO HTSs are Bi-2212, the n=2 compound ($Bi_2Sr_2CaCu_2O_{8+x}$), and Bi-2223, the n=3 compound ($Bi_2Sr_2Ca_2Cu_3O_{10+x}$) (Saxena, 2012). The above materials are commonly available in a wire or tape form where the superconductor itself is layered or imbedded within a stabilizer material, usually copper, aluminum, or silver (Figure 5.3). In the case of tape type conductors, an additional substrate material is used (Figure 5.4).

Figure 5.3 Example BSSCO Multifilament Round Wire in Ag Stabilizer
(Graphic provided courtesy of Oxford Instruments)

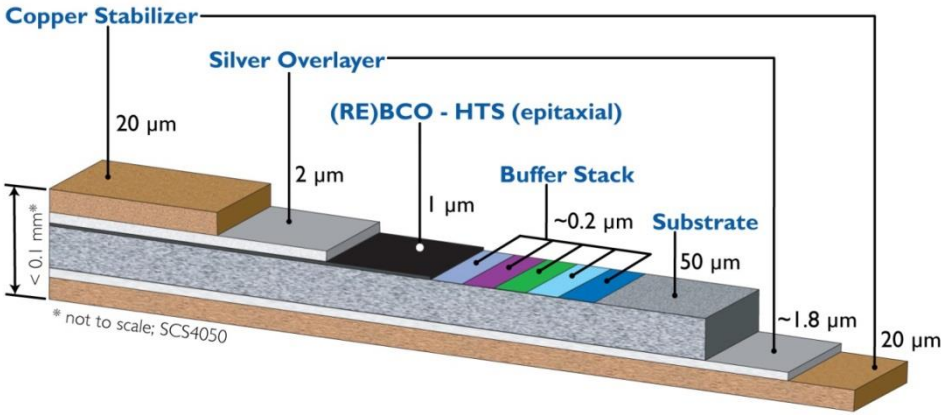

Figure 5.4 Example YBCO Tape (Graphic provided courtesy of SuperPower Inc.)

These YBCO and BSSCO tapes and wires can be used for mass composition estimates. The mass can be estimated based upon the current carrying capabilities of these tapes/wires and the electric current required for a given magnetic field strength. The total mass will not only be a function of the electric current required to generate the field, but also the dimensions of the desired field, i.e. the magnetic field thickness.

5.2.2.1 Tape/Wire Electric Current Requirements

The field strength at the center (radial and axial), $B(0,0)$, of an ideal, thin walled magnetic solenoid coil is

$$B(0,0) = \frac{\mu_0 N i}{\sqrt{D^2 + l^2}}, \tag{5.1}$$

where i is the current, N is the total number of windings, μ_0 is the permeability constant, D is the solenoid diameter, and l is the solenoid length (Iwasa, 2009). By assuming that this field is uniform throughout the solenoid, and equal to the desired magnetic field strength, B, Eq. (5.1) can be rewritten to give current as a function of magnetic field strength and thickness,

$$i(B,D) = \frac{B\sqrt{D^2 + l^2}}{\mu_0 N}. \tag{5.2}$$

Since N is equal to the solenoid length, l, divided by the width of the solenoid windings (wire/tape width plus space between windings), w_t, Eq. (5.2) can also be written as

$$i(B,D) = \frac{B\sqrt{D^2 + l^2}}{\mu_0 l} w_t. \tag{5.3}$$

Using Eq. (5.3), one can show that extremely high currents will be required, even for low magnetic field strengths and field thicknesses. For example, a 1T, 1m diameter, 20m long solenoid, constructed of a single layer of 1cm width tape, will require 7.9 kA of current.

5.2.2.2 Tape/Wire Electric Current Capabilities

Essential to the design of the superconductor coil is the engineering current density, J_e, of the superconductor. This is the maximum current that the tape or wire can carry divided by its entire cross section. This is directly related to the critical current density, J_C, of the superconductor but accounts for the overall design of the wire by including non-current carrying mass. Current HTS tapes and wires utilize either a substrate and stabilizer or stabilizer only designs. These are essential for the stability, robustness, and manufacture of these tapes and wires; however, they increase the overall mass of the system and reduce the engineering current density. Any improvements in superconductor manufacturing which increase the critical current density, J_C, as well as any manufacturing improvements which increase the superconductor/non-superconductor ratio, will directly impact J_e (Schwartz, 2008).

Both J_e and J_C values are often given at a reference state of 77K, self-field (i.e. no externally applied field). State-of-the-art superconductor YBCO tape technologies have engineering current densities in the range of ~21-29 kA/cm^2 at 77K and self-field (SuperPower Inc. website). State-of-the-art superconductor BSCCO wire technologies have slightly higher current capabilities. J_C, and therefore J_e, are a function of both temperature and magnetic field (Lombardo et al, 2011), which have competing effects. As temperature decreases, the critical current increases, and as the magnetic field increases, the critical current decreases. Additionally, the critical current is affected not only by the magnitude of the magnetic field, but also by its direction (Haugan et al., 2009). Since these current capability values are a function of temperature, magnetic field magnitude, and magnetic field direction, the maximum current capability will be dependent on the selected system operating temperature and overall system design.

If the required current for a coil design exceeds the maximum current available, multiple layers of tape or wire can be used. This type of layering could be achieved in a manner similar to pancake coils, commonly used in large commercial magnetic coils. Alternatively, these tape layers could be bundled together using techniques such as Roebel cables (Turenne, 2010) or other wound techniques (van der Laan et al., 2011). For example, if 1cm width YBCO tape is capable of carrying a maximum of 250 A at the selected operating temperature and design, then for a 1T, 1m diameter, 20m long solenoid, 32 layers of this tape would be required to achieve the desired field strength.

5.2.2.3 Superconductor Solenoid Coil Mass

The current density, J, is the operating current divided by the cross sectional area of the entire tape or wire, A_t. This value accounts for the area of the tape/wire's non-superconducting material as well. Therefore,

$$J(B,D) = \frac{i}{A_t} = \frac{B\sqrt{D^2 + l^2}}{\mu_0 N A_t}. \tag{5.4}$$

The minimum number of layers of tape or wire required to achieve a given field, without exceeding the electric current capacity of the material, n_{layers}, can be determined by dividing by the engineering current density of the material,

$$n_{layers}(B,D) = \frac{J}{J_e} = \frac{B\sqrt{D^2 + l^2}}{\mu_0 N A_t J_e}. \tag{5.5}$$

The total superconductor volume can then be determined by

$$V_{SC}(B,D) = n_{layers} A_t \pi D N = \frac{B\pi D\sqrt{D^2 + l^2}}{\mu_0 J_e}. \tag{5.6}$$

And thus the total superconductor mass per coil, m_{sc}, is

$$m_{sc}(B,D) = \frac{\rho_{sc} B \pi D \sqrt{D^2 + l^2}}{\mu_0 J_e}, \tag{5.7}$$

where ρ_{sc} is the density of the superconductor material.

5.2.3 Wire/Tape Lengths and Splicing

An important aspect of superconductor wire and tape technology is the maximum manufacturing length. "This is not an intrinsic engineering problem but rather a question of commercial scale-up requiring sufficient market pull" (Schwartz, 2008). Also of importance is the technology available for splicing these lengths of tape or wire together. Combined, these technologies play a significant role in the thermal system due to resistive losses at splice junctions. A 1m diameter, 20m long coil made of a single layer of 1cm wide tape would require ~6.3 km of tape. Therefore, for even small coil dimensions, extremely large lengths of tape are required, and any improvements in superconductor length would reduce the number of splices required. Splices are of concern because perfectly superconducting splice technology does not currently exist. State-of-the-art splices can achieve resistance values of approximately 20 nΩ (SuperPower Inc.). While this may seem small, the large current values required can result in large resistance losses. This makes any splice a heat source, which must be accounted for as part of the thermal system. Additionally, the power loss from these splices must be compensated for by the power system to maintain the required operating current.

5.2.4 Superconductor System Key Technologies

Based on this survey of the superconductor system, the following key technologies are identified for the development of an active magnetic shield:

1. Metallurgical and manufacturing improvements to increase the critical current density of existing superconductor material. This would reduce the amount of superconductor mass required to achieve a given field configuration and reduce system complexity.
2. Metallurgical and manufacturing improvements to increase the engineering current density of existing superconductor materials. Again, this would reduce the amount of superconductor mass required to achieve a given field configuration and reduce system complexity.
3. Manufacturing improvements to increase the maximum achievable length of superconductor wires and tapes. This would reduce the number of splices required for a given design, reducing the heat removal requirements on the thermal system.
4. Development of improved superconductor splice technology. This would reduce the heat load from superconductor splices, reducing the heat removal requirements on the thermal system, as well as the requirements of the power system which must compensate for these losses.
5. Development of new, higher temperature superconductors. This would allow higher operating temperatures and potentially relax thermal design requirements.

It is important to note that the first four key technologies focus on improving existing superconductors and only the last focuses on the development of new materials. While there are approximately 10,000 known superconducting materials and compounds, there are on the order of 10 such materials which are suitable for magnetic applications (Iwasa, 2009). As described by Iwasa (2009), the process of developing these new materials is both long and costly. Therefore, technology development can be divided into near term goals, improving existing

superconductors, or long term goals, developing new superconductors, and prioritized based upon development objectives and constraints.

5.3 Structural System

The magnetic forces within a cylindrical solenoid coil can be divided into two categories: radial and axial. As a result of the Lorentz force, the interaction between the current in a solenoid and the magnetic field it creates produces in an outward radial force, often called the "magnetic pressure." The Lorentz force also results in an axially directed, compressive force. Without adequate structural support, the superconducting elements of a design would expand outward and compress together like a spring. In addition to the forces within a coil, there are also coil-to-coil forces. These arise from the interaction of each coil with the external magnetic field resulting from the surrounding coils, much in the same way that two dipole magnets will repel one another when placed side by side with their poles aligned.

The radial and axial forces within a cylindrical coil may be compensated for separately. Since the axial force is compressive, a rigid material is required to keep the coil from collapsing. However, the radial force is an outward directed, tensile force. This allows the option that instead of the coil structure being composed entirely of a single material, such as an aluminum walled cylinder, it may be partially constructed using other high-strength, light-weight materials for radial support. Such a design would allow the cylinder to be constrained radially and separate axial beams, running the length of the cylinder, could be incorporated to prevent compression. This will be termed the "mixed-material" option and this configuration can provide substantial mass savings over designs which use a single material, as will be detailed later. High-strength, light-weight options include composites or fiber materials such as Kevlar or Zylon. Using

flexible material for radial support, i.e. not impregnated with epoxy or resin, could also be used to create a "semi-rigid" design. Such a design could allow movement of the coils in the radial direction when they are not in use. Therefore, the structure could potentially be collapsed, allowing it to be housed in a smaller launch vehicle fairing, as proposed by Westover et al. (2012). Because of the substantial mass savings offered, the rigid or semi-rigid mixed-material design options have been down-selected as the most likely structural configurations.

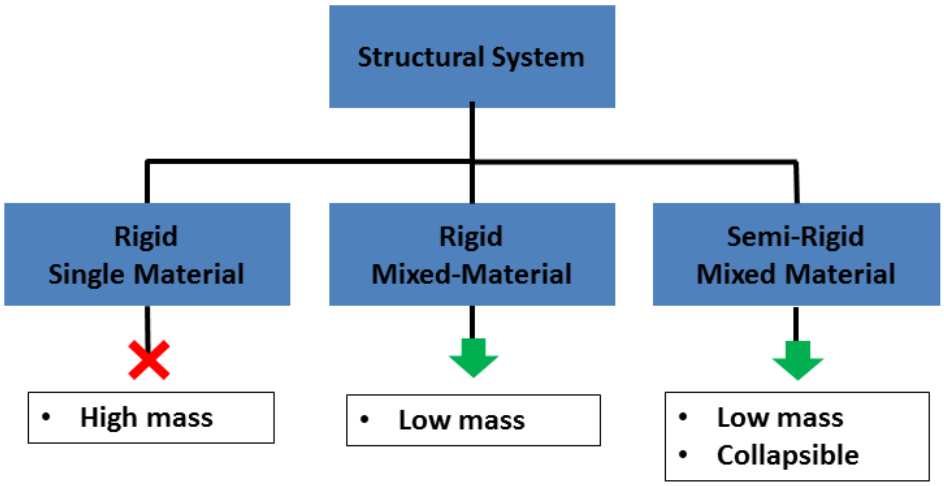

Figure 5.5 Structure System Trade Tree

The forces that the support structure must compensate for will be determined using a "thin-walled", "long" cylinder approximation of an individual solenoid coil. The "thin-walled" approximation is appropriate for all cases being examined, since the thickness of the cylinder wall will be much less than the cylinder's radius. The "long" approximation assumes that the cylinder's length is much greater than its diameter. This is not the case for some of the large diameter coils being analyzed; however, this error was calculated over the trade space analyzed and determined to be minimal.

5.3.1 Radial Forces and Structural Support Mass

The magnetic pressure, p_m, or radially directed outward pressure on a coil, for an ideal, thin-walled, long cylindrical coil is

$$p_{\mathrm{m}} = \frac{B^2}{2\mu_0}, \tag{5.8}$$

(Iwasa, 2009). Pressure in a cylinder can be translated into hoop stress, σ_t, which is the stress in the azimuthal (tangential) direction in the cylinder wall. For a thin-walled, long cylinder, the magnetic pressure is related to σ_t by

$$\sigma_{\mathrm{t}} = \frac{p_m D}{2t_{\mathrm{w}}}, \tag{5.9}$$

where t_w is the coil wall thickness. Substituting Eq. (5.8) into Eq. (5.9) yields the hoop stress as a function of magnetic field thickness and strength,

$$\sigma_{\mathrm{t}}(B, D) = \frac{B^2 D}{4\mu_0 t_{\mathrm{w}}}. \tag{5.10}$$

The maximum tensile strength that a material can withstand without failure is defined as the ultimate tensile strength, σ_u. The maximum stress in a part is limited relative to its strength by a Factor of Safety, F_S, which accounts for uncertainties in the loads, analysis methods, and material strength. Therefore, the maximum allowed hoop stress, $\sigma_{t\text{-}max}$, is given by

$$\sigma_{\mathrm{t-max}} = \frac{\sigma_{\mathrm{u}}}{F_S}. \tag{5.11}$$

Setting Eq. (5.10) equal to the maximum allowed tensile strength in Eq. (5.11) results in an equation for the required structural wall thickness as a function of magnetic field thickness and strength,

$$t_w(B,D) = \frac{B^2 D F_S}{4\mu_0 \sigma_u}. \tag{5.12}$$

The coil radial structural volume can then be determined by

$$V_{struct-radial}(B,D) = t_w \pi D l = \frac{B^2 D^2 \pi l F_S}{4\mu_0 \sigma_{u\text{-radial}}}, \tag{5.13}$$

where $\sigma_{u\text{-}radial}$ is the ultimate tensile strength of the radial structural support material. Therefore, the radial structural mass required per coil, $m_{struct\text{-}radial}$, is

$$m_{struct-radial}(B,D) = \frac{\rho_{struct-radial} B^2 D^2 \pi l F_S}{4\mu_0 \sigma_{u\text{-radial}}}, \tag{5.14}$$

where $\rho_{struct\text{-}radial}$ is the density of the radial structural material.

High-strength, light-weight materials such Kevlar or Zylon have a strength to mass ratio that is several times larger than aluminum. Therefore, the mass savings provided by these materials can be substantial. For example, a 1T, 1m diameter, 20m long solenoid coil would require 152.0 kg of aluminum for radial support. Similarly, a coil using Kevlar would only require 7.0 kg per coil, a 95% mass savings over aluminum, and a coil using Zylon would require 1.2 kg per coil, a mass savings of ~99% over aluminum. While these values seem reasonable, they are for a low field strength, low field thickness example. Eq. (5.14) shows that the required radial support mass varies as a function of B^2 and D^2; therefore, the required mass can become substantial at higher strengths and thicknesses. Figure 5.6 shows the radial support mass requirements over the design trade space using Kevlar49 as the radial support material with a F_S of 1.4.

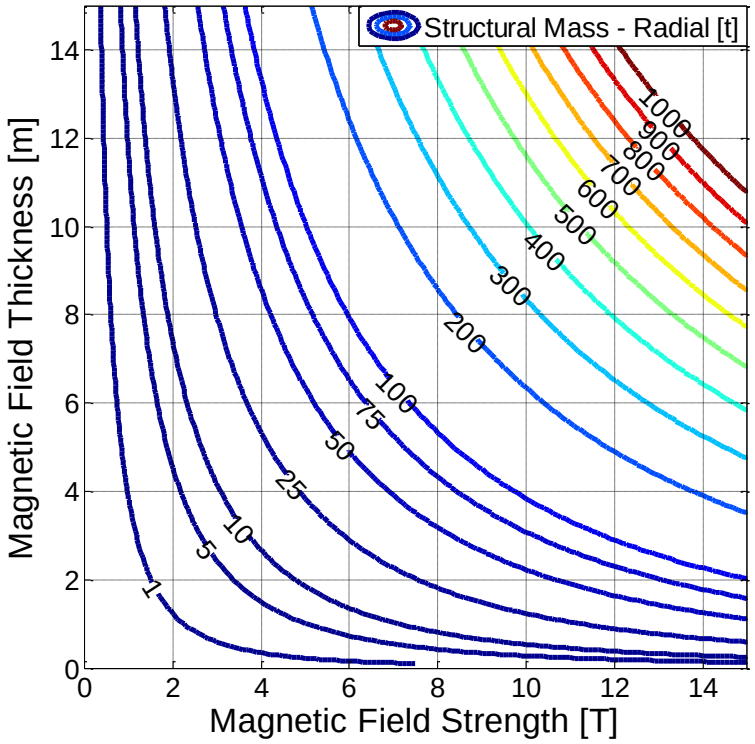

Figure 5.6 Radial Support Structure Mass, Kelvar49
(F_S = 1.4, $\sigma_{u\text{-}axial}$ = 1.44 g/cm^3, $\rho_{struct\text{-}axial}$ = 3.6 GPa)

5.3.2 Axial Forces and Structural Support Mass

The Lorenz forces in the coil also work to compress the coil axially. This force is greatest at the axial mid-plane of the coil, and reduces to zero at the ends of the coil (Iwasa, 2009). The equation for the maximum force at the mid-plane (axial center) for an ideal, thin-walled, long cylindrical coil is

$$F_z(0) = -\frac{\mu_0}{2}\left(\frac{Ni}{l}\right)^2 \pi\left(\frac{D}{2}\right)^2. \tag{5.15}$$

Note that the negative sign indicates the force is compressive. Eq. (5.2) can be rewritten to match the thin-walled, long cylinder approximation where $D << l$. This equation can then be rearranged so that

$$\frac{Ni}{l} = \frac{B}{\mu_0}. \tag{5.16}$$

Substituting Eq. (5.16) into Eq. (5.15) yields

$$F_z(0) = -\frac{B^2 D^2 \pi}{8\mu_0}. \tag{5.17}$$

Note that Eq. (5.17) is also equal to the magnetic pressure multiplied by the cross sectional area of the coil,

$$F_z(0) = -p_m \pi \left(\frac{D}{2}\right)^2. \tag{5.18}$$

Since the axial force is highest at the center and reduces to zero at the edges, the axial support structure can be sized appropriately to save mass. Therefore, the following axial support structure analysis is based on the average axial force, $F_{z\text{-}avg}$, equal to ½ of the maximum axial force, $F_z(0)$,

$$F_{z-\text{avg}}(B,D) = \frac{F_z(0)}{2} = -\frac{B^2 D^2 \pi}{16\mu_0}. \tag{5.19}$$

The maximum allowed axial stress, $\sigma_{a\text{-}max}$, is related to the ultimate tensile strength, σ_u, of the structural material by a safety factor, F_S,

$$\sigma_{a-\max} = \frac{\sigma_u}{F_S}. \tag{5.20}$$

The average cross sectional area required for the axial support structure, A_{axial}, is related to the average axial force by

$$A_{\text{axial}} = \frac{F_{z-\text{avg}}}{\sigma_{a-\max}}. \tag{5.21}$$

Substituting Eqs. (5.19) and (5.20) into Eq. (5.21) yields

$$A_{\text{axial}}(B,D) = \frac{\mathrm{B}^2\mathrm{D}^2\pi F_S}{16\mu_0\sigma_{\text{u-axial}}}. \tag{5.22}$$

where $\sigma_{u\text{-}axial}$ is the ultimate tensile strength of the axial structural support material. The coil axial structural support volume required, $V_{struct\text{-}axial}$, is then given by

$$V_{struct-axial}(B,D) = A_{\text{axial}}l = \frac{\mathrm{B}^2\mathrm{D}^2\pi l F_S}{16\mu_0\sigma_{\text{u-axial}}}. \tag{5.23}$$

Therefore, the axial structural support mass required per coil, $m_{\text{struct-axial}}$, is

$$m_{struct-axial}\left(\mathrm{B},\mathrm{D}\right) = \frac{\rho_{struct-axial}B^2D^2\pi l F_S}{16\mu_0\sigma_{\text{u-axial}}}, \tag{5.24}$$

where $\rho_{struct\text{-}axial}$ is the density of the axial structural support material. Note that, assuming the same material properties, this is ¼ of the mass required for the radial support structure.

While the use of light-weight materials can provide substantial mass savings for the radial support structure, a material which can withstand the high compression forces of the solenoid, such as aluminum, is still required for support in the axial direction. Eq. (5.24) demonstrates that the required axial support mass also varies as a function of B^2 and D^2, and Figure 5.7 shows the axial support mass requirements over the design trade space using a F_S of 1.4 and Aluminum 6061. This shows that the axial support mass becomes a significant contributor to the overall system mass at high field strengths and thicknesses. Therefore, the development of stronger, light-weight structural materials will contribute significantly to an active magnetic shielding design by reducing the overall system mass requirements.

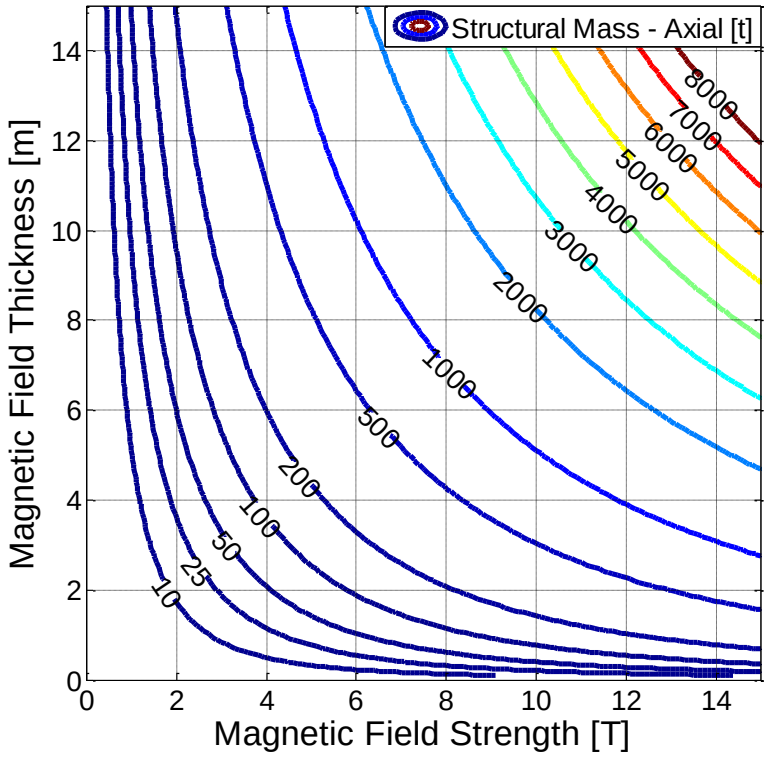

Figure 5.7 Axial Support Structure Mass, Aluminum 6061
(F_S = 1.4, $\sigma_{u\text{-}axial}$ = 2.7 g/cm^3, $\rho_{struct\text{-}axial}$ = 310 MPa)

5.3.3 Coil-to-Coil Forces and Additional Support Structure Mass

In addition to the structure required to contain the forces within a single coil, there are also coil-to-coil forces that must be accounted for. These are repulsive forces that arise from the interaction of each coil with the external magnetic field from the surrounding coils. A complete analysis of these forces is incredibly complex and far beyond the scope of this work, especially one covering the entire trade space discussed here. A brief analysis shows that the forces on an individual cylinder are roughly on the same order of magnitude as the axial forces. Therefore, for the purposes of this analysis, the coil-to-coil forces are assumed to be equal to the average axial force derived previously. Because this is a repulsive force, resulting in tensile stress on the

support structure, high-strength, light-weight materials such as Kevlar or Zylon can be used, similar to the radial support structure.

The mass of the coil-to-coil support structure for a single coil can be estimated by a single support that extends from the axial centerline of the shield to the center of the coil. The length of this support, L_{c2c}, is

$$L_{c2c} = r_i + D. \tag{5.25}$$

Assuming that the coil-to-coil force is equal to the average axial force, the equation for the cross sectional area of this support is identical to Eq. (5.22). Therefore, the coil-to-coil structural support volume required, $V_{struct\text{-}c2c}$, is then given by

$$V_{struct-c2c}(B,D) = A_{c2c}L_{c2c} = \frac{\mathrm{B}^2\mathrm{D}^2\left(r_i + D\right)\pi F_S}{16\mu_0\sigma_{\mathrm{u\text{-}c2c}}}, \tag{5.26}$$

where $\sigma_{u\text{-}c2c}$ is the ultimate tensile strength of the coil-to-coil structural support material. The coil-to-coil structural support mass required per coil, $m_{struct\text{-}c2c}$, is then given by

$$m_{struct-c2c}\left(\mathrm{B},\mathrm{D}\right) = \frac{\rho_{struct-c2c}B^2D^2\left(r_i + D\right)\pi F_S}{16\mu_0\sigma_{\mathrm{u\text{-}c2c}}}, \tag{5.27}$$

where $\rho_{struct\text{-}c2c}$ is the density of the coil-to-coil structural support material.

5.3.4 Structure System Key Technologies

Based on this survey of the structural system, the following key technology is identified for the development of an active magnetic shield:

1. Development of higher-strength, lighter-weight structural materials. Given the high mass contribution of the structural system, improvements in structural materials would greatly reduce the overall system mass.

5.4 Thermal System

The cryogenic temperatures required for superconductor operation have only limited space flight heritage. In order to ensure that the superconductor functions properly, the system's operating temperature must be kept below the superconductor's critical temperature, plus additional thermal margin to reduce the risk of quench. Cooling methods for superconductors are generally broken into two groups: "wet" or "dry/cryogen-free" (Iwasa, 2009). In wet systems, the superconductor is either placed in direct contact or thermal linked, via conduction or convection, to cryogenic fluid. Temperature is then maintained through the boil-off of this cryogenic fluid. The resulting boil-off gas is vented in an open-loop system, or may be condensed and recycled in a closed-loop system. In dry/cryogen-free systems, a crycooler is used to remove heat via a refrigeration cycle. The superconductor is either conductively or convectively linked to the cryocooler, with the latter option commonly known as a cryocirculator system. In a cryocirculator system the superconductor is convectively cooled by a coolant loop, and heat is removed from the returning fluid by a crycooler via a heat exchanger. The coolant fluid is usually cold hydrogen or helium gas, which have condensation temperatures at atmospheric pressure of 4.2 K and 20.3 K respectively.

A wet system would require a large vessel containing cryogenic fluid, also known as a cryostat, to surround each coil. For an open-loop design, excess cryogen would need to be provided for the lifetime of the system. The amount of excess cryogen required to enable long duration missions would be prohibitive, therefore, an open-loop system can be considered impractical for use in active magnetic shielding applications. To create a closed-loop system, cryocoolers are used to condense all of the cryogen boil-off, eliminating the need to include a life cycle reserve of cryogenic fluid. This would eliminate the need for excess cryogen capacity;

however, the amount of mass required for the cryogen and its containment structure would be significant. Although this type of system is not the lowest mass option, it will not be eliminated from further consideration since the thermal capacity of the cryogen may provide advantages in quench protection that outweigh the associated mass penalty. However, mass estimates for this system will not be presented since this is not the lowest mass option.

Like the wet, closed-loop system, a dry system would require cryocooler capacity sized to handle the maximum heat removal required by the superconductor system. The cryogen-free, conduction only option, i.e. cryocoolers with only conductively coupling to the superconductor, is considered impractical for a large scale system. This would require a significant number of small cryocoolers and result in thermal gradients across the superconductor. The addition of a convective heat transfer system (i.e. a cryocirculator system) would allow consolidation of heat removal capability into a smaller number of larger capacity cyrocoolers, as well as provide more even heat distribution across the superconductor system. However, a circulator system would require additional system mass in the form of the heat transfer fluid, fluid pumps/fans, system piping, and heat exchangers. A trade tree detailing the thermal system, and system down selection, is shown in Figure 5.8.

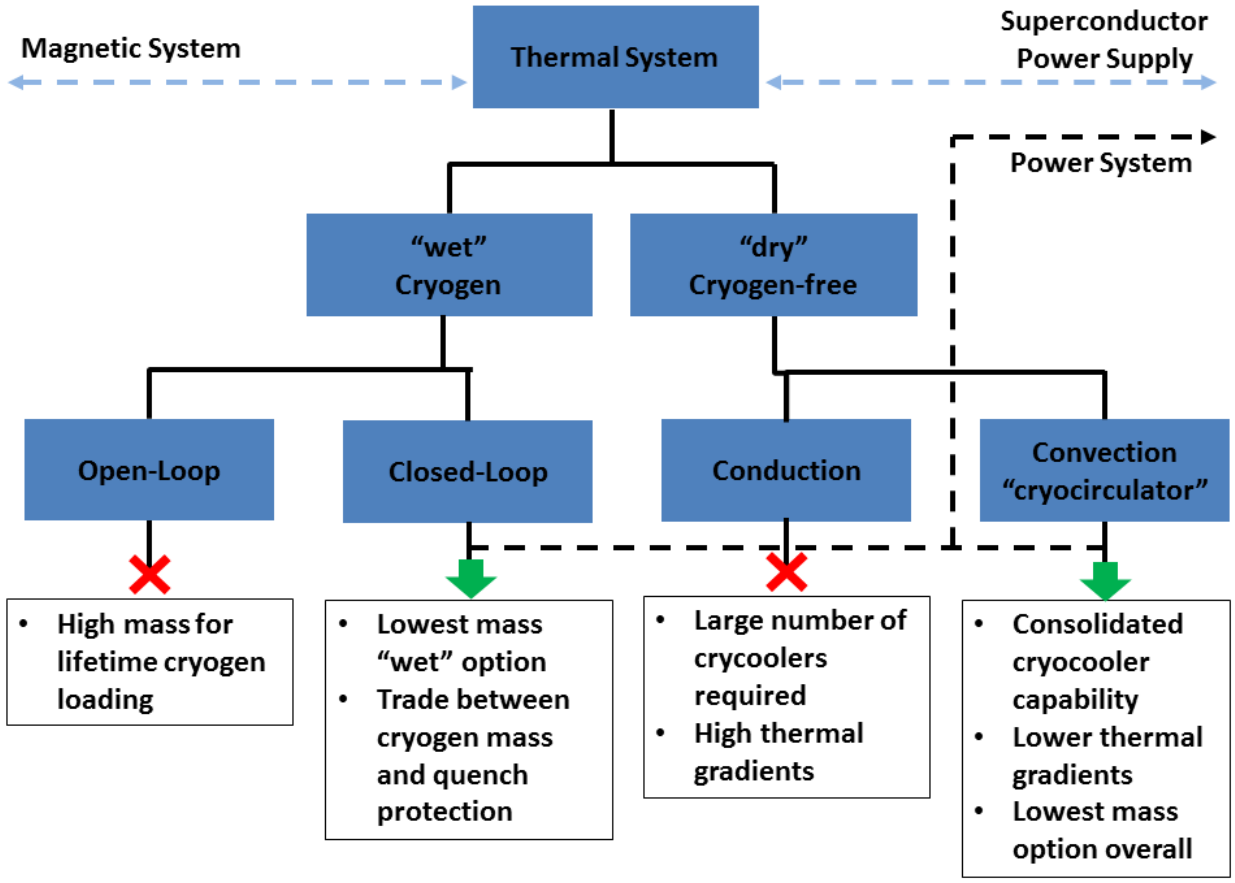

Figure 5.8 Thermal System Trade Tree

5.4.1 Heat Loads

There are three primary heat sources that must be compensated for during steady state operation of the active shield: external, internal and superconductor losses. External sources include radiative heating from solar, earth infrared (IR), and albedo flux sources. Internal heat sources are primarily due to the enclosed habitat module, which must be maintained at an operating temperature sufficient to allow human comfort. The active magnetic shield will be thermally coupled to the other modules and systems, including the habitat, but can be substantially thermally insulated from these heat sources while maintaining structural integrity.

Superconductor losses are primarily due to resistance losses, which will occur in the splice joints between lengths of superconductor material, and thermal leaks from the superconductor power supply. The sum of these heat loads dictates the heat removal requirements and sizing of the thermal system.

A conservative thermal analysis of the shield environment is first performed to determine the heat loads on the system due to the external and internal heat sources; superconductor losses are analyzed separately. Therefore, the analysis will only be a function of the shield size (i.e. field thickness) and independent of the magnetic field strength. The shield is assumed to be oriented so that its maximum cross sectional area is exposed to the incoming solar flux, with the sun perpendicular to the central axis, thus creating a design basis external thermal environment. By sizing the system so that it will function with this alignment, which results in the greatest amount of heat transfer from the sun, the design will result in no operational restrictions being placed on the system concerning attitude with respect to the sun. Additionally, optimal sun alignment could be used to minimize the solar heat input, and the resulting excess heat removal capacity can be used for transient cooldown of the system to operational temperatures. A sun shield could also be used to mitigate the external heat load; however, such a shield is not analyzed in this body of work.

The system is assumed to have three layers of multilayer insulation (MLI): one surrounding the habitat, one on the inner surface of the shield (facing the habitat), and one on the external surface of the shield (facing the space environment). In order to simplify the analysis the following assumptions are made:

1. Solar flux is determined at 1 AU from the sun;
2. Earth IR and Albedo fluxes are assumed to be negligible for deep space operations;

3. Heat losses through the side-walls are ignored, i.e. heat exchange only occurs in the radial direction (the side walls will likely be insulated to minimize thermal gradients within the coils); and
4. Conductive coupling between the shield and the habitat is assumed to be negligible (any conductive couplings will be heavily insulated to prevent thermal leakage into the superconductor system).

Figure 5.9, shows a cross section view of the analysis configuration, including the relevant thermal property assumptions used in this analysis, where α_s is the MLI solar absorptivity, ε_{IR} is the MLI IR emissivity, and ε_{eff} is the MLI effective emissivity.

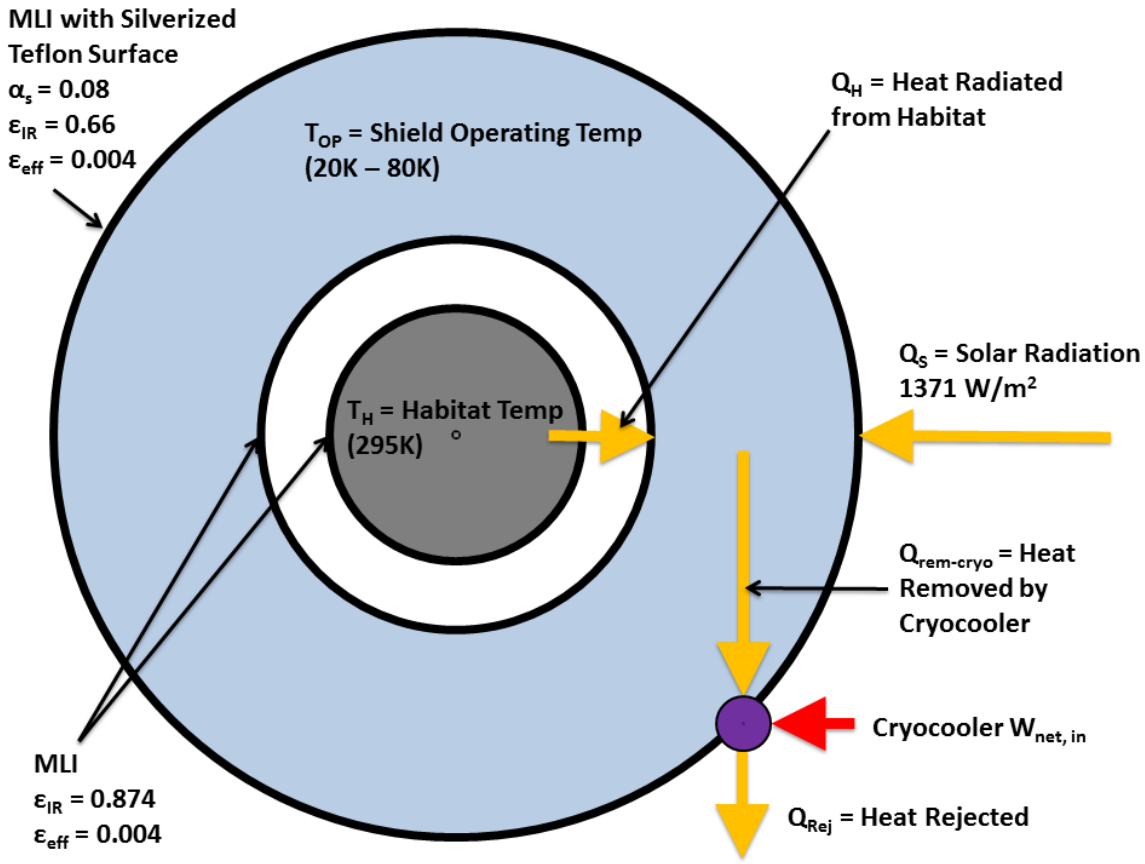

Figure 5.9 Thermal Analysis Configuration and Properties
(Thermal surface properties from Brown, 2005)

The results of the thermal network depicted depend, to a large extent, on the effective emissivity of the MLI material. The MLI dimensions for such a design will be large and the configuration will likely allow for low number of discontinuities (seams, penetrations, etc.). Therefore, a value of 0.004 was selected based upon the MLI performance values given by Stimpson and Jaworski (1972). An effective emissivity value of 0.002 is reasonable; however, 0.004 was selected to be conservative.

Solving the thermal network depicted in Figure 5.9, for a range of superconductor operating temperatures and magnetic field thicknesses, yields the external and internal heat loads, as shown in Figure 5.10. For this case, the habitat radius is selected to be 3m and the inner diameter of the magnetic field is selected to be 4m. Figure 5.10 demonstrates that these heat loads vary little as a function of the system operating temperature. The contribution to the total heat load from the habitat is approximately 370 W. The difference between the habitat contribution and the total heat load is the contribution from solar radiation. As the magnetic field thickness increases, and therefore the shield's cross sectional area, the amount of heat removal required also increases as more heat is absorbed from the sun.

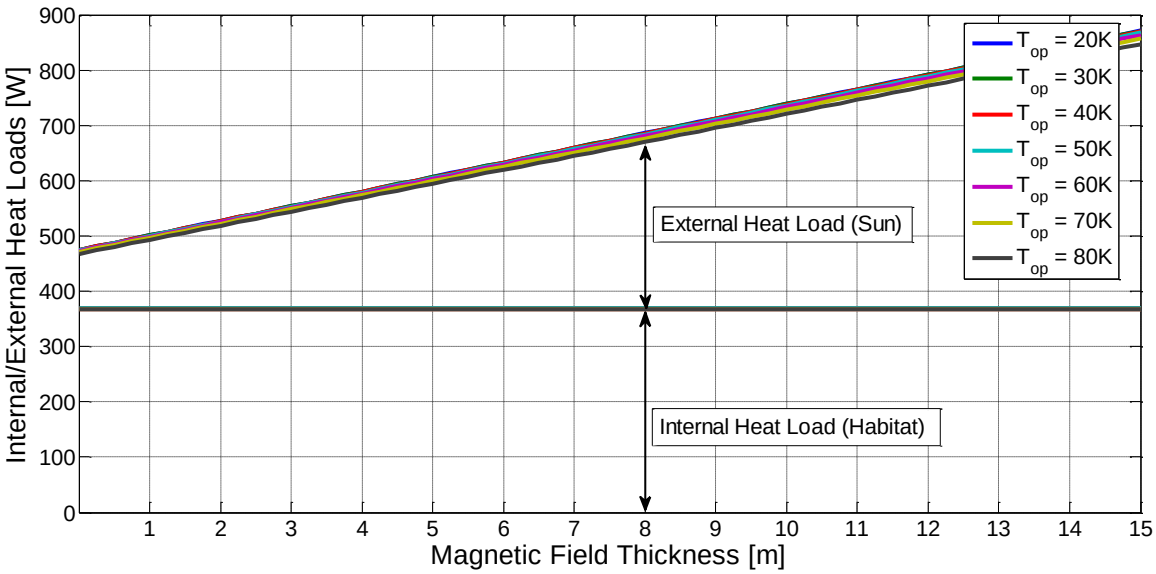

Figure 5.10 Internal and External Heat Loads

The heat load contribution from superconductor losses is a function of both the magnetic field thickness, which dictates the length of superconductor tape/wire, and the magnetic field strength, which specifies the electric current required and drives the resistance losses at each splice junction. The overall length of superconductor tape/wire required for a single coil, $L_{w/t}$, is given by

$$L_{w/t}\left(B,D\right)=\frac{n_{layers}\pi Dl}{w_t}. \tag{5.28}$$

Therefore, the total number of splices in a coil, n_{splice}, is

$$n_{splice}(B,D)=\frac{n_{layers}\pi Dl}{w_t L_{\max}}, \tag{5.29}$$

where L_{max} is the maximum manufacturing length of a piece of superconducting tape/wire. If the system is sized such that it is operating at the maximum electric current capacity of the superconductor tape/wire, the total heat dissipation per coil from resistance losses at splice junctions, Q_{splice}, is given by

$$Q_{splice}(B,D)=\left(\frac{i}{n_{layers}}\right)^2 R_{splice}n_{splice}. \tag{5.30}$$

where R_{splice} is the resistance of a splice junction. Substituting Eq. (5.3) for i, Eq. (5.5) for n_{layers}, and Eq. (5.29) for $n_{splices}$ into Eq. (5.30) yields

$$Q_{splice}(B,D)=\frac{J_e A_t R_{splice}\pi BD\sqrt{D^2+l^2}}{\mu_0 L_{\max}}. \tag{5.31}$$

Figure 5.11 shows an example of the contribution of superconductor losses over the design trade space using a splice resistance of 20 nΩ (SuperPower Inc.), a maximum superconductor current capacity of 250 A (i.e. $J_e A_t$ = 250 A), and a maximum tape/wire manufacturing length of 1 km.

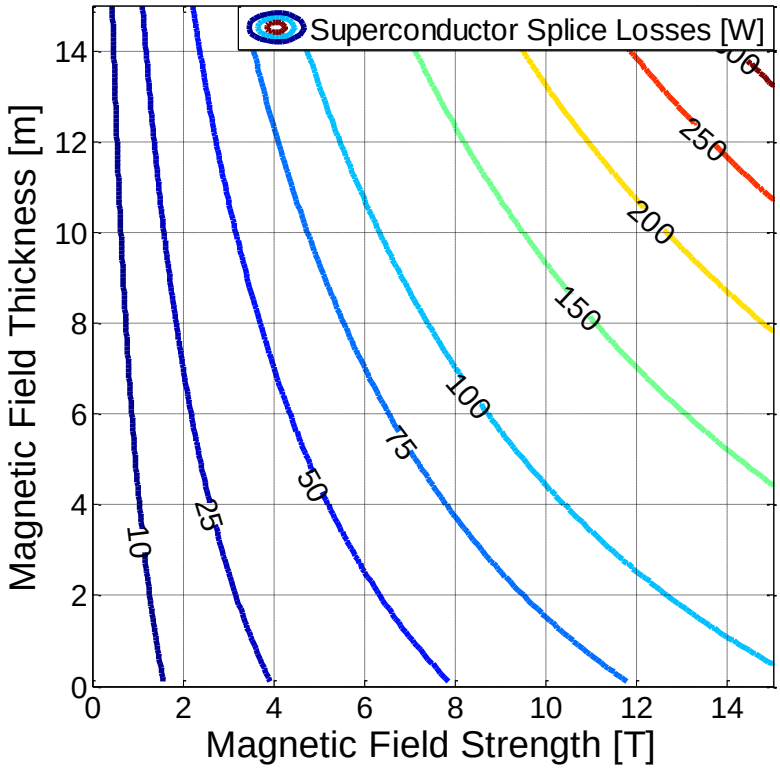

Figure 5.11 Superconductor Splice Losses

5.4.2 Cyrocoolers: Performance, and Mass Estimates

There are five common cryocooler types used for cryogenic cooling: Joule–Thomson, Brayton, Stirling, Gifford–McMahon, and pulse tube cryocoolers. A discussion of these different types is beyond the scope of this study; however, an excellent review of their operation, applications, state-of-the-art capabilities, and a comparison between the different types is given by Radebaugh (2004 and 2009) and de Waele (2011). While each type functions under a different principle of operation, they all rely on the basic refrigeration cycle. The thermodynamic efficiency, or Coefficient of Performance (*COP*), for a refrigeration device, COP_R, is defined as the ratio of the heat removed, Q_L, to the net work input required for the system, $W_{net,in}$,

$$COP_R = \frac{Q_L}{W_{net,in}}. \tag{5.32}$$

These systems are usually compared to the ideal refrigeration cycle, or the reverse Carnot cycle. The reverse Carnot cycle is a theoretical, reversible thermodynamic cycle which defines the limit of a refrigeration cycle's efficiency for operation between two different temperature levels. The Carnot efficiency ($COP_{R,Carnot}$) can be expressed as a function of the system's low temperature refrigerated source, T_L, and the high temperature heat sink, T_H, (Cengel and Boles, 1998) by

$$COP_{R,Carnot} = \frac{1}{\frac{T_H}{T_L} - 1}. \tag{5.33}$$

Eq. (5.33) shows that as T_L decreases, the Carnot efficiency also decreases. For the thermal system being analyzed, the superconductor operating temperature, T_{op}, is identical to T_L. Thus, as the operating temperature is lowered, the Carnot efficiency of the system's cryocoolers will decrease. However, the Carnot efficiency is a theoretical limit for a device operating between two different temperatures. The true efficiency of a device is lower than this and cryocooler efficiencies are often expressed as a percentage of Carnot efficiency, η. Therefore, the overall efficiency may be expressed as

$$COP_R = \frac{\eta}{\frac{T_H}{T_{op}} - 1}. \tag{5.34}$$

A survey of cyrocooler efficiencies, as a percentage of Carnot, has shown that these efficiencies are largely a function of the cryocooler heat removal capacity and are not a strong function of T_L (Kittel, 2007). As shown earlier, the heat removal requirements for the active shielding system discussed will be on the order of hundreds of Watts. Therefore, a corresponding efficiency of 10% of Carnot is selected as a conservative estimate, given the size of cryocoolers required

(Kittel, 2007). Using this value, the overall cyrocooler efficiency as a function of system operating temperature is shown in Figure 5.12.

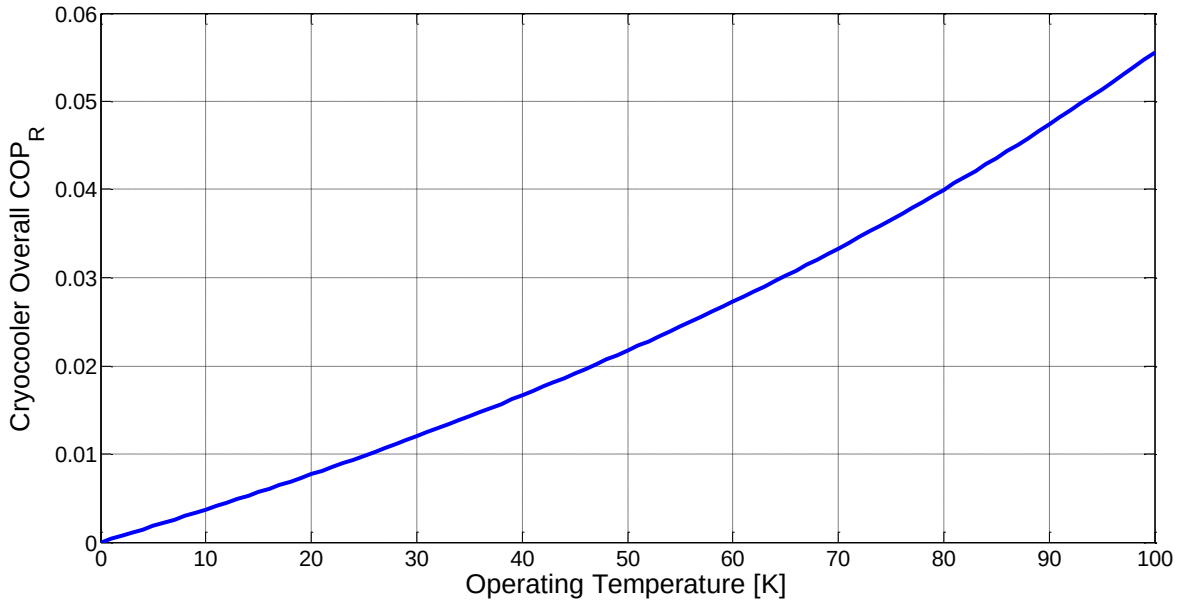

Figure 5.12 Cryocooler Total Efficiency (COP_R)

The mass of cyrocoolers may be estimated as a function of their required input power (Kittel, 2007) by

$$m_{Cryocooler} = 0.0711 W_{net,in}^{0.905}. \tag{5.35}$$

Combining Eqs. (5.32), (5.33), and (5.34) to solve for cryocooler mass as a function of the system heat removal requirements yields

$$m_{Cryocooler} = 0.0711\left(\frac{1}{\eta} Q_L \left(\frac{T_H}{T_{op}} - 1\right)\right)^{0.905}. \tag{5.36}$$

Figure 5.13 shows an example of the total system crocooler mass over the design trade space using a heat sink temperature, T_H, of 280K and a superconductor operating temperature, T_{op}, of 40K. The total system heat removed, Q_L, is calculated using the internal and external loads shown in Figure 5.10 and the superconductor splice losses shown in Figure 5.11.

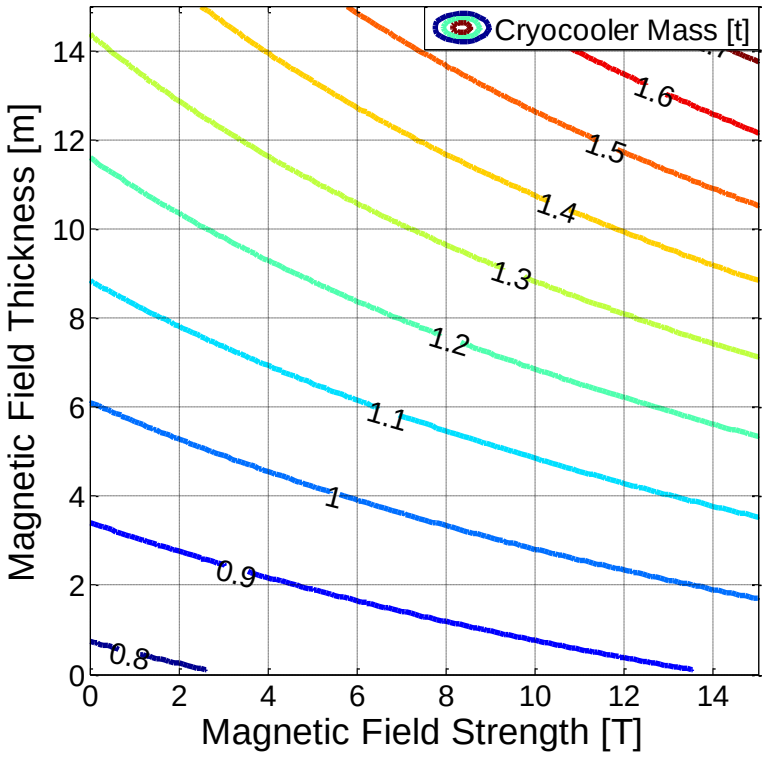

Figure 5.13 System Cryocooler Mass

While these mass values are not negligible, they are significantly lower than those required for the superconductor and support structure systems, particularly at high bending powers. Additional thermal system mass, such as circulator fans, heat exchangers, and piping, can be estimated by applying a small correction factor to the cryocooler mass. It is assumed that much of the required cyrocooler piping can be eliminated by incorporating hollow bores into the axial support structure to minimize the need for additional mass.

5.4.3 Cyrocooler Spaceflight Heritage

Crycoolers have been utilized onboard numerous space systems and an excellent review of their space applications is given by Ross and Boyle (2006), including the cryocooler systems utilized onboard the AMS experiment and the Hubble telescope. However, the cooling capacity

of these flight systems is limited, with most systems providing less than 10 W of cooling. Many terrestrial cryocoolers have capacities in the mid-100 W range, with some capable of the low kW range. Unfortunately, many of these terrestrial based systems do not meet the high reliability requirements necessary for space applications (Radebough, 2009). Thus, the development of high capacity, low mass, space qualified cryocoolers is essential for the development of active magnetic radiation shielding.

5.4.4 Heat Rejection Requirements and Radiation Sizing

Figure 5.12 demonstrates that the overall efficiency of cyrocoolers is low, resulting in high cyocooler power requirements and high heat rejection requirements. Additionally, the overall cryocooler efficiency decreases with lower operating temperatures; therefore, the selected operating temperature will have a significant impact on the thermal and power systems. Figures 5.14 and 5.15 show the cryocooler power and heat rejection requirements as a function of the total system heat load (the sum of external, internal, and superconductor loss loads) for various operating temperatures. These plots highlight the competing drivers for the selected superconductor operating temperature. While lower temperatures are desirable for superconductor operation, resulting in higher critical current densities and larger thermal quench margins, they also drastically increase the thermal and power system requirements.

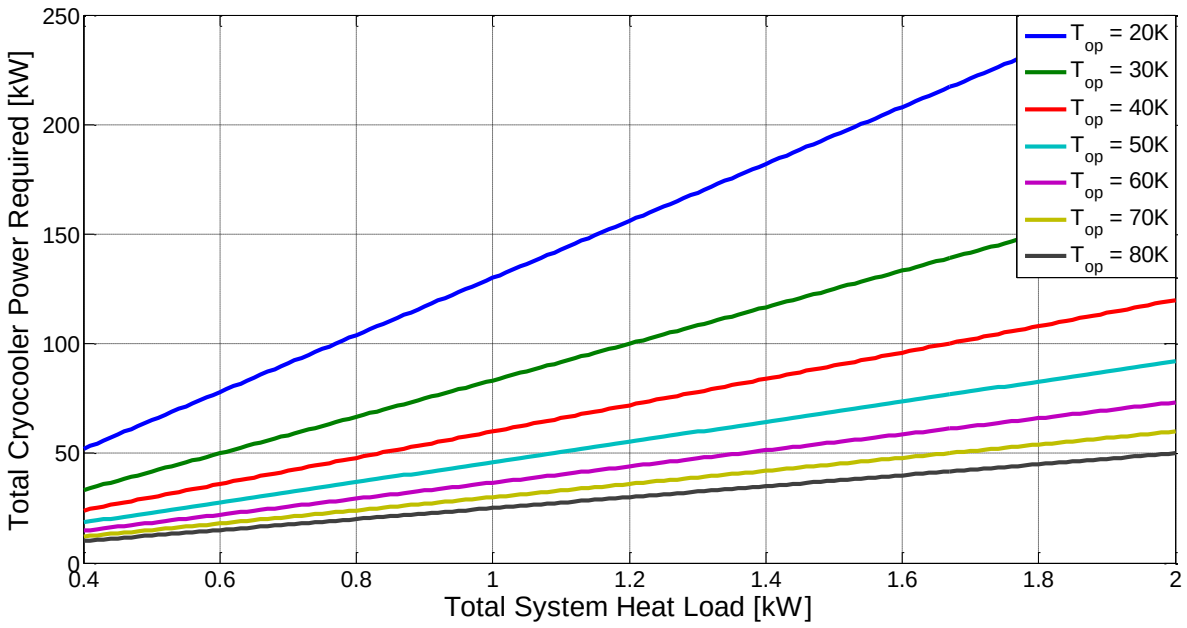

Figure 5.14 Total Cryocooler Power Requirements

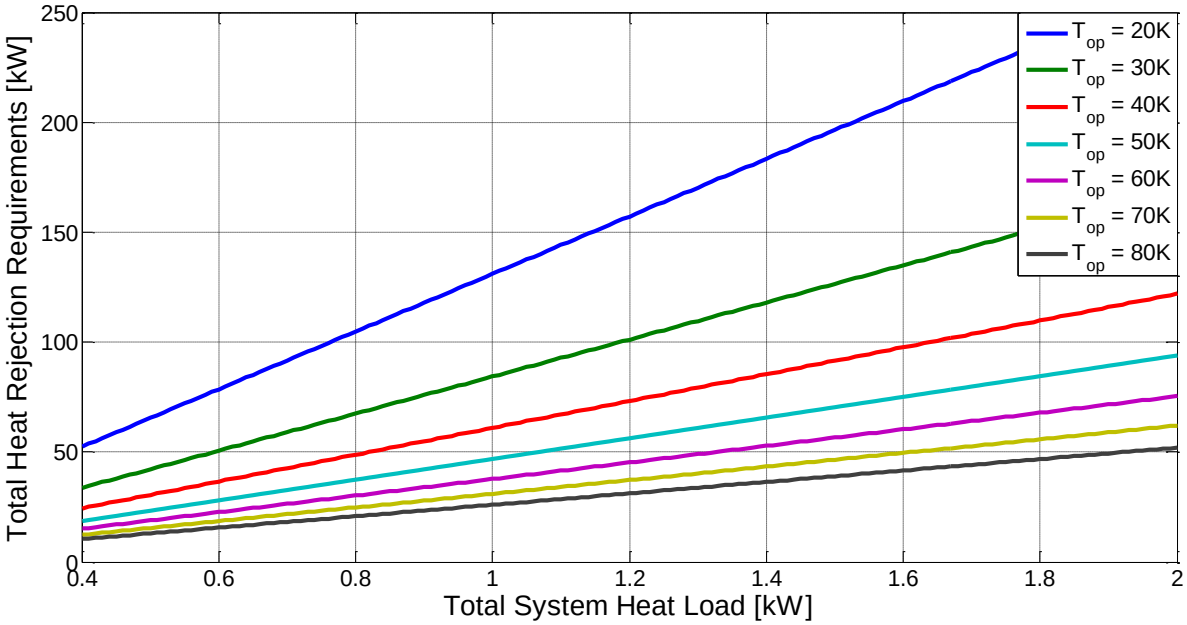

Figure 5.15 Total Thermal System Heat Rejection Requirements

The large heat rejection requirements of the thermal system will require large radiators to reject this energy. The ISS radiators may be used as a point of reference for the radiator sizing

requirements. The ISS uses 6 Heat Rejection System (HRS) radiators. Each radiator weighs approximately 1120 kg, is 73.56 m^2, and can reject at least 11.8 kW (Lockheed Martin Corp. website). As an example, a shield composed of 1T x 8m coils would have a heat load of approximately 692W (combined internal and external load of ~680W, Figure 5.10, and superconductor losses of ~12W, Figure 5.11). Selecting an operating temperature of 40K, the thermal system would need to reject approximately 42.2 kW of heat. Therefore, this system would require radiators with a total mass of 4005 kg and a surface area of 263 m^2 (equivalent to approximately 3.6 ISS HRSs).

5.4.5 Thermal System Key Technologies

Based on this survey of the thermal system, the following key technologies are identified for the development of an active magnetic shield:

1. Development of space qualified, high capacity cryocoolers. These are essential for the operation of large scale superconductor systems in space. Additionally, the development of this technology has direct applications in other space related topics, such as high powered, cryogenic scientific instruments and long-term cryogenic propellant storage.
2. Improvements in cryocooler efficiency. Even marginal improvements in efficiency can greatly reduce the overall thermal and power system requirements.

5.5 Power System

The power system must be capable of charging the superconducting coils, maintaining the desired operating current, and also provide for the high power requirements of the thermal system. Providing the necessary power for the thermal system is straightforward and simply a

matter of sizing the solar arrays, or other source, to meet the system load requirements. However, providing power for the superconducting magnetic coils, which operate at extremely high currents, is a unique problem.

5.5.1 Superconductor Power System

A LTS magnetic coil can be operated in what is known as "persistent" mode, where the lack of resistance would allow current to flow through the coil indefinitely. Persistent mode operation can be achieved by using an external power source to charge the coil to the desired current level and then creating a superconducting short between the terminals of the power source. At this point, the power supply leads can then be disconnected from the terminals to minimize heat leakage from the leads. This is the strategy employed on the AMS experiment (Chung et al., 2005).

Unfortunately, the properties of HTSs are such that they are "intrinsically dissipative," and a variety of conditions will result in system losses. These losses are generically termed "AC losses" and a thorough description may be found in Iwasa (2009). In addition to AC losses, any system of the scale presented here will inevitably require splices between lengths of superconductor cable. Although the resistance introduced by these splices is relatively low, the large currents required for high field operation can result in significant losses. Therefore, an HTS system will not be able to operate in a true persistent mode and a power supply will need to remain connected to the system in order to compensate for these losses.

In terrestrial HTS systems a variety of power supply solutions are available and different techniques can be employed to accommodate heat leakage from the power supply lead connections. However, in a space environment these problems are not so easily remedied.

Because a normal power supply will operate at non-superconducting temperatures, a significant heat leak is presented by the power supply leads. This thermal leakage is not easily compensated for in the space environment, as demonstrated in the thermal system analysis. Additionally, the high currents desired for use in active magnetic shielding designs would result in high resistance losses in the non-superconducting material on the power supply side, further compounding the associated thermal challenges. While these problems may be accounted for, their effects are undesirable.

An alternative to a traditional power supply source is the use flux pumps (Kervendal et al., 2009), which are devices capable of supplying the high dc current required by the superconductor system. Flux pumps fall into three general categories: flux compressors, dc dynamos, and transformer rectifiers. A thorough review and discussion of each is given by van de Klundert and ten Kate (1981a). The first two types require mechanical work to supply the necessary current; however, transformer rectifier flux pumps utilize a low ac current, non-superconducting source and can be constructed with no moving parts, making them ideal for space applications. Additionally, transformer rectifier flux pumps have the greatest success of the various flux pump designs, in terms of the maximum current achieved, and are the only type actively employed in an operational system. Therefore, transformer rectifier flux pumps are the only type which will be considered further here. A trade tree detailing the power system, and the superconductor power supply down selection, is shown in Figure 5.16.

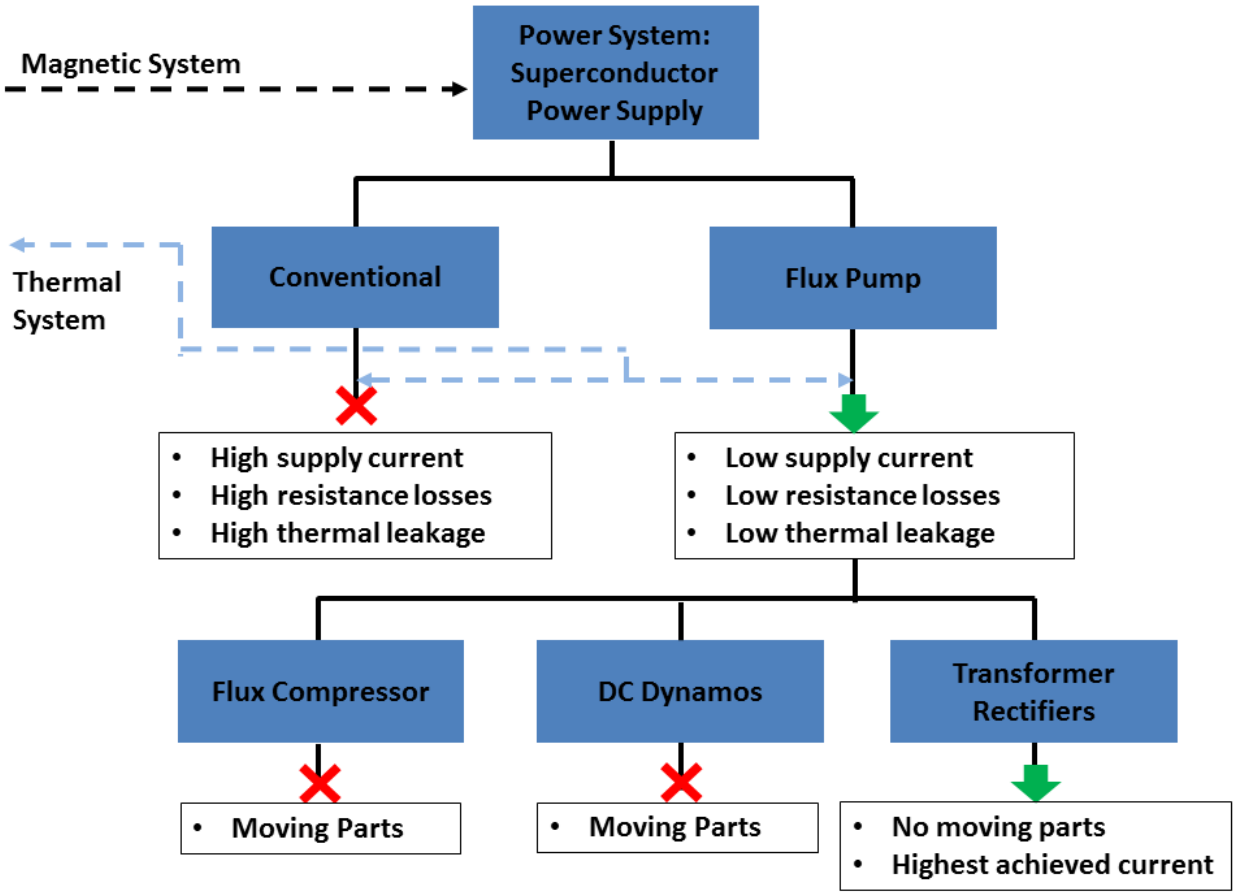

Figure 5.16 Power System: Superconductor Power Supply Trade Tree

5.5.2 Flux Pump Operation and State-of-the-Art

The simplest transformer rectifier flux pump is the half-wave rectifier flux pump, shown in Figure 5.17. In the initial state, switch 1 is closed and switch 2 is open, completing the circuit between the load and the secondary coil in the transformer. As the current in the primary loop increases, so does the current in the secondary loop. At the peak of the primary current, switch 1 opens and switch 2 closes, effectively allowing the load current to bypass the transformer. The current in the primary loop then decreases and, at the minimum current, the switches reset to their original position and the cycle starts again. Thus, each half-cycle of the primary loop

creates a “pumping” action in the secondary loop, allowing the current to be incrementally increased. There are numerous transformer rectifier designs (van de Klundert and ten Kate, 1981b), including full-wave designs which take advantage of each side of the primary loop ac current wave, but each relies on this basic principle. It is important to note that the switches in the superconducting loop may be either conventional mechanical switches or thermally activated superconductor switches, where a section of superconductor is heated so that it is no longer superconducting, effectively creating an open switch.

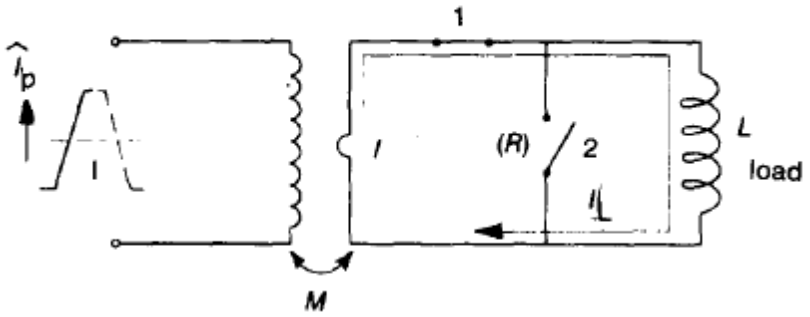

Figure 5.17 Transformer Rectifier Type Flux Pump: Half-Wave Rectifier
(van de Klundert and ten Kate, 1981a, reprinted with permission from Elsevier)

Given the characteristics of flux pumps, utilizing these as power supplies for the superconductor coils would provide significant benefits in active magnetic shielding applications. Unfortunately, today most flux pump technology remains in the experimental stage. In the early 1990’s, Mulder, van de Klundert, ten Kate and their colleagues developed a thermally switched, full-wave, transformer rectifier flux pump which was successfully tested up to 60 kA (Mulder et al., 1991). Despite this achievement, use of these devices did not take hold, and to date the only flux pump devices which appear to have made it to full scale development are LTS flux pumps employed in the CMD-2 and CMD-3 detectors at the Budker Institute of Nuclear Physics in Russia (Barkov et al., 1999; Karpov et al., 2006). These particular flux pump devices have been in operation since 1989; however, their maximum current capability is approximately 1.5 kA,

lower than what is generally required for active magnetic shielding applications. Since early 2000, research and development of these high current designs seems to have largely languished, and flux pump devices, with the exception of CMD-2 and CMD-3, exist only in the experimental and prototype phase. Therefore, further R&D efforts will need to be placed in the development of these devices. Although successful high current prototypes have been developed, these studies were conducted nearly 20 years ago and significant effort will likely be necessary in order to revive these programs and construct the necessary space qualified hardware. Mass estimates for these devices are difficult to obtain; however, the 60 kA flux pump design by Mulder et al. (1991) does show that these devices are rather small. Therefore, the mass of these devices will be ignored since they are negligible when compared to the other system masses presented.

5.5.3 Solar Arrays

The power required for the operation of the thermal system, primarily the cryocoolers, will be the dominate power load for an active magnetic shielding design. Figure 5.14 demonstrates the total cyrocooler power requirements as a function of the shield size and selected superconductor operating temperature. Solar array mass and size requirements are estimated using Triple Junction (TJ) GaAs rigid panel solar arrays, which are common for many space applications. These arrays typically have specific power values of 70 W/kg and provide 3.12 W/m^2 of surface area (Bailey and Raffaelle, 2011).

As an example, a shield composed of 1T x 8m coils would have a heat load of approximately 692W (combined internal and external load of ~680W, Figure 5.10, and superconductor losses of ~12W, Figure 5.11). Selecting an operating temperature of 40K, the thermal system would require approximately 41.5 kW of power to operate the cryocoolers. The

superconductor power system would also need to supply 12W to the flux pumps to compensate for superconductor losses; however, this value is negligible when compared to the cyrocooler power requirements. Based upon the Triple Junction (TJ) GaAs rigid panel solar arrays performance stated earlier and assuming a distance of 1 AU from the sun, this system would require solar arrays with a total mass of 593 kg and a surface area of 129.5 m^2.

5.5.4 Power System Key Technologies

Based on this survey of the power system, the following key technology is identified for the development of an active magnetic shield

1. Development of high current, transformer rectifier HTS flux pumps. Because of the distinct advantages offered by flux pump technology over traditional power sources, high current capability transformer rectifier flux pumps are ideal for the operation of large scale superconductor systems in space. These devices would reduce the resistance losses and heat leaks from the superconductor power supply, reducing the requirements for the thermal and power systems.

5.6 Chapter Summary

The major active shielding systems (magnetic/superconductor, structure, thermal, and power) are surveyed and mass and material estimates are provided for each. These provide a picture of the large scale of these systems, as well as highlighting their dependence on the primary design parameters: magnetic field strength and field thickness. In the following chapter, these mass estimates will be incorporated into the rapid analysis model so that mass and material effects may be automatically accounted for.

The survey and trade study analysis of these systems resulted into a down selection of possible system architectures:

1. Magnetic/Superconductor System: HTS superconductor such as YBCO tape or BSCCO wire.
2. Structural System: mixed material design with high-strength, light-weight options such as Kevlar or Zylon used for radial support.
3. Thermal System: cryocirculator system (although a wet, closed-loop system could be employed at a higher mass penalty is greater quench protection is needed).
4. Superconductor Power System: transformer rectifier flux pumps.

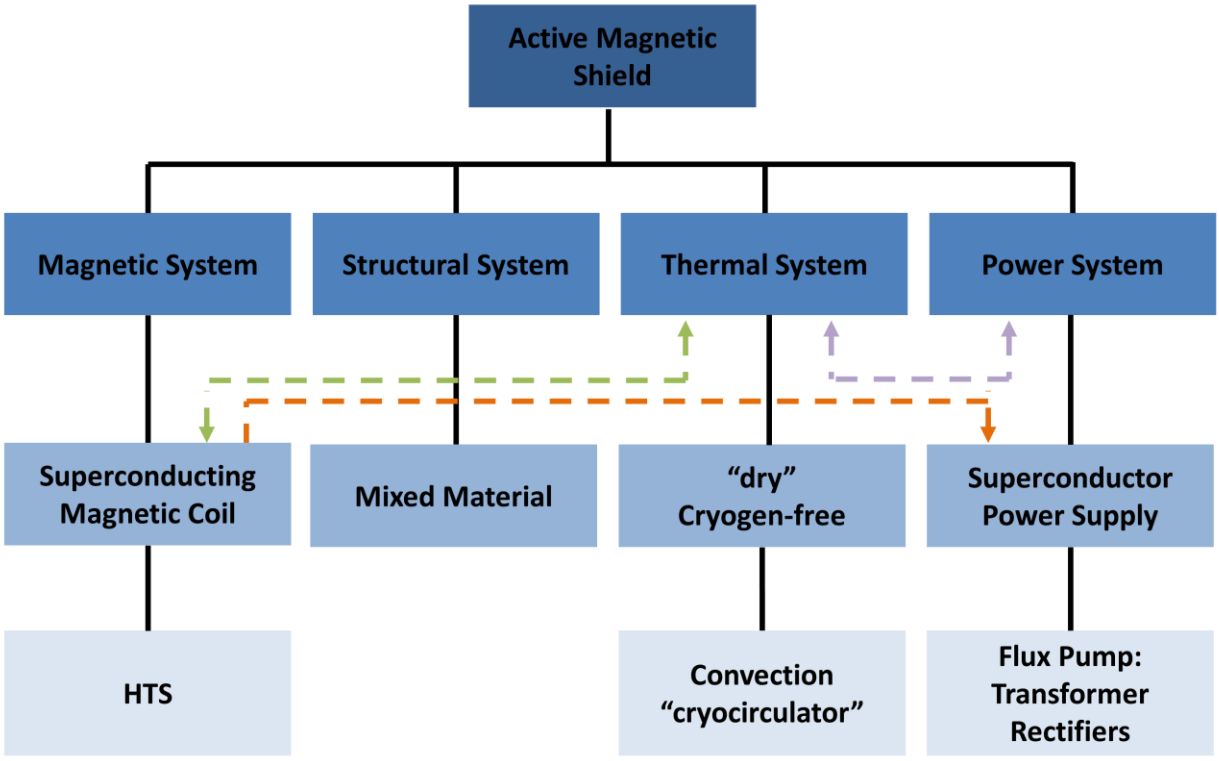

Figure 5.18 Active Magnetic Shield Trade Tree Summary

The survey of these systems also allowed the identification of the following key technologies, which are either enabling for such a design or would provide significant mass or performance improvements:

1. Metallurgical and manufacturing improvements to increase the critical current density of existing superconductor material.
2. Metallurgical and manufacturing improvements to increase the engineering current density of existing superconductor materials.
3. Manufacturing improvements to increase the maximum achievable length of superconductor wires and tapes.
4. Development of improved superconductor splice technology.
5. Development of new, higher temperature superconductors.
6. Development of higher-strength, lighter-weight structural materials.
7. Development of space qualified, high capacity cryocoolers.
8. Improvements in cryocooler efficiency.
9. Development of high current, transformer rectifier HTS flux pumps.

Chapter 6

Rapid Analysis Model with Adjusted Mass Estimates

The previous chapter presented a system survey of a solenoid active magnetic shield design in order to calculate mass and material estimates over the design trade space. This chapter combines these estimates with the rapid analysis model presented in Chapter 4. A design is then analyzed using this model, with the mass and material quantities automatically adjusted as a function of the trade space design variables, and the results presented allow additional insights into the characteristics of such a design. A comparison is also performed applying the modeling work developed here to a similar design that was analyzed using Monte Carlo techniques (Westover et al., 2012).

6.1 Addition of Active Shielding System Mass Estimates

The system mass and material estimates are incorporated into the rapid analysis model using the configuration shown in Figure 6.1. First, the flux in the barrel region is determined as a function of magnetic field strength and thickness, as described in Chapter 4. Then, using the system mass estimates discussed in the Chapter 5, the shield system mass for each material type is determined as a function of the magnetic field strength and thickness. This mass is smeared over a cylinder that is located at the center of the magnetic field, as shown in Figure 6.1. This cylinder provides the average thicknesses of the various shielding materials that the flux in the barrel region flux will pass through. The barrel region flux is then transported, using

HZETRN2010 (Wilson et. al, 1995; Slaba et. al, 2010a, 2010b), through these average thickness values. The resulting flux output is then transported again through the habitat, and the resulting dose equivalent is combined with the habitat end cap region dose equivalent contribution. Because the end cap region flux is unaffected by the magnetic field, the end cap dose equivalent contribution may be calculated separately.

This method transports each particle in the barrel region through the same average thickness value of each shielding material; however, this is only an approximation. Each particle will pass through a different amount of mass, depending on the approach angles of the particle and the exact geometry of the active shielding design. Therefore, this approximation introduces some uncertainty into the analysis results. Future work using Monte Carlo transport codes can include more detail and quantify the effects of this approximation.

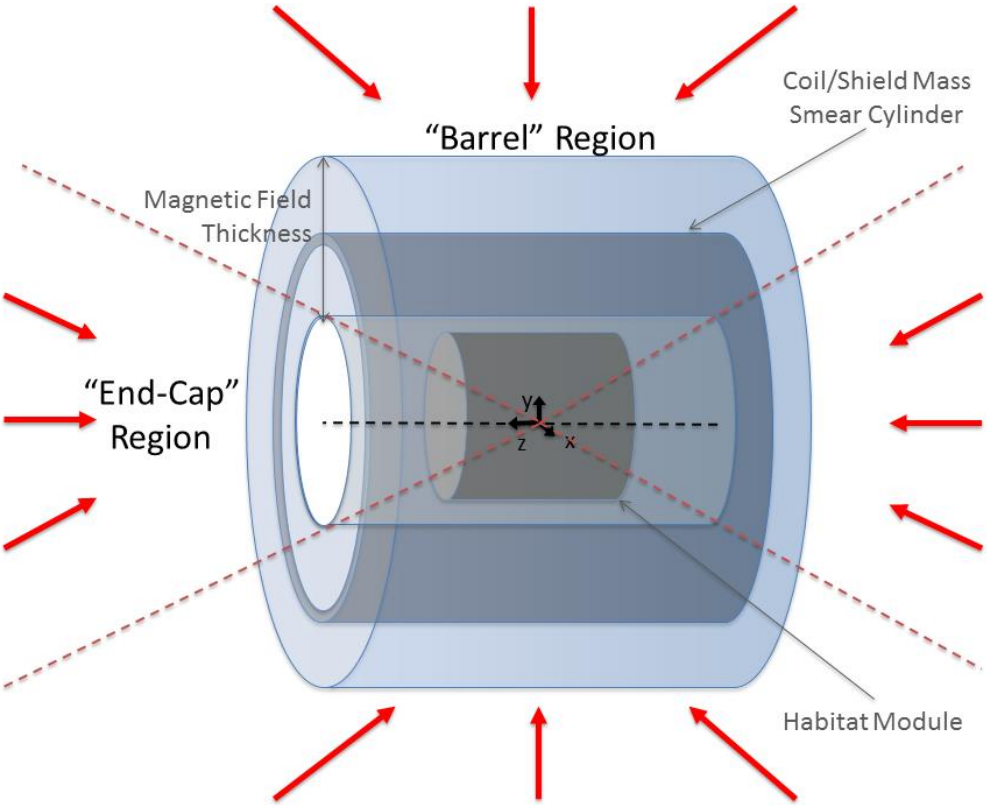

Figure 6.1 Model Geometry and Mass Locations

6.2 Trade Space Analysis with Automatically Adjusted Mass Estimates

6.2.1 Analysis Parameters

An analysis is conducted using the method outlined in Section 6.1 and the mass and material estimates presented in Chapter 5. The following assumptions are made for the results presented:

1. Superconductor system: HTS
    a. Material: YBCO tape
    b. Dimensions: 5 cm wide, 0.1 mm thick
    c. J_e: 87 kA/cm^2, assuming 29 kA/cm^2 at 77K and self-field, with an average of 3x capability for operation at 40K (Hazelton, 2012)
2. Structural system: Mixed-Material
    a. Radial Structural Material: Kevlar 49
    b. Axial Structure Material: Aluminum 6061
    c. Coil-to-Coil Structural Material: Kevlar 49
    d. Safety Factor: 1.4
3. Thermal System: Cyrocirculator type
    a. Additional System Mass: circulator fans, heat exchangers, and piping are accounted for by adding three times the cyrocooler mass
    b. Material: Aluminum 6061
    c. The radiators mass is not included in the barrel region mass since these will likely be located farther away, near the end caps
4. Power System: Flux Pump and Solar Arrays

a. The flux pump mass is considered negligible

b. The solar array radiators mass is not included in the barrel region mass since these will likely be located farther away, near the end caps

5. Shield Dimensions:

   a. r_i = 4m

   b. l = 20m

6. Habitat Dimensions:

   a. r_H = 3m

   b. l_{hab} = 10m

   c. Cylinder Wall Thickness: 13.0 g/cm^2 Aluminum 6061, 1.36 g/cm^2 water

   d. Cylinder End Cap Thickness: 25.0 g/cm^2 Aluminum 6061, 1.36 g/cm^2 water

The selected habitat dimensions allow a pressurized volume of 282.7 m^3. This is similar in size and dimension to what has been proposed for a 4 crew member, 380 day asteroid mission (Rucker and Thompson, 2012). Based on historical data, a habitat of this size corresponds to a mass of approximately 32 t (Heinemann, 1994). Smearing this mass over the surface area of the habitat results in a shielding thickness of 4.8 cm (13 g/cm^2), which is assumed to be entirely Aluminum 6061. The water mass for a long duration trip can provide substantial shielding and is also considered. For this scenario, it is assumed that a closed-loop water supply system is employed and that a sufficient water reserve is provided for a crew of 4 for 30 days. The daily consumption of water, for drinking and food rehydration, is assumed to be 2.5 kg/p-day (NASA, 2010) and additional water requirements, for hygiene and housekeeping, are assumed to be 25.4 kg/p-day (Reed and Coulter, 2000), for a total of 27.9 kg/p-day. This results in a total water mass

of 3348 kg. Smearing this over the surface area of the habitat results in a water shielding thickness of 1.36 cm (1.36 g/cm^2).

The end-cap regions of the active shield will make a likely location for additional items, and the shielding in this region will be substantially higher than the 13 g/cm^2 calculated for the habitat wall. These additional items may include units such as a crew module, service module, and docking stations. Therefore, the habitat end-cap thickness is roughly doubled, to 25 g/cm^2 of aluminum, to account for this additional mass.

6.2.2 Analysis Results: Mass and Dose Equivalent

The results for the system and habitat described are shown in Figure 6.2. This plot also shows the total active magnetic shielding system mass, which is the sum of the superconductor, structural, thermal, and power systems masses, less radiator and solar array mass. It is assumed that the required radiators and solar arrays will be integrated into the larger thermal and power systems of the overall vehicle architecture; therefore, their mass is not included in this total. The mass is given in metric tons, and the color scale also shows this value in terms of the number of Space Launch System (SLS) launches required to place this mass in low-earth orbit. This assumes a maximum SLS capability to LEO of 70 t per launch, based on the SLS "70-metric-ton Initial Configuration" (SLS Fact Sheet, NASA website).

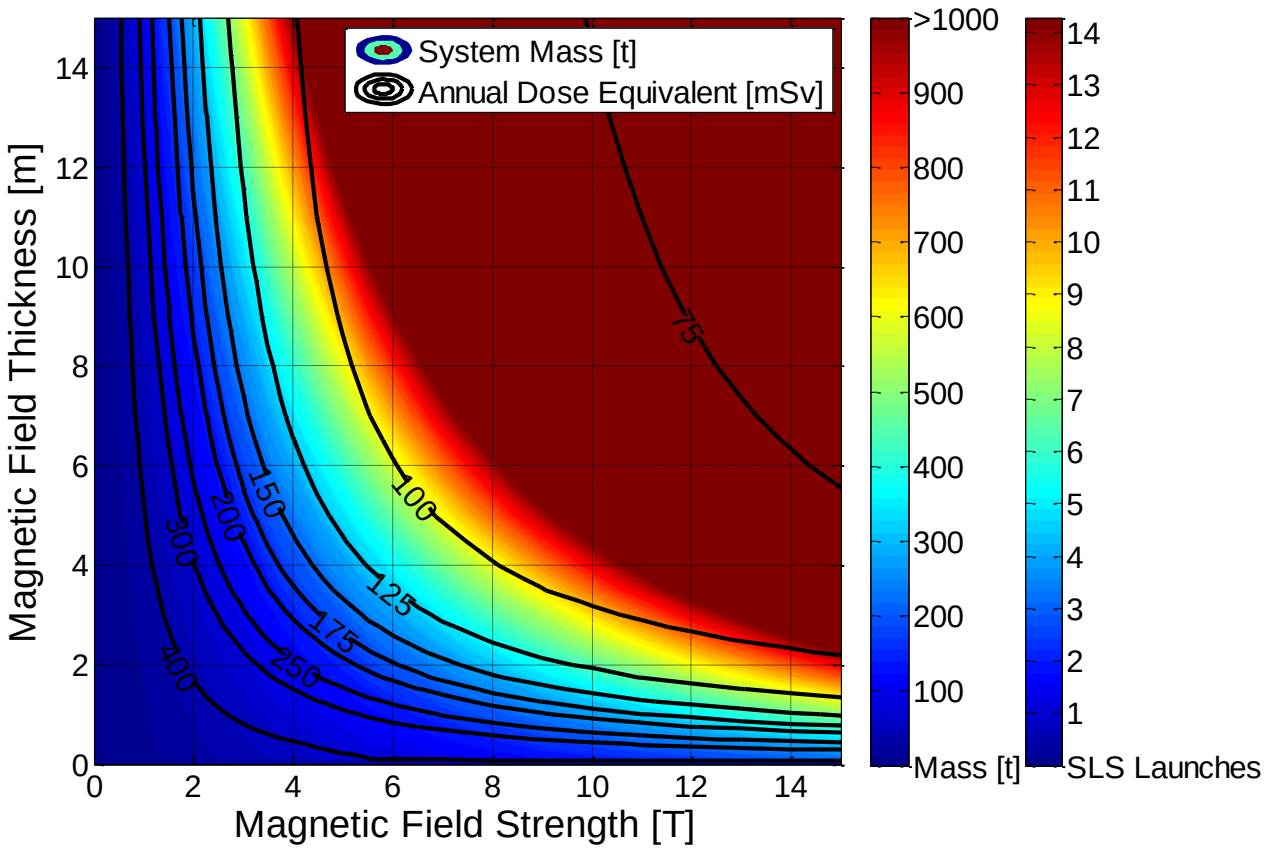

Figure 6.2 Annual Dose Equivalent and Active Shielding Mass

Similar to the results in Chapter 4, a higher field strength is more effective at reducing dose equivalent than a larger field thickness (e.g. 10T x 2m yields ~125 mSv/yr, 2T x 10m yields ~185 mSv/yr). However, this does not result in the lowest system mass. Figure 6.2 shows that for this specific configuration, a low field strength, medium field thickness or medium field strength, medium field thickness design results in the lowest system mass, depending on the exposure value desired. For example, consider a design for a one year mission, with a point dose equivalent value of 150 mSv considered as an acceptable exposure design baseline, and no other restrictions other than minimizing system mass. Based on these criteria, according to Figure 6.2, the optimal selection is approximately a 4.5T, 4.5m design, resulting in a system mass of

approximately 300 t. This translates into approximately 4.5 SLS launches to place this system mass in LEO.

6.2.3 Analysis Results: Magnetic Field "On" vs "Off" Case

It is useful to compare the effects of the active shield to the effects of the bulk material required to generate the magnetic field. To provide this comparison, the above case was analyzed with the magnetic field turned off, i.e. the equivalent system with no magnetic field effects. These results are shown below in Figures 6.3 and 6.4.

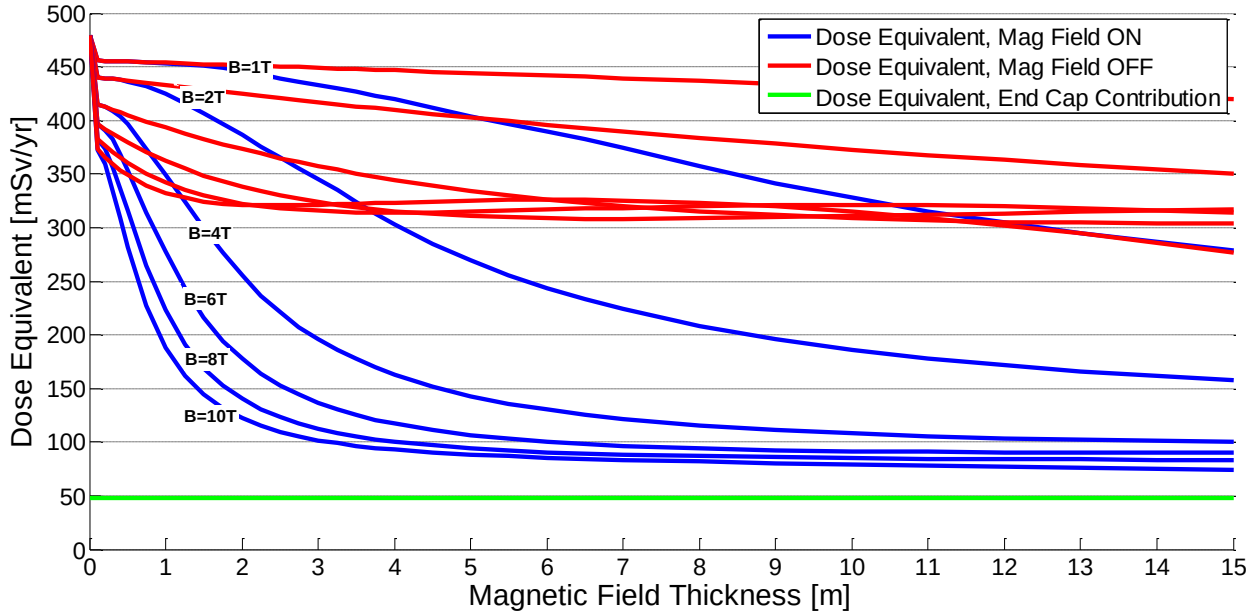

Figure 6.3 Annual Dose Equivalent for Fixed Field Strengths (B)

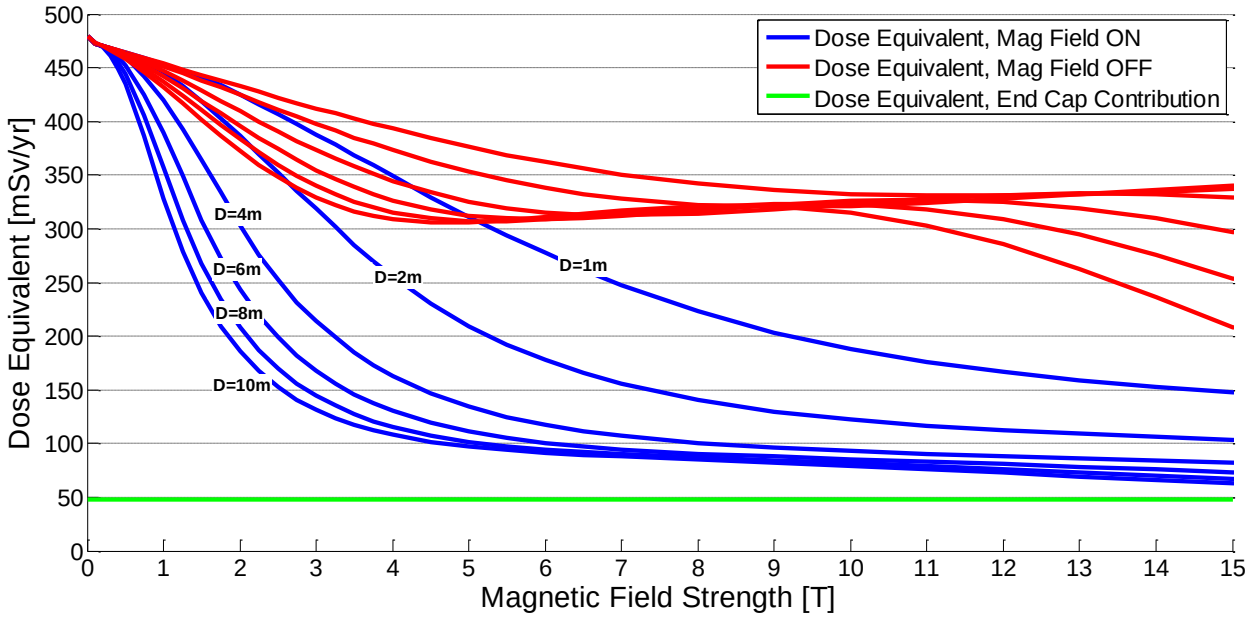

Figure 6.4 Annual Dose Equivalent for Fixed Field Thicknesses (D)

Figures 6.3 and 6.4 demonstrate that the magnetic shield offers a substantial reduction of the received dose equivalent, particularly at higher shield bending powers; however, these results compare the same quality, as well as quantity, of mass. The same quantities of material with better passive shielding properties, such as polyethylene, could provide a mass advantage. Future trade studies should be conducted on this topic, and these results could be used to identify technology drivers and priorities for active shielding development.

These plots also offer some additional insights into a solenoid active shielding design. As either field strength or field thickness is increased, the resulting dose equivalent approaches a horizontal asymptote, and bending powers greater than ~20 Tm begin to have a limited impact on further reducing dose equivalent values. This limiting value is dictated by two factors: the end-cap region and the shield's "side wall" region, where incoming particles do not pass through the entire thickness of the magnetic field. For example, a shield design with a small field thickness has a correspondingly small side-wall region. Thus, as the magnetic field strength is

increased, the asymptotic dose equivalent limit is only slightly higher than the contribution from the end-cap region. Shields with a large field thickness will have large side walls; therefore, the resulting dose equivalent contribution from this region will be larger and the asymptotic dose equivalent limit will be substantially higher than the contribution from the end-cap region.

Figures 6.3 and 6.4 also demonstrate an unexpected trend in the dose equivalent values for the "off" case at high bending powers. At these high bending powers, as either field strength or field thickness increases, the dose equivalent results increase slightly before dropping again. This is a result of the particle transport code and the large quantities of passive shielding that the flux is being transported through. For example, the dose equivalent results and passive shielding component thicknesses are shown in Figure 6.5 for a 6 m field thickness and varying field strength.

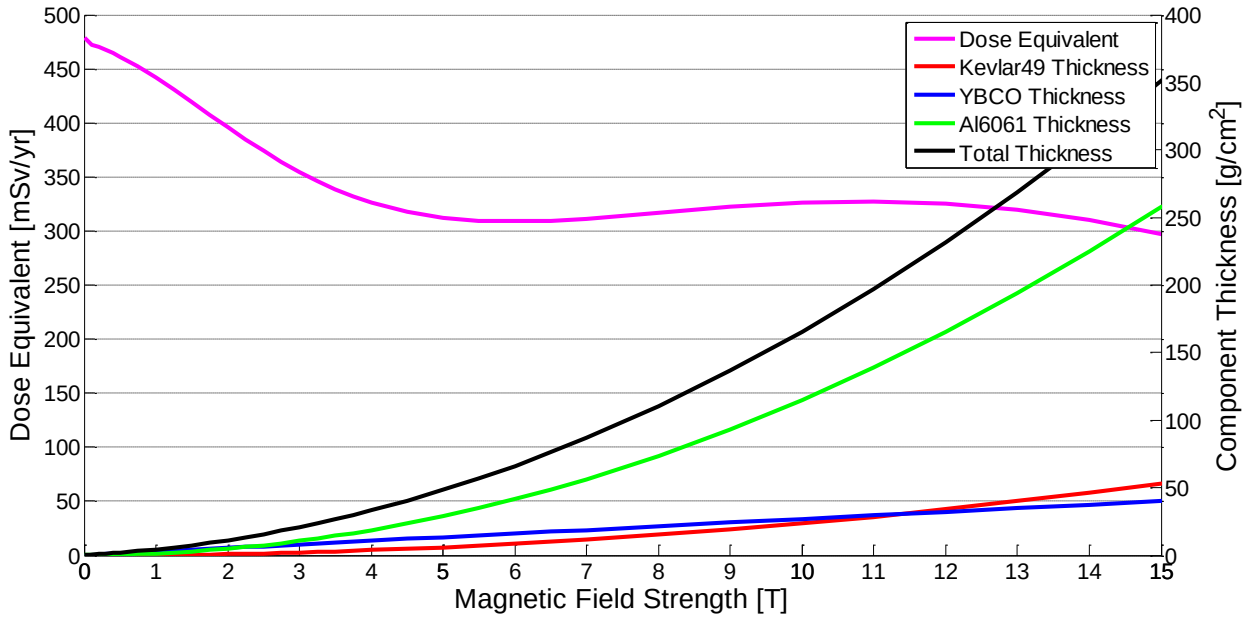

Figure 6.5 Annual Dose Equivalent and Shielding Component Thickness
For an Active Shield Thickness of 6m with the Magnetic Field "Off"

Figure 6.5 demonstrates that, for high bending powers, the radiation is being transported through large quantities of passive shielding. At these large passive shielding depths, large

uncertainties may be introduced, and these have not yet been quantified for depths greater than 100 g/cm^2 (Slaba et al., 2010a). However, the results of Figures 6.3 and 6.4 are consistent with the HZETRN output for large passive shielding depths, as demonstrated in Figure 6.6 for large depths of aluminum shielding.

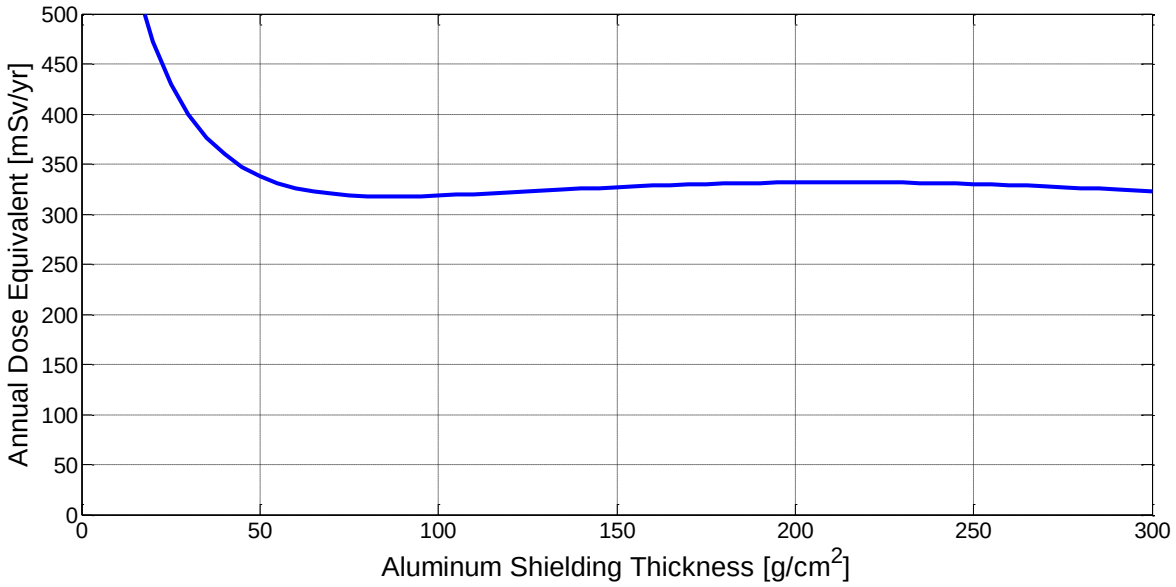

Figure 6.6 Annual Dose Equivalent vs Aluminum Shielding Depth
for 1977 Solar Minimum GCR Flux

6.3 Comparison with Monte Carlo Results

Unfortunately, there are few active magnetic shielding analyses with which to make a comparison of the rapid analysis model presented in this work. The best available comparison is the solenoid magnetic field design proposed by Westover et al. (2012), in the recent NIAC active magnetic shielding study, which was analyzed using Monte Carlo methods (Burger et al., 2013). This design uses a series of six 1T x 8m diameter coils, arranged around a cylindrical habitat, plus a "compensation coil" This geometry is shown in Figure 6.7. Unlike the rapid analysis model, the NIAC model assumes that the magnetic field is confined to the six solenoid coils. The

Monte Carlo analysis performed by the NIAC team utilized the GEANT3 toolkit (CERN, 1994), a predecessor to GEANT4, to determine the exposure results inside this shield.

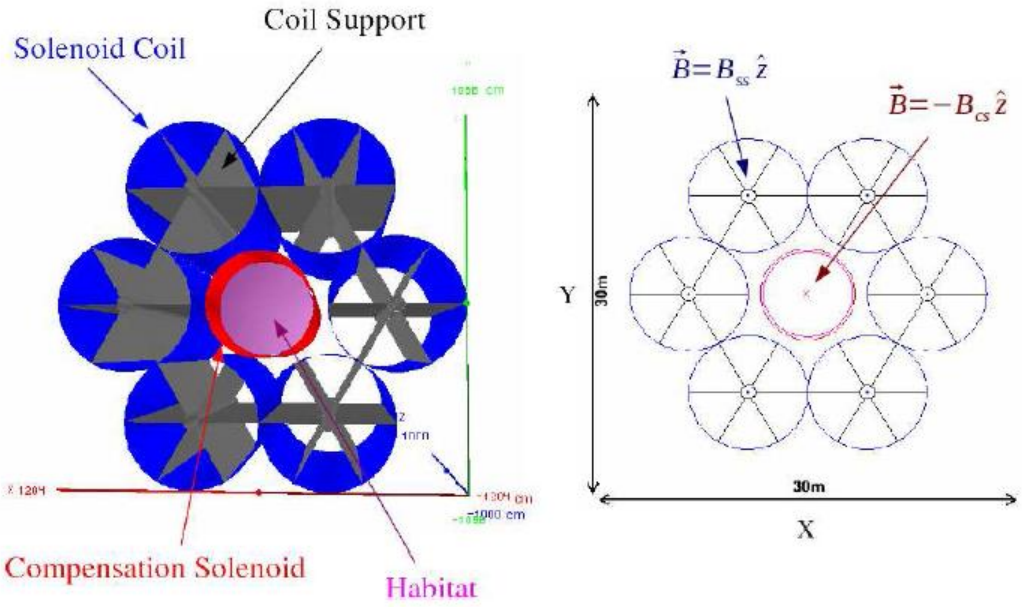

Figure 6.7 Monte Carlo Analysis Geometry (Westover et al., 2012)

In order to make a comparison between these two models, the rapid analysis model was modified to run using the same CREME09 1977 solar minimum GCR flux as the Monte-Carlo analysis. Additionally, the Monte Carlo results are given in terms of skin and BFO dose equivalent values, calculated using a 24 cm diameter x 180 cm long water cylinder at depths of 0 cm and 5 cm respectively. In order to enable a comparison, this capability was also added to the rapid analysis model by approximating skin and BFO dose equivalent values in a 24 cm diameter water sphere at depths of 0 cm and 5 cm respectively.

Initially the "free-space" dose equivalent values, i.e. no active or passive shielding, were compared. This allows differences from the dose equivalent determination methods and flux source configurations, using the same GCR model, to be determined. These results are shown in Table 6.1. The rapid analysis model yields lower exposure values; however, these are within

22% of the Monte-Carlo results, which is not unexpected for different radiation exposure model types (Heinbockel et al., 2011; Lin et al., 2012).

Table 6.1 "Free-Space" Model Comparison (CREME09 1977 Solar Minimum GCR flux)

DE Type	Rapid Analysis Model [mSv/yr]	Monte-Carlo Model [mSv/yr]	Delta [mSv/yr] (%)
Point DE	1320		
Skin DE	921	1177	256 (22%)
BFO DE	521	624	103 (17%)

Since the "free-space" analysis yielded comparable results, the same mass and material estimates from the NIAC study were placed into the rapid analysis model, as described in Section 6.1. The NIAC study utilized copper to approximate the superconductor material and graphite to represent the structural material. The total masses of these materials, 3,400 kg of copper and 21,038 kg of graphite, were smeared over the representative active shielding cylinder as shown in Figure 6.1. Additionally, an identical thickness of aluminum, 1.8 cm, was used to represent the habitat. The resulting values for both models are shown in Table 6.2.

Table 6.2 Shielding Model Comparison, 1T x 8m (CREME09 1977 Solar Minimum GCR flux)

DE Type	Rapid Analysis Model [mSv/yr]	Monte-Carlo Model [mSv/yr]	Delta [mSv/yr] (%)
Point DE	572		
Skin DE	463	604	141 (23%)
BFO DE	361	403	42 (10%)

Again, the rapid analysis model yields lower results, within 23% of the Monte-Carlo values, which is expected. This is due not only to the "free-space" comparison, but also due to differences in the magnetic field model. The NIAC model assumes that the magnetic field is confined to the solenoid coils, while the rapid analysis model assumes a uniform cylindrical field. Therefore, the rapid analysis model does not have the field gaps between the coils, which

allow higher energy particles to penetrate these regions in the NIAC model. Given the modeling differences, particularly the dose equivalent determination method and flux source configuration differences highlighted by the "free-space" results, the agreement between these two modeling results is reasonable.

Despite the efforts to make the rapid analysis model as similar as possible to the NIAC model, the following differences remain between the two:

1. Mass Location:
    a. Rapid Analysis model: smears equivalent mass over a representative cylinder
    b. Monte Carlo model: utilizes a more realistic geometry
2. Magnetic Field Geometry:
    a. Rapid Analysis model: assumes a uniform cylindrical field around the habitat (i.e. no gaps in the field)
    b. Monte-Carlo model: assumes that the field is confined to individual solenoid coils which surround the habitat (i.e. gaps in the field exist between coils)
3. Dose Equivalent Determination Method:
    a. Analytical-HZETRN model: 24 cm diameter water sphere
    b. Monte-Carlo model: 24 cm diameter x 180 cm long water cylinder
4. Flux Source Configuration : although the same GCR flux model is used, the CREME09 1977 Solar Minimum, the flux values are represented differently in the two models.
    a. Analytical-HZETRN: isotropic
    b. Monte-Carlo: flux generated uniformly over a cube surface 5 meters away from the architecture to approximate an isotropic source (results in flux biasing in the cube corners)

Future work should focus on eliminating these differences so that a better comparison can be made. This would also allow the assumptions that are made in the rapid analysis model to be quantified.

6.4 Chapter Summary

Applying the mass and material estimates from Chapter 5, to the rapid analysis model from Chapter 4, results in a robust analysis method. This allows an active shielding design trade space to be explored over a large range of magnetic field thicknesses with automatically adjusted mass and material properties. The modeling results allow a more specific design regime to be selected based on a variety of considerations, including the overall system mass. This analysis tool would also enable sensitivity studies to be conducted to determine how exposure results and mass estimates are affected by various design choices, such as structural material selection or superconductor types.

The analysis results for the general design case highlight some of the features of such an active shield design. These results demonstrate that the active component of the shielding system can provide significant exposure reductions, particularly at higher shield bending powers; however, bending powers greater than ~20 Tm begin to have a limited impact on further reducing dose equivalent values. Additionally, as either field strength or field thickness is increased, the resulting dose equivalent approaches a limit, dictated by the characteristics of the shield's end-cap and side wall regions. A shield design with a small field thickness has a correspondingly small side-wall region; therefore, as the magnetic field strength is increased, the dose equivalent limit is only slightly higher than the contribution from the end-cap region. Shields with a large field thickness will have large side walls, and the resulting dose equivalent

contribution from this region will be higher, resulting in a dose equivalent limit that is substantially larger than the contribution from the end-cap region.

The analysis model was also compared to a similar design that was analyzed using Monte Carlo techniques. These comparison results show reasonable agreement, given the differences which exist between the models. Future work should be conducted to eliminate these modeling differences so that a better comparison can be made. This would also allow the assumptions that are made in the rapid analysis model to be quantified.

Chapter 7

Summary and Conclusions

7.1 Summary

A method for rapidly analyzing an active magnetic shielding design was presented. This method utilizes an electromagnetic analytic solution method for determining the GCR flux inside the active shield as a result of the magnetic field. The resulting flux is then transported through a representative thickness of mass using the HZETRN2010 particle transport code, allowing the determination of mass and passive/structural shielding effects on the incident flux. This rapid analysis method enables the analysis of a large range of the two primary design variables: magnetic field strength and magnetic field thickness. Although this model was developed for a solenoid active shielding design, the methodology may also be applied to a toroidal design case.

Initial results were produced using a representative volume of aluminum; however, mass quality and quantity can affect the radiation exposure inside the shield design. In order determine appropriate mass properties, a survey was conducted of the major systems required for an active shielding design. A trade study of the major design options was presented, which allowed a narrowing in scope of possible system solutions. From this, mass and material estimates were formulated as a function of magnetic field strength and field thickness. In addition to providing mass and material estimates for use in the rapid analysis model, the analysis of the major active

shielding systems allowed the identification of several key technologies that should be prioritized for active shielding development.

The mass estimates developed were then incorporated into the rapid analysis model, so that the system mass could be automatically adjusted as a function of magnetic field strength and field thickness, and results were presented for a likely design case. This allowed the demonstration of how mass and material compositions of an actual shield design would affect the resulting radiation exposure and how these would change as a function of the system design variables. Finally, the model was compared to a similar design in which radiation exposure results were obtained using Monte Carlo analysis methods.

7.2 Conclusions

The simplicity of the analytical model combined with the computational speed of HZETRN allows the rapid determination of dose equivalent values for a large trade space of variables. By providing a broad analysis of magnetic field strength and magnetic field thickness, the results obtained allow designers to select configurations suited to specific mission goals, including mission radiation exposure limits, duration, and destination. Based on the trade study results generated in the initial model analysis, where only aluminum is used to represent the passive/structural shielding mass (Chapter 4), several characteristics of an active solenoid magnetic shield design were determined. These results showed that active shield bending powers greater than ~20 Tm and passive/structural shielding thicknesses greater than 40 g/cm^2 have a limited impact on further reducing dose equivalent values. Passive/structural shielding has a greater impact at lower bending powers; however, it still has a definite impact even at high bending powers due to the shielding it provides in the end-cap regions where the magnetic field

does not attenuate the incoming GCR flux. Additionally, for a given active shield bending power, magnetic field strength is more effective at reducing dose equivalent than field thickness.

The additional of mass and material estimates for a solenoid active shielding design allowed a more robust trade space analysis, with mass parameters automatically adjusted as functions of these design variables. The results generated allowed insight not only into the effectiveness of reducing radiation exposure, but also the overall mass requirements of such a design. These radiation exposure results were generally consistent with those of the aluminum only case, i.e. bending powers greater than ~20 Tm have a limited impact on further reducing dose equivalent values and magnetic field strength is more effective at reducing dose equivalent than field thickness. However, when combined with the overall system mass results, high field strength, low field thickness designs may be less desirable since they can have higher overall system mass quantities than low field strength, high field thickness or medium strength, medium thickness designs. Additionally, as either field strength or field thickness is increased, the resulting dose equivalent approaches a limit that is dictated by the characteristics of the shield's end-cap and side wall regions. When compared with available Monte Carlo results, the rapid analysis results also show that these models are in reasonable agreement, given the differences that still remain between the modeling types.

Finally the survey and trade study analysis of the systems required for an active magnetic shield design resulted into a down selection of possible system architectures:

1. Magnetic/Superconductor System: HTS superconductor such as YBCO tape or BSCCO wire.
2. Structural System: mixed material design with high-strength, light-weight options such as Kevlar or Zylon used for radial support.

3. Thermal System: cryocirculator system (although a wet, closed-loop system could be employed at a higher mass penalty is greater quench protection is needed).
4. Superconductor Power System: transformer rectifier flux pumps.

This also allowed the identification of the following key technologies which are either enabling for such a design or would provide significant mass or performance improvements:

1. Metallurgical and manufacturing improvements to increase the critical current density of existing superconductor material.
2. Metallurgical and manufacturing improvements to increase the engineering current density of existing superconductor materials.
3. Manufacturing improvements to increase the maximum achievable length of superconductor wires and tapes.
4. Development of improved superconductor splice technology.
5. Development of new, higher temperature superconductors.
6. Development of higher-strength, lighter-weight structural materials.
7. Development of space qualified, high capacity cryocoolers.
8. Improvements in cryocooler efficiency.
9. Development of high current, transformer rectifier HTS flux pumps.

7.3 Future Work

In order to simplify the analysis and reduce the required computation time, four primary assumptions are made in the rapid analysis model: the magnetic field is uniform in magnitude, the magnetic field is confined to the boundaries of a cylindrical geometry, all of the mass is confined in the interior of the magnetic field, and this mass is represented by an appropriate

volume of spherical shielding. Future work concerning this model should focus on quantifying the effects of these assumptions. This is probably best accomplished by creating a Monte Carlo analysis model that can be directly compared to the rapid analysis model results. Although an initial comparison with the NIAC study Monte Carlo results demonstrated reasonable agreement, there are numerous modeling differences that exist between the two. By creating a Monte Carlo model allowing direct comparison, the rapid analysis model can be better qualified and improved.

There are also numerous improvements that can be made to the rapid analysis model, and these will likely be further identified as better Monte Carlo comparisons become available. One aspect that would significantly enable the utility of this model is the addition of human phantom models. Currently, the rapid analysis model calculates radiation exposure as a point dose equivalent value. While this allows the efficacy of various shielding designs to be compared, it does not allow for the direct comparison to equivalent dose or organ dose values. These provide a better characterization of the biological effects of radiation and allow a relation to future exposure limits. Therefore, a priority for future work should be the incorporation of human phantom models, such as MAX/FAX models (Kramer et al., 2003; Kramer et al., 2004).

Finally, the rapid analysis model can enable the analysis of a broad range of variables beyond magnetic field strength and field thickness. This could include a variety of active shielding design parameters such as superconductor type, superconductor J_e values, support structure material, etc. Therefore, additional future work could focus on utilizing the rapid analysis model to perform trade and sensitivity studies of these design parameters. This would allow better determination of active shielding design options, as well as help prioritize technology improvements for active shielding.

References

Adams, J.H., Hathaway, D.H., Gregory, J.C. Grugel, R.N., Parnell, T.A., Watts, J.W., Winglee, R.M. Revolutionary Concepts of Radiation Shielding for Human Exploration of Space. NASA TM 213688, 2005.

Agostinelli, S., Allison, J., Amako, K., et al. GEANT4 - a simulation toolkit. Nucl. Instr. Meth. A 506, pp. 250–303, 2003.

Badhwar, G.D., Cucinotta, F.A., O'Neill, P.M. An analysis of interplanetary space radiation exposure for various solar cycles. Radiation Research 138 (2), pp. 201-208, 1994.

Bailey, S., Raffaelle, R. Handbook of Photovoltaic Science and Engineering, Chapter 9: Space Solar Cells and Arrays, second ed. Luque, A. and Hegedus, S., Eds. John Wiley & Sons, Ltd, 2011.

Battistoni, G., Muraro, S., Sala, P.R., Cerutti, F., Ferrari, A., Roesler, S., Fassò, A., Ranft, J. The FLUKA code: Description and benchmarking. Proceedings of the Hadronic Shower Simulation Workshop 2006, Fermilab 6-8 September 2006. M. Albrow, R. Raja eds., AIP Conference Proceeding 896, pp. 31-49, 2007.

Battiston, R. Burger, W.J., Calvelli, V., Musenich, R., Choutko, V., Datskov, V.I., A. Della Torre, A.D., Venditti, F., Gargiulo, C., Laurenti, G., Lucidi, S., Harrison, S., Meinke, R. ARSSEM: Active Radiation Shielding for Space Exploration Missions. Final Report ESTEC Contract No. 4200023087/10/NL/AF, 2011.

Billings, M.P., Yucker, W.R. The Computerized Anatomical Man (CAM) Model. NASA Contractor Report CR-134043, 1973.

Brown, C.D. Elements of Spacecraft Design. AIAA Inc., Reston, VA, 2002.

Buckley, J.C. Space Physiology. Oxford University Press, Inc., New York, 2006.

Burger, W.J., Battiston, R., Calvelli, V., Musenich, R., Datskov, V.I., Della Torre, A., Venditti, F., Hovland, S., Meinke, R., Van Sciver, S., Westover, S.C., Washburn, S.A. Active magnetic shielding for long duration manned space missions. 6th IAASS International Space Safety Conference, Montreal, Canada, 21-23 May 2013.

Cengel. Y.A., Boles, M.A. Thermodynamics: an Engineering Approach, third ed. McGraw-Hill, Boston, 1998.

CERN. GEANT - Detector Description and Simulator Tool, CERN Program Library Long Write-up W5013, CERN, Geneva, 1994.

Chung, C.H., Fopp, S., Kirn, T.H., et al., AMS on ISS: application of particle physics technology to manned interplanetary flight, AMS Collaboration Internal Report. March 2005, in preparation.

Clowdsley, M.S. Wilson, J.W., Kim, M., Anderson, B.M., Nealy, J.E. Radiation protection quantities for near Earth environments. AIAA Space 2004 Conference and Exhibit, San Diego, CA, 2004.

Cocks, F. Hadley. A deployable high temperature superconducting coil (DHTSC): A novel concept for producing magnetic shields against both solar flare and galactic radiation during manned interplanetary missions. J. Br. Interplanet. Soc 44, pp. 99 – 102, 1991.

Cucinotta., F.A., Nikjoo, H., Goodhead, D.T. Comment on the effects of delta-rays on the number of particle-track transversals per cell in laboratory and space exposures. Radiat. Res., 150, pp. 115–119, 1998.

Cucinotta, F.A., Manuel, F. K., Jones, J., Iszard, G., Murrey, J., Djojonegro, B., Wear, M. Space radiation and cataracts in astronauts. Rad. Res. 156, pp. 460–466, 2001.

Cucinotta, F.A., Durante, M. Cancer risk from exposure to galactic cosmic rays: implications for space exploration by human beings. Lancet Oncol. 7, pp. 431–435, 2006.

Cucinotta, F.A., Kim, M.H., Willingham, V., George, K.A. Physical and biological organ dosimetry analysis for International Space Station astronauts. Radiation Research 170, pp. 127–138, 2008.

Cucinotta, F.A., Durante, M. Risk of Radiation Carcinogenesis. Chapter 4 in Human Health and Performance Risks of Space Exploration Missions, Mcphee, J.C and Charles, J.B., Eds. NASA SP-2009-3405, 2009.

Cucinotta, F.A., Wang, H., Huff, J. Risk of Acute or Late Central Nervous System Effects from Radiation Exposure. Chapter 6 in Human Health and Performance Risks of Space Exploration Missions, Mcphee, J.C and Charles, J.B., Eds. NASA SP-2009-3405, 2009.

Cucinotta, F.A., Kim, M.Y., Chappell, L.J. Space Radiation Cancer Risk Projections and Uncertainties – 2010. NASA/TP-2011- 216155, July, 2011.

Cucinotta, F.A., Kim, M.Y., Chappell, L.J. Space Radiation Cancer Risk Projections and Uncertainties – 2012. NASA/TP-2013-217375, January, 2013.

Cyrot, M., Pavuna, D. Introduction to Superconductivity and High-T_C Materials. World Scientific Publishing Co., New Jersy, 1992.

Durante, M., Cucinotta, F.A. Physical basis of radiation protection in space travel. Rev. Mod. Phys. 83 (4), pp. 1245-1281, 2011.

Fassò , A., Ferrari, A., Ranft, J., Sala, P.R. FLUKA: a Multi-Particle Transport Code. CERN-2005-10, 2005, INFN/TC_05/11, SLAC-R-773, 2005.

Griffiths, D.J. Introduction to Electrodynamics, third ed. Prentice Hall, New Jersey, 1999.

Hall, E.J., Cox, J.D, Physical and Biologic Basis of Radiation Therapy, in Moss's Radiation Oncology, Cox, J.D., Ed. Mosby, St. Louis, MO, 1994.

Haugan, T.J., Baca, F.J., Mullins, M.J. Pierce, N.A., Campbell, T.A., Brewster, E.L., Barnes, P.N. Wang, H., Sumption, M.D. Temperature and magnetic field dependence of critical current density of YBCO with varying flux pinning additions. IEEE Trans. Appl. Supercond. 19 (3), pp. 3270 – 3274, 2009.

Hazelton, D.W. 2G HTS Conductors at SuperPower. Low Temperature High Field Superconductor Workshop (LTHFSW2012), Napa, CA, November 6, 2012.

Heinbockel, J.H., Slaba, T.C., Tripathi, R.K., Blattnig, S.R., Norbury, J.W., Badavi, F.F., Townsend, L.W., Handler, T., Gabriel, T.A., Pinsky, L.S., Reddell, B., Aumann, A.R. Comparison of the transport codes HZETRN, HETC and FLUKA for galactic cosmic rays. Adv. Space Res. 47, pp. 1089–1105, 2011.

Heinemann, W. Design Mass Properties II: Mass Estimating and Forecasting for Aerospace Vehicles Based on Historical Data. NASA JSC-26098, 1994.

Hoffman, J.A., Fisher, P., Batishchev, O. Use of Superconducting Magnet Technology for Astronaut Radiation Protection. NASA NIAC Phase I Final Report, 2005.

Huff, J.L., Cucinotta, F.A. Risk of Degenerative Tissue or Other Health Effects from Radiation Exposure. Chapter 7 in Human Health and Performance Risks of Space Exploration Missions, Mcphee, J.C and Charles, J.B., Eds., NASA SP-2009-3405, 2009.

International Commission on Radiological Protection. 1990 Recommendations of the International Commission on Radiological Protection. ICRP Publication 60. Ann. ICRP 21 (1-3), 1991.

International Commission on Radiological Protection. The 2007 Recommendations of the International Commission on Radiological Protection. ICRP Publication 103. Ann. ICRP 37 (2-4), 2007.

International Commission on Radiological Units and Measurements. Fundamental Units and Quantities for Ionizing Radiation (Revised). J. ICRU 11 (1), 2011.

Iwase, H., Niita, K., Nakamura, T. Development of general-purpose particle and heavy ion transport Monte Carlo code. J. Nucl. Sci. Tech. 39 (11), pp. 1142–1151, 2002.

Iwasa, Y. Case Studies in Superconducting Magnets: Design and Operational Issues, second edition. Springer, Cambridge, MA, 2009.

James, M.R., McKinney, G.W., Durkee, J.W. et al. MCNPX 2.7.X – New features being developed. IEEE/NSS Conference, Orlando, FL, October 25–31, 2009.

Kervendal, E.A., Kirk, D.R., Meinke, R.B. Spacecraft radiation shielding using ultralightweight superconducting magnets. Journal of Spacecraft and Rockets, Vol. 46 (5), pp. 982 – 988, 2009.

Kittel, P. Cryocooler Performance Estimator. Miller,S.D. and R.G. Ross, R.G. Eds. International Cryocooler Conference, Inc., Boulder, CO, 2007.

Kramer, R., Vieira, J.W., Khoury, H.J., Lima, F.R.A., Fuelle, D. All about MAX: a male adult voxel phantom for Monte Carlo calculations in radiation protection dosimetry. Phys. Med. Biol. 48, pp. 1239–1262, 2003.

Kramer, R., Vieira, J.W., Khoury, H.J., Lima, F.R.A., Loureiro, E.C.M., Lima, V.J.M., Hoff, G. All about FAX: a female adult voxel phantom for Monte Carlo calculations in radiation protection dosimetry. Phys. Med. Biol. 49, pp. 5203–5216, 2004.

Kumada, M., Fujisawa, T., Hirao, Y., Endo, M., Aoki, M., Kohda, T., Bolshakova, I., Holyaka. R. Development of 4 Tesla permanent magnet. Proceedings of the IEEE 2001 Particle Accelerator Conference, Chicago, 2001.

Levy, R. H., Janes, G. S. Plasma radiation shielding. AIAA Journal 2, pp. 1835-1838, 1964.

Lin, Z.W., Adams, J.H., Barghouty, A.F., Randeniya, S.D., Tripathi, R.K., Watts, J.W., Yepes, P.P. Comparisons of several transport models in their predictions in typical space radiation environments. Adv. Space Res. 49 (4), pp. 797–806, 2012.

Lockheed Martin Corporation website: Heat Rejection Radiators (HRS). Retrieved May 23, 2013, from http://www.lockheedmartin.com/us/products/HeatRejectionRadiators.html.

Lombardo, V., Barzi, E., Turrioni, D., Zlobin, A.V. Critical currents of $YBa_2Cu_3O_{7-\delta}$ tapes and $Bi_2Sr_2CaCu_2O_x$ wires at different temperatures and magnetic fields. IEEE Trans. Appl. Supercond. 21, pp. 3247-3250, 2011.

Mulder, G.B.J., ten Kate, H.H.J., Krooshoop, H.J.G., van de Klundert, L.J.M. Development of a thermally switched superconducting rectifier for 100 kA. IEEE Trans. on Magnetics 27 (2), pp. 2333 – 2336, 1991.

Mrigakshi, A.I., Matthiä, D., Berger, T., Reitz, G., and Wimmer-Schweingruber, R.F. Assessment of galactic cosmic ray models, J. Geophys. Res., 117, doi: 10.1029/2012JA017611, 2012.

National Aeronautics and Space Administration website: NIAC page. Retrieved June 15, 2013, from http://www.nasa.gov/directorates/spacetech/niac/2012_phaseII_fellows_westover.html.

National Aeronautics and Space Administration. NASA Space Flight Human System Standard Volume 1: Crew Health. NASA-STD-3001. March, 2007.

National Aeronautics and Space Administration. Human Integration Design Handbook (HIDH). NASA/SP-2010-3407. January, 2010.

National Aeronautics and Space Administration. NASA Space Flight Human System Standard Volume 2: Human Factors, Habitability, And Environmental Health. NASA-STD-3001. January, 2011.

National Aeronautics and Space Administration. Human Health, Life Support and Habitation Systems, Technology Area 06. Internet Publication (www.nasa.gov/offices/oct/home/roadmaps). April, 2012.

National Aeronautics and Space Administration website, SLS Fact Sheet. Retrieved May 23, 2013, from http://www.nasa.gov/exploration/systems/sls.

National Council on Radiation Protection and Measurements, Guidance on Radiation Received in Space Activities, NCRP Report No. 98, National Council on Radiation Protection and Measurements, Bethesda, Maryland, 1989.

National Council on Radiation Protection and Measurements, Radiation Protection Guidance for Activities in Low-Earth Orbit, NCRP Report No. 132, National Council on Radiation Protection and Measurements, Bethesda, Maryland, 2000.

National Research Council. Radiation Hazards to Crews of Interplanetary Missions: Biological Issues and Research Strategies. The National Academies Press, Washington D.C., 1996.

National Research Council. Managing Space Radiation Risk in the New Era of Space Exploration. The National Academies Press, Washington D.C., 2008.

National Research Council. Radiation and the International Space Station: Recommendations to Reduce Risk. The National Academies Press, Washington D.C., 2010.

National Research Council. NASA Space Technology Roadmaps and Priorities: Restoring NASA's Technological Edge and Paving the Way for a New Era in Space. The National Academies Press, Washington D.C., 2012.

Olsen, R.C. Introduction to the Space Environment. Internet Publication (http://uk-corp.org), 2005.

O'Neill, P.M. Badhwar–O'Neill 2010 galactic cosmic ray flux model - revised. IEEE Trans. Nucl. Sci. 57 (6), pp. 3148–3153, 2010.

Parsons, J.L., Townsend, L.W. Interplanetary crew dose rates for the August 1972 solar particle event. Radiation Research 153, pp. 729–733, 2000.

Patel, V.N., Gupta, S., Shareef, M.M., Ahmed, M.M. Contemporary radiation countermeasures. Defense Science Journal 61 (2), pp. 138-145, 2011.

Radebaugh, R., Refrigeration for superconductors. Proceedings of the IEEE 92 (10), pp. 1719 – 1734, 2004.

Radebaugh, R., Cryocoolers: the state of the art and recent developments. J. Phys.: Condens. Matter 21, doi:10.1088/0953-8984/21/16/164219, 2009.

Reed, R.D., Coulter, G.R. Physiology of Spaceflight. Chapter 5 in Human Spaceflight Mission Analysis and Design. Larson, W.J., Pranke, L.K., Eds. McGraw Hill, New York, 2000.

Robbins, D.E., Yang, T.C. Radiation and Radiobiology. Chapter 9 in Space Physiology and Medicine, third edition. Nicogossian, A.E., Huntoon, C.L., Pool, S.L., Eds. Lea and Febiger, New York, 1994.

Ross, R.G., Boyle, R.F. An overview of NASA space cryocooler programs – 2006. International Cryocooler Conference Annapolis, MD, June 14-6, 2006.

Rucker, M.A., Thompson, S. Developing a habitat For long duration, deep space missions. AIAA Global Exploration 2012 Conference; Washington, D.C., May 22-24, 2012.

Saxena, A.K. High-Temperature Superconductors, second edition. Springer, New York, 2012.

Schoenfeld, M.P., Ansari, R.R., Nakao, A., Wink, D. A hypothesis on biological protection from space radiation through the use of new therapeutic gases as medical counter measures. Medical Gas Research 2 (1), doi: 10.1186/2045-9912-2-8, 2012.

Schwartz, J., Effio, T., Liu, X., Le, Q.V., Mbaruku, A.L., Schneider-Muntau, H.J., Shen, T. High field superconducting solenoids via high temperature superconductors. IEEE Trans. Appl. Supercond. 18 (2), pp. 70-81, 2008.

Severn Communications Corporation. UPROP a Heavy-Ion Propagation Code. SCC Report, pp. 89–102, 1989.

Simpson, J.A. Elemental and isotopic composition of the galactic cosmic rays. Ann. Re. Nucl. Part. Sci. 33, pp. 323 -382, 1983.

Singleterry, R.C. Radiation engineering analysis of shielding materials to assess their ability to protect astronauts in deep space from energetic particle radiation. Acta Astronautica 91, pp. 49–54, 2013.

Slaba, T.C., Blattnig, S.R., Badavi, F.F. Faster and more accurate transport procedures for HZETRN. J. of Comput. Phys. 229, pp. 9397-9417, 2010a.

Slaba, T.C., Blattnig, S.R., Aghara, S.K., Townsend, L.W., Handler, T., Gabriel, T.A., Pinsky, L.S., Reddell, B. Coupled neutron transport for HZETRN. Rad. Meas. 45 (2), pp. 173-182, 2010b.

Spillantini, P., Taccetti, F., Papini, P., Rossi, L. Radiation shielding of spacecraft in manned interplanetary flights. Nuclear Instruments and Methods in Physics Research 443 (2–3), pp. 254–263, 2000.

Spillantini, P. Active shielding for long duration interplanetary manned missions. Adv. Space Res. 45, pp. 900–916, 2010.

Spillantini, P. Superconducting magnets and mission strategies for protection from ionizing radiation in interplanetary manned missions and interplanetary habitats. Acta Astronautica 68, pp. 1430–1439, 2011.

Stabin, M.G. Radiation Protection and Dosimetry: An Introduction to Health Physics. Springer, New York, 2007.

Stimpson, L.D., Jaworski, W., Effects of overlaps, stitches, and patches on multilayer insulation. AIAA Seventh Thermophysics Conference, San Antonio, TX, April, 1972.

SuperPower Inc. website. 2G HTS Wire Specification Overview. Retrieved May 23, 2013, from http://www.superpower-inc.com/content/products-services.

Sussingham, J.C., Watkins, S.A., Cocks, F.H., Forty years of development of active systems for radiation protection of spacecraft. Journal of the Astronautical Sciences 47, pp. 165-175, 1999.

Townsend, L.W. Implications of the space radiation environment for human exploration in deep space. Rad. Prot. Dosim. 115 (1-4), pp. 44-50, 2005a.

Townsend, L.W. Critical analysis of active shielding methods for space radiation protection. Aerospace Conference, IEEE 2005, pp. 724-730, 5-12 March 2005b.

Townsend, L.W., Miller, T.M., Gabriel, T.A. HETC radiation transport code development for cosmic ray shielding applications in space. Rad. Prot. Dos. 116, pp. 135–139, 2005.

Tripathi, R.K., Wilson, J.W., Youngquist, R.C. Electrostatic active radiation shielding-revisited. IEEE Aerospace Conference, 2006.

Tripathi, R.K., Schaub, H.P, Joshi, R. Meeting the Grand Challenge of Protecting Astronaut's Health: Electrostatic Active Space Radiation Shielding for Deep Space Missions. NASA NIAC Phase I Final Report, 2011.

Trovati, S., Ballarini, F., Battistoni, G., Cerutti, F., Fassò, A., Ferrari, A., Gadioli, E., Garzelli, M.V., Mairani, A., Ottolenghi, A., Paretzke, H.G., Parini, V., Pelliccioni, M., Pinsky, L., Sala, P.R., Scannicchio, D., Zankl, M. Human exposure to space radiation: role of primary and secondary particles. Radiat Prot Dosimetry, 122 (1-4), pp. 362-366, 2006.

Turenne, M., Johnson, R.P., Hunte, F., Schwartz, J., Song, H. Roebel cable for high-field low-loss accelerator magnets. Proceedings of IPAC'10, Kyoto, Japan, 2010.

Turner, J.E. Atoms, Radiation, and Radiation Protection, second edition. John Wiley & Sons, Inc., New York, 1995.

van de Klundert, L.J.M., ten Kate, H.H.J. Fully superconducting rectifiers and fluxpumps Part 1: realized methods for pumping flux. Cryogenics 21 (4), pp. 195–206, April 1981a.

van de Klundert, L.J.M., ten Kate, H.H.J. On fully superconducting rectifiers and fluxpumps. A review. Part 2: commutation modes, characteristics, and switches. Cryogenics 21 (5), pp. 267–277, May 1981b.

van der Laan, D. C., Goodrich, L.F., Haugan, T.J. High-current dc power transmission in flexible RE–$Ba_2Cu_3O_{7-\delta}$ coated conductor cables. Superconductor Science and Technology 25 (1), doi:10.1088/0953-2048/25/1/014003, 2011.

Vogler, F.H., Analysis of an electrostatic shield for space vehicles. AIAA Journal Vol 2 (5), pp. 872 – 878, 1964.

von Braun, W. Will mighty magnets protect voyagers to planets? Popular Science, Vol. 194 (1), pp. 98-100, January, 1969.

de Waele, A.T.A.M. Basic operation of cryocoolers and related thermal machines. J Low Temp. Phys. 164, 179–236, 2011.

Westover, S.C., Meinke, R.B., Battiston, R., Burger, W.J., Van Sciver, S., Washburn, S.A., Blattnig, S.R., Bollweg, K., Singleterry, R.C., Winter, D.S. MAARSS - Magnet Architectures and Active Radiation Shielding Study with High Temperature Superconductors. NASA NIAC Phase I Final Report, 2012.

Weiss, J.F., Landauer, M.R. Radioprotection by antioxidants. Annals of the New York Academy of Sciences 899, pp. 44 – 60, 2000.

Wilson, J.W., Badavi, F.F., Cucinotta, F.A., Shinn, J.L., Badhwar, G.D., Silberberg, R., Tsao, C.H., Townsend, L.W., Tripathi, R.K. HZETRN: Description of a Free-Space Ion and Nucleon Transport and Shielding Computer Program, NASA Technical Paper 3495, 1995.

Wilson, J.W., Miller, J., Konradi, A., Cucinotta, F.A., Eds. Shielding Strategies for Human Space Exploration. NASA CP 3360, 1997.

Wilson, J.W., Tripathi, R.K., Mertens, C.J., Blattnig, S.R., Clowdsley, M.S., Cucinotta, F.A., Tweed, J., Heinbockel, J.H., Walker, S.A., Nealy, J.A. Verification and Validation: High Charge and Energy (HZE) Transport Codes and Future Development. NASA/TP-2005-213784, July, 2005.

Appendix A:

Rapid Analysis Model Flowchart, Infinite Cylinder

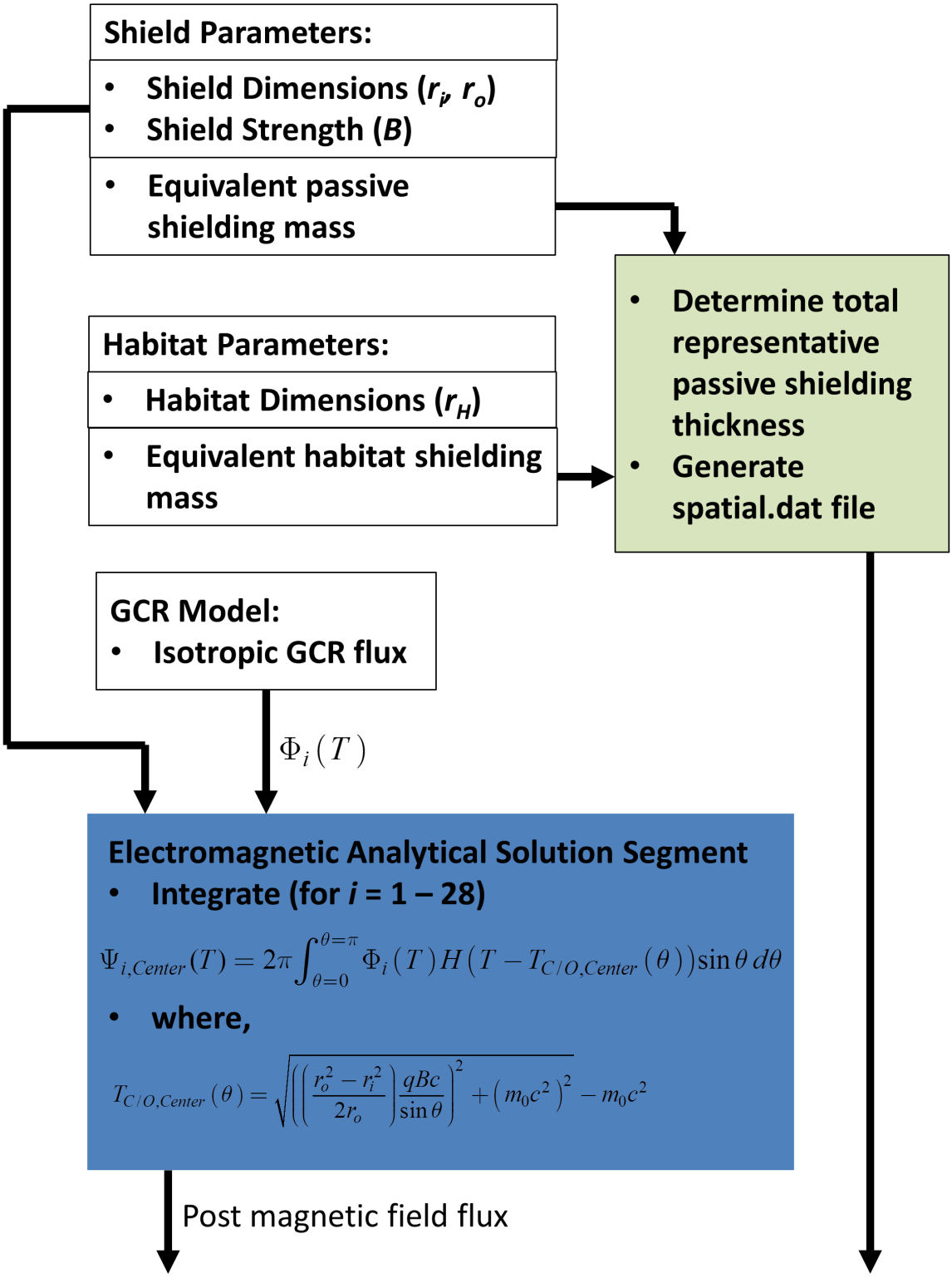

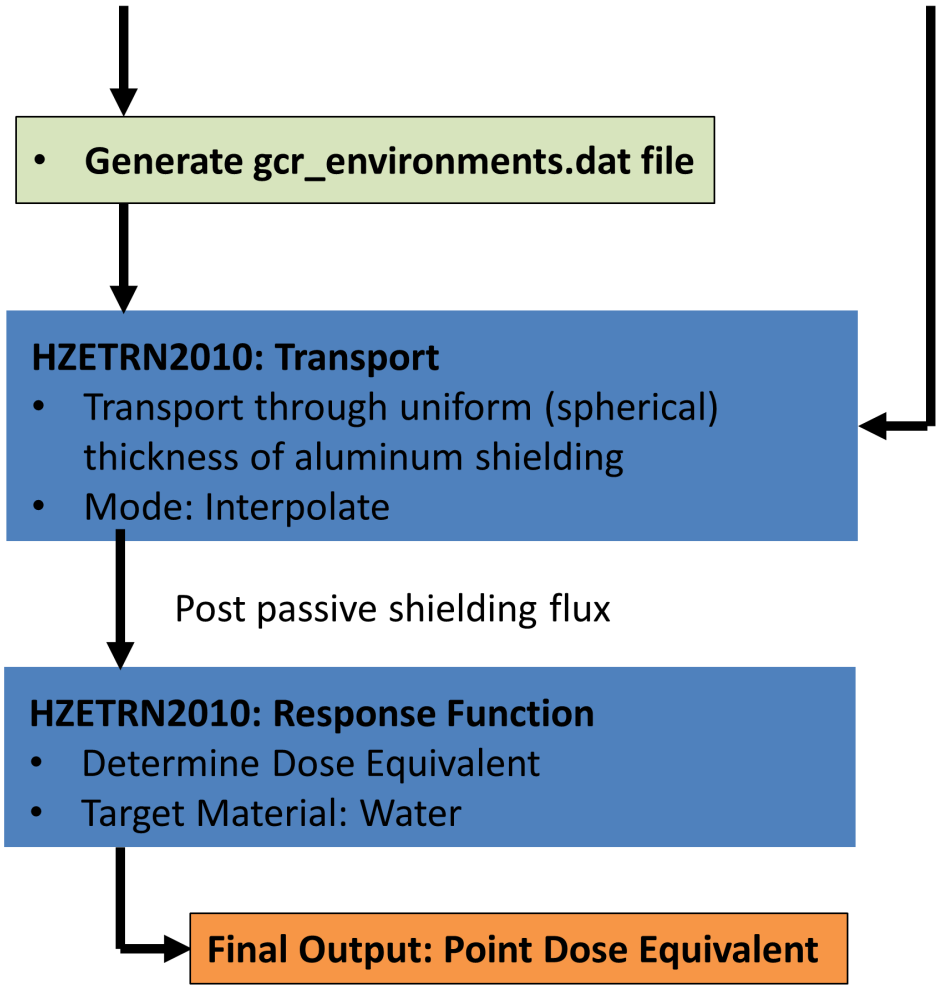

Appendix B:

Rapid Analysis Model Flowchart, Open-Ended Cylinder

Shield Parameters:

- Shield Dimensions (r_i, r_o, l)
- Shield Strength (B)
- Equivalent passive shielding mass

Habitat Parameters:

- Habitat Dimensions (r_H, L_H)
- Equivalent habitat shielding mass

Analysis Point:

- Distance from habitat center along axial centerline(L_P)

- Determine total representative passive shielding thickness
- Generate spatial.dat file

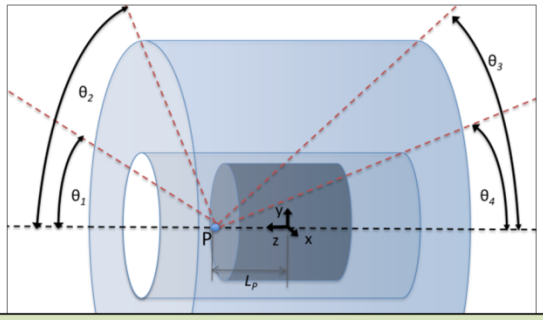

Determine Integration angles (θ_1, θ_2, θ_3, θ_4)

$$\theta_1 = \tan^{-1}\left(\frac{r_i}{(l/2)-L_P}\right) \qquad \theta_3 = \pi - \tan^{-1}\left(\frac{r_o}{(l/2)+L_P}\right)$$

$$\theta_2 = \tan^{-1}\left(\frac{r_o}{(l/2)-L_P}\right) \qquad \theta_4 = \pi - \tan^{-1}\left(\frac{r_i}{(l/2)+L_P}\right)$$

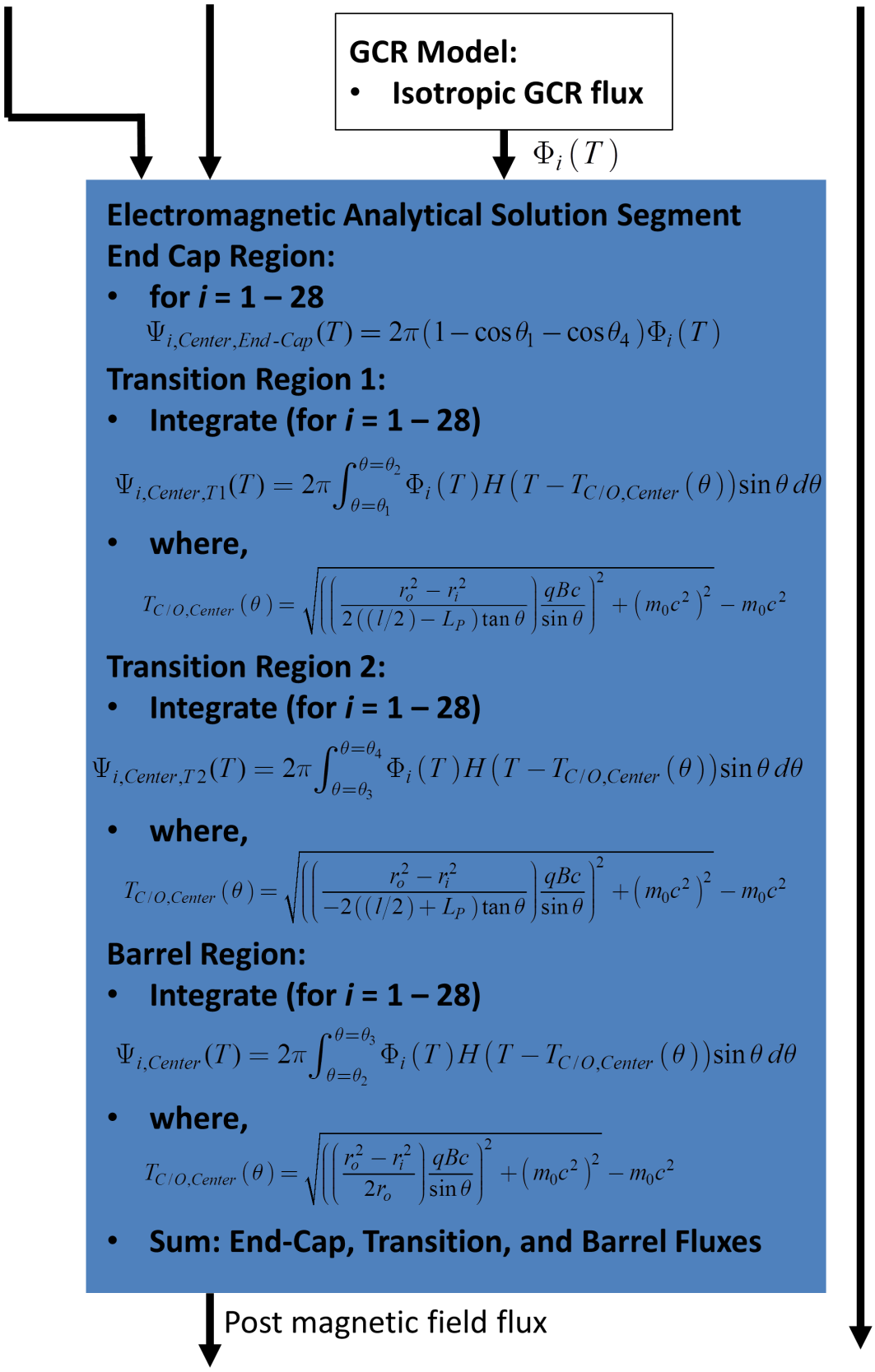

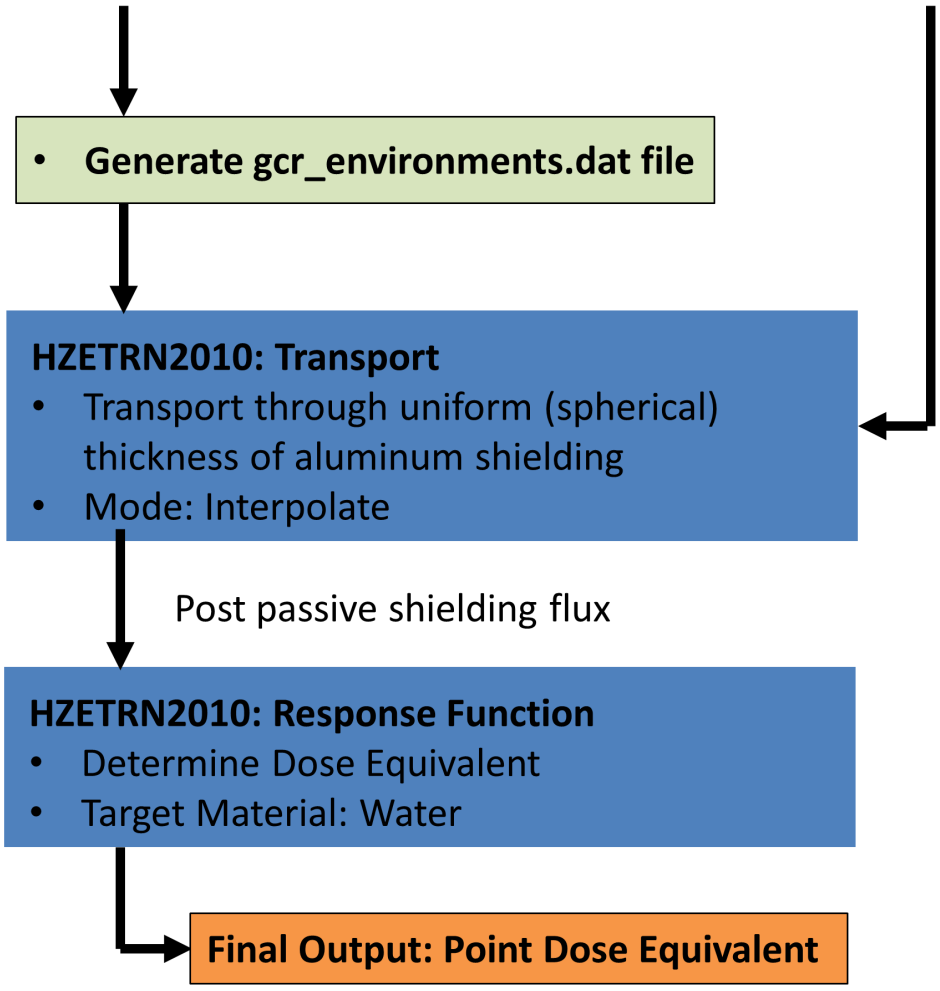

Appendix C:

Rapid Analysis Model Flowchart, Mass Adjusted Open-Ended Cylinder

Shield Parameters:

- Shield Dimensions (r_i, r_o, l)
- Shield Strength (B)
- Shield design properties (J_e, R_{splice}, F_S, etc.)

Habitat Parameters:

- Habitat Dimensions (r_H, L_H)
- Habitat Wall thickness
- Habitat End-Cap thickness

Analysis Point:

- Distance from habitat center along axial centerline(L_P)

- Determine total mass of each material type (M_j) - Appendix D
- Smear total mass over representative cylinder to determine average thickness (t_j)

$$t_j = \frac{M_j}{2\pi(r_i + D/2)l}$$

- Generate spatial_barrel.dat file

- Generate spatial_hab.dat file
- Generate spatial_endcap.dat file

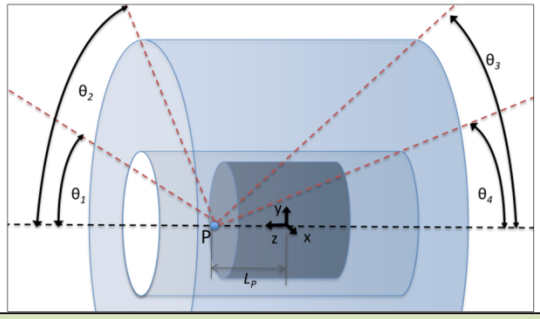

Determine Integration angles (θ_1, θ_2, θ_3, θ_4)

$$\theta_1 = \tan^{-1}\left(\frac{r_i}{(l/2) - L_P}\right) \qquad \theta_3 = \pi - \tan^{-1}\left(\frac{r_o}{(l/2) + L_P}\right)$$

$$\theta_2 = \tan^{-1}\left(\frac{r_o}{(l/2) - L_P}\right) \qquad \theta_4 = \pi - \tan^{-1}\left(\frac{r_i}{(l/2) + L_P}\right)$$

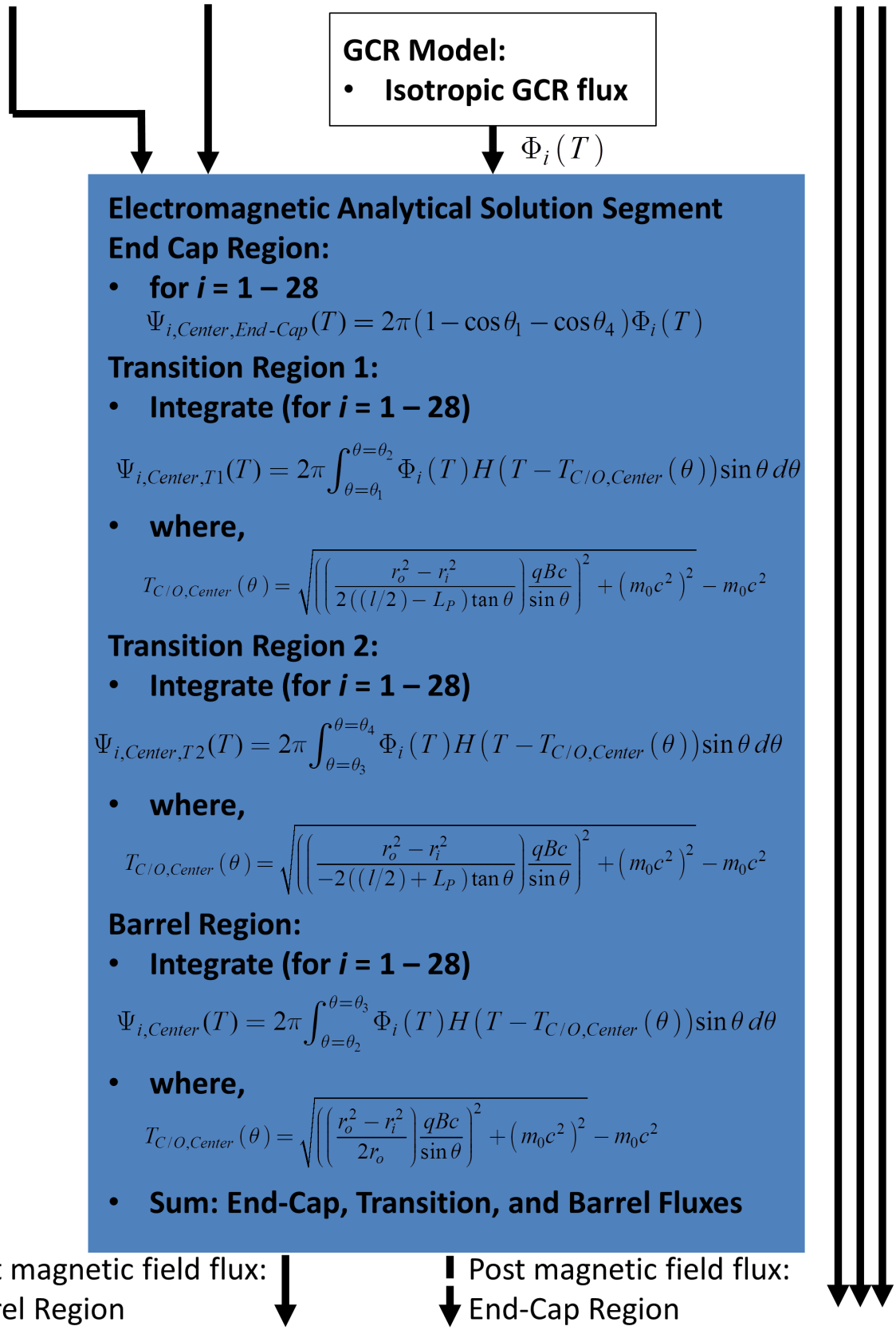

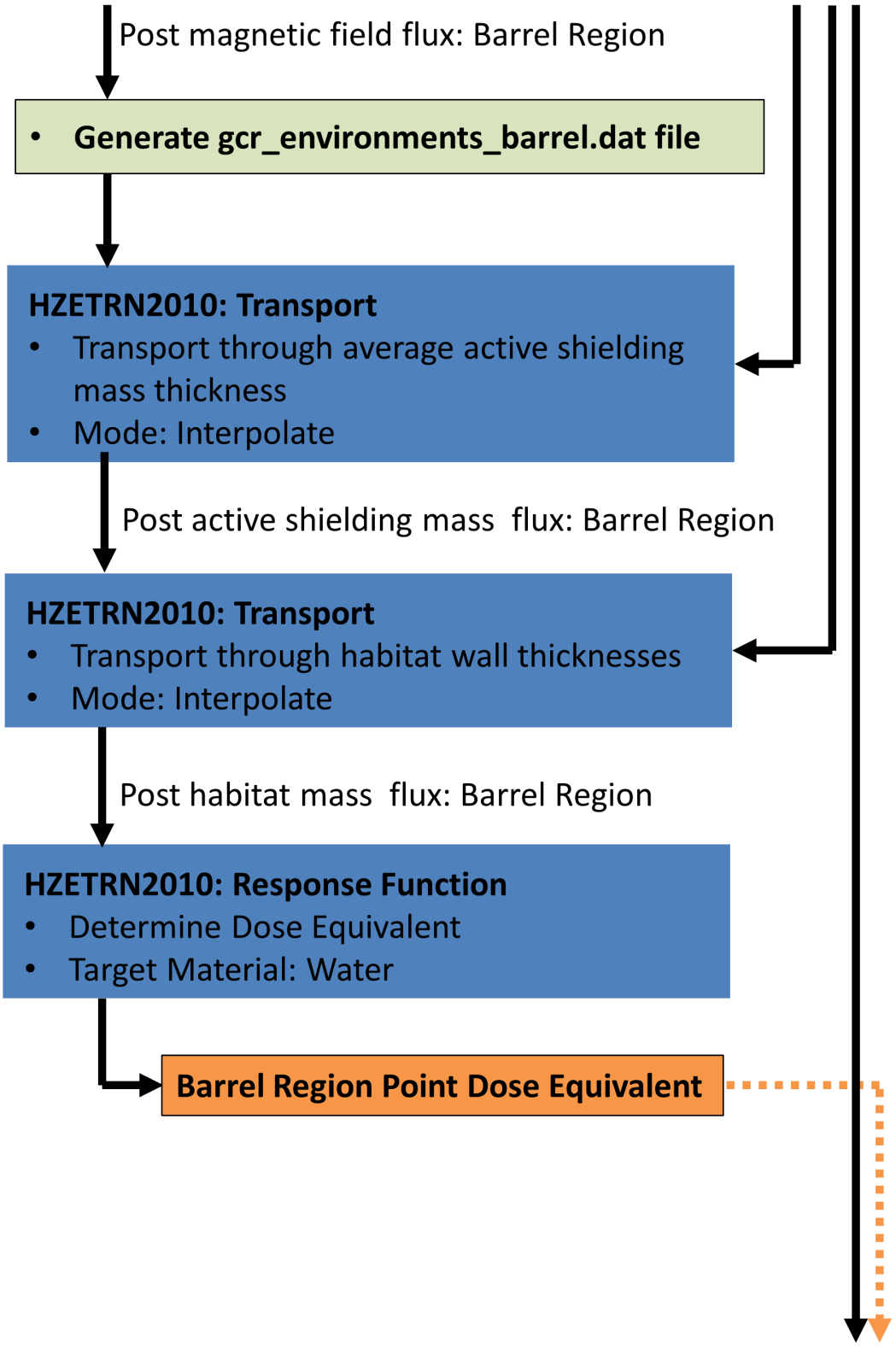

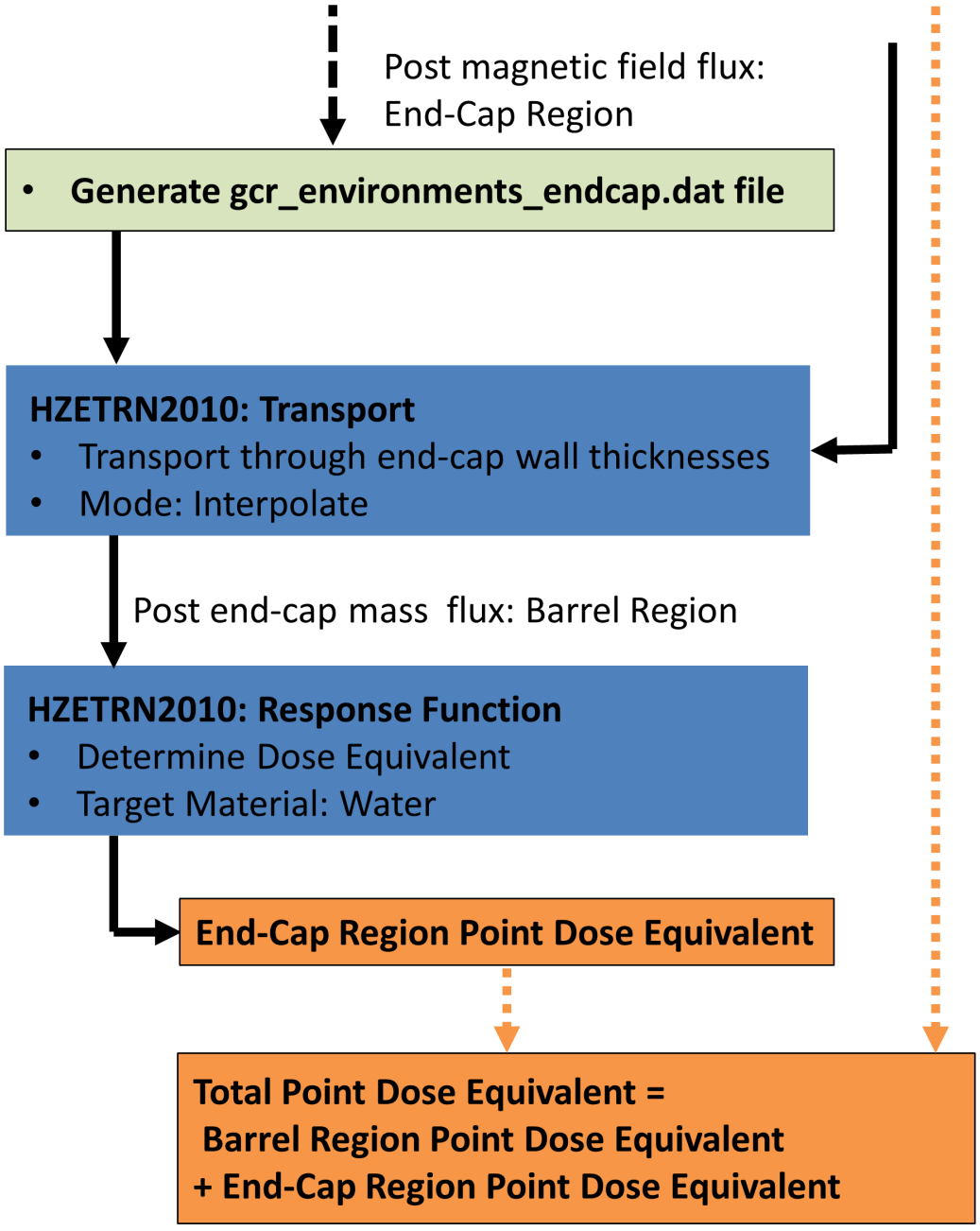

Appendix D:

System Mass Estimates Flowchart and Summary

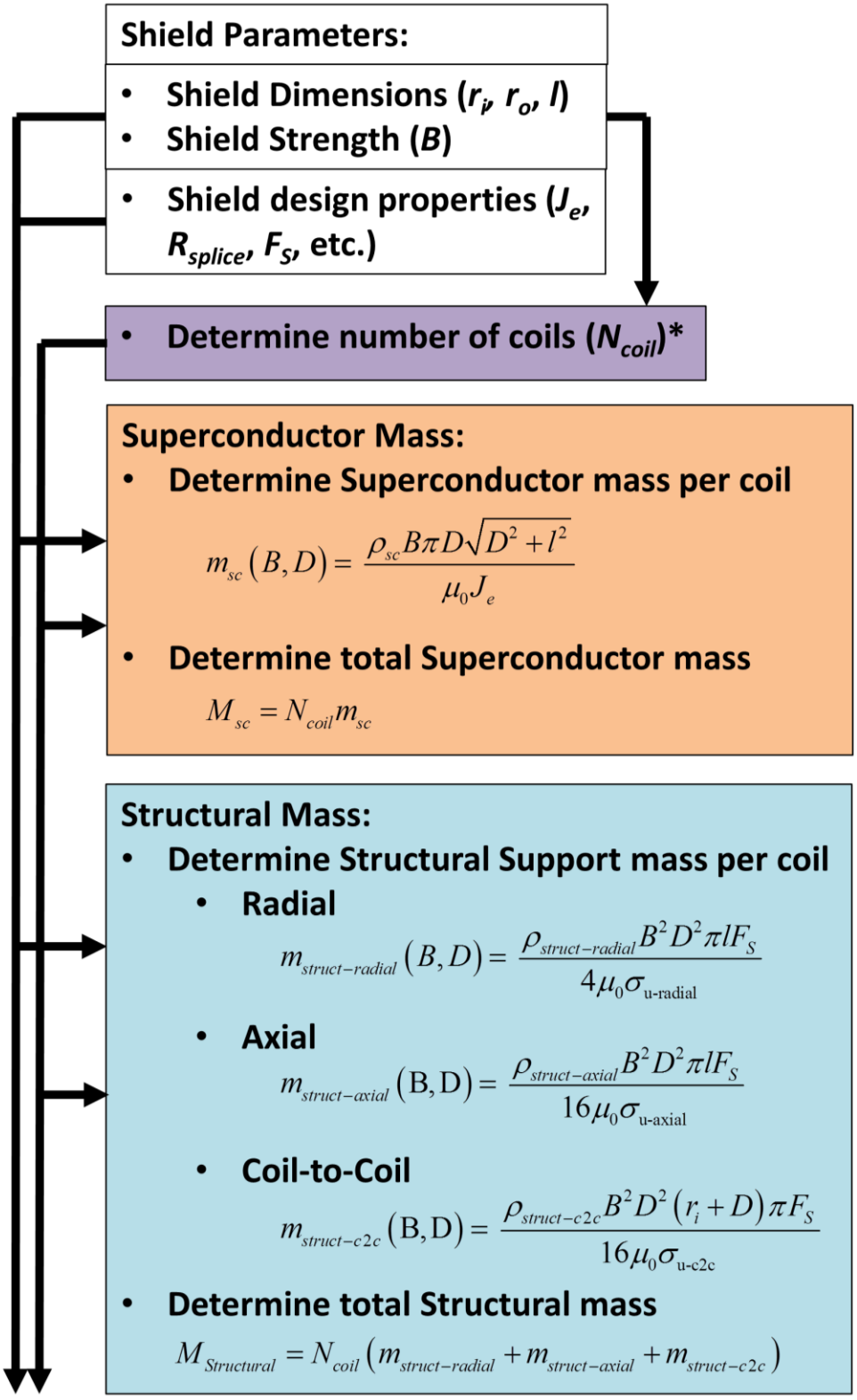

Thermal Mass:

- **Determine system heat load**
  - **External/Internal:**
    - from Figure 5.10
  - **Superconductor Losses:**

$$Q_{splice}(B,D)=\frac{J_e A_t R_{splice}\pi BD\sqrt{D^2+l^2}}{\mu_0 L_{\max}}$$

  - **Total Heat load**

$$Q_L = Q_{Ext/Int} + Q_{splice}$$

- **Determine Cryocooler Mass**

$$m_{Cryocooler} = 0.0711\left(\frac{1}{\eta}Q_L\left(\frac{T_H}{T_{op}}-1\right)\right)^{0.905}$$

- **Determine System Mass**

$$M_{Thermal} = C_T m_{Cryocooler}$$

  - **C_T = correction factor to account for circulator fans, heat exchangers, and piping**

****Note: thermal radiator mass is not included in the shielding estimates shown in this work. However it may be estimated by the following**

$$M_{Thermal-Radiators} = C_{Radiators} Q_L\left(1+\frac{1}{\eta}\left(\frac{T_H}{T_{OP}}-1\right)\right)$$

where, $C_{Radiators} = \frac{1120\,\text{kg}}{11.8\,\text{kW}}$

and is a relationship derived from the ISS HRS radiators

Power Mass:

- **Superconductor power supply is considered negligible**

*****Note: solar array mass is not included in the shielding estimates shown in this work. However it may be estimated by the following**

$$M_{Power-SolarArrays} = C_{SolarArrays} Q_L \left(\frac{1}{\eta} \left(\frac{T_H}{T_{OP}} - 1 \right) \right)$$

where,

$$C_{SolarArrays} = \frac{1\,\text{kg}}{70\,\text{W}}$$

and is a relationship based on the use of Triple Junction (TJ) GaAs rigid panel solar arrays

***In this study, the number of coils (N_{coil}) is estimated by:**

$$N_{coil}(D) = \frac{2\pi\left(r_i + D/2\right)}{D}$$

-Note, this may result in a non-integer number of coils; however, this provides an interpolated mass estimate over the trade space analyzed